Reflection and Refraction
of Spin Waves

Dissertation

zur Erlangung des Doktorgrades
der Naturwissenschaften (Dr. rer. nat.)
der Fakultät für Physik
der Universität Regensburg

vorgelegt von

Johannes Stigloher

aus Rosenheim

im Jahr 2018

Contents

1 Introduction

Spin waves are the collective excitations of magnetically ordered systems. Their respective quasi particle — the magnon — is name-giving for a rapidly evolving research area called magnonics. The field aims to exploit spin waves to carry, process, and store information [1]. Potentially small wavelengths in the nanometer range [2], high frequencies in the terahertz regime [3], and Joule-heat-free transport [4] are promising features for such applications. Underlining the growing interest in magnonics and related subjects, a whole bouquet of review articles has been published in the last decade [5, 6, 7, 8, 9].

Accompanying the technological motivation, spin waves have been the subject of fundamental research giving valuable insights in Bose-Einstein condensation [10], spin wave tunneling [11], and artificial [9] or natural magnonic crystals [12, 13]. General wave properties shared with e.g. light waves or sound waves led to the study of spin wave analogs to diffraction [14, 15], interference [16, 17, 18], or the Doppler effect [19, 20]. In particular, the anisotropic nature of spin wave propagation [21] — even in isotropic magnetic media — and its comparatively easy manipulation by external magnetic fields or electrical currents [22] allows for rich physics to be discovered and exploited.

To this end, this thesis focuses on the experimental investigation of spin wave reflection and refraction in the magnetostatic regime. In particular, the transmission of plane waves through an interface of two $Ni_{80}Fe_{20}$ (permalloy, Py) films of different thickness is studied by means of time resolved scanning Kerr microscopy (TRMOKE). This optical technique allows to directly image wave fronts of incident, reflected, and refracted waves thus providing information on their wavelength, angular dependence, and attenuation. Their relation is explained by incorporating the anisotropic dispersion relation, which enables us to formulate Snell's law for spin waves [23]. Especially the use of a thickness step from a thick to a thin film as an interface for the refraction process provides an efficient way of spin wave steering and wavelength reduction [24] — two problems that are actively investigated in magnonics [25, 26, 27, 28, 29].

With the same technique, the reflection of plane spin waves at the edge of a Py film is examined. We observe that the phase of the reflected wave exhibits a shift with respect to the incident wave that depends on the wave vector component along the interface. Such a phase shift for a plane wave is known to lead to a spatial shift for a beam [30]. These are called Goos-Hänchen (GH) shifts and were experimentally first observed in optics [31]. Recently, they have been proposed for spin waves in different wave vector regimes and geometries [32, 33, 34, 35]. Since our experimental results are not covered by these predictions, a numerical model is developed that provides insights into the physics governing the shift. We can show that dipolar interactions naturally cause GH-like phase shifts for plane spin waves in our wavelength regime and consequently expect GH beam shifts for spin waves [36].

This thesis is divided into two parts. Part I starts with an introduction to the theory of spin waves in the dipole-exchange regime that covers wavelengths in the range of nanometer to millimeter. Chapter 2 includes their analytic description within the framework of micromagnetism, the derivation of dispersion relations, and their excitation by means of microwave antennas. In Chapter 3, the methods utilized in this thesis are reviewed. In particular, numerical methods to obtain the spin wave spectrum in a full film (Sec. 3.2.1) and a stripe (Sec. 3.2.2) are described. Thereafter, an overview of the TRMOKE setup will be given. Part I concludes with Chapter 4, which gives insight into the unique properties of spin wave propagation by combining numerical methods, analytic dispersion relations, and first experimental results. In particular, the surface character of spin waves and spin wave caustics are discussed. The analytic dispersion relation is verified with the help of the numerical model.

Part II is dedicated to reflection and refraction experiments. Since all of these are conducted on similar samples, Chapter 5 introduces their general design and the coordinate system used. In Chapter 6, we describe our experimental results on Snell's law for spin waves. This includes a characterization of samples with the help of the analytic dispersion relation, a discussion on the phenomenon of spin wave bending, as well as the comparison to Snell's law in optics. Chapter 7 summarizes the dependence of the refraction process on the thickness. Finally, Chapter 8, deals with the experiments on the GH-like phase shift of spin waves. After a review of the connection to beams, the experimental results are compared to numerical simulations to reveal the connection of the GH shift to magnetostatic interactions.

Part I

Preliminaries

2 Theory of Dipole-Exchange Spin Waves

Spin waves can be understood as a propagating phase of neighboring, precessing magnetic moments with defined wave vector $\mathbf{k}$. They are closely related to ferromagnetic resonance (FMR) [37, 38], the resonant absorption of electromagnetic energy by a ferromagnet. FMR constitutes the special case of uniform precession, i.e. a wave vector magnitude $k = 0$. Spin waves with $k = 0$ and $k \neq 0$ are sketched in Fig. 2.1. Depending on the magnitude k, the propagation is governed by either magnetic dipolar ($k < 10\,\mu\text{m}^{-1}$) or exchange interactions ($k > 100\,\mu\text{m}^{-1}$). The intermediate regime is called dipole-exchange spectrum, where both contributions need to be considered.

Spin waves were first described by Bloch [39] in 1930 within a microscopic theory that explained the temperature dependence of the saturation magnetization. This microscopic description is reasonable for wavelengths on the order of atomic distances and consequently describes exchange spin waves [40]. Landau and Lifshitz [41] developed a macroscopic description of ferromagnets by obtaining the equation of motion for the magnetization, a continuous vector field that averages magnetic moments of individual atoms. Nowadays, this approach is called micromagnetism [42]. It triggered the study of spin waves in the long wavelength limit: Walker [43] and others [44, 45] simultaneously solved Maxwell's equations and Landau and Lifhsitz's equation in bounded ferromagnets. The solutions were called magnetostatic modes or dipolar spin waves.

These classical magnetostatic modes are name-giving for the main geometries in which spin waves are typically classified. Usually, one considers a propagating spin wave with wave vector $\mathbf{k}$ in the plane of a ferromagnetic film. Depending on the direction of magneti-
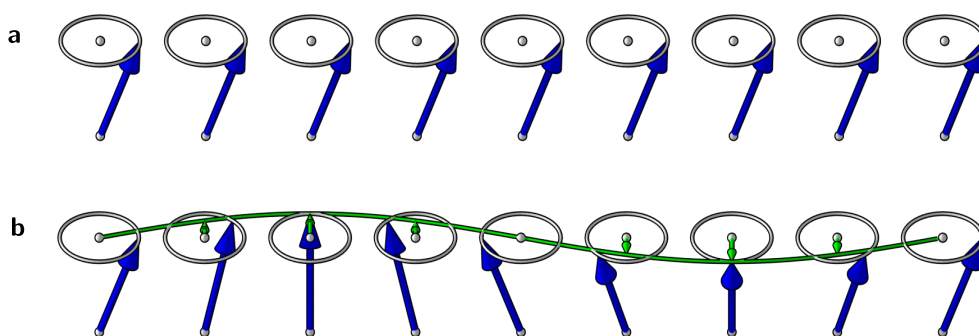
Figure 2.1: Sketch of a snapshot in time of two spin waves with $k = 0$ and $k \neq 0$ in **a** and **b**, respectively. Blue denotes either the spin or the magnetization, precessing around its equilibrium. The green arrows in **b** depict one component of the precession amplitude, which changes harmonically in space, as indicated by the sine-like green curve connecting the arrows.
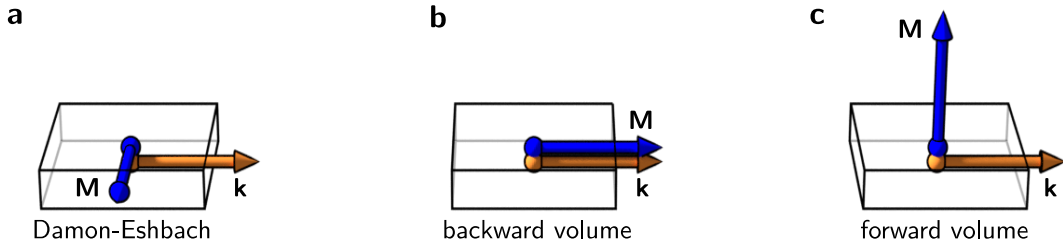
Figure 2.2: Main geometries of in-plane propagating spin waves. **a** Damon-Eshbach, **b** backward volume, and **c** forward volume modes.

zation $\mathbf{M}$, the modes are either called Damon-Eshbach (DE) or surface spin waves ($\mathbf{M} \perp \mathbf{k}$, $\mathbf{M}$ in the plane), backward volume (BV) spin waves ($\mathbf{M} \parallel \mathbf{k}$, $\mathbf{M}$ in the plane), and forward volume (FV) spin waves ($\mathbf{M}$ perpendicular to the plane), see Fig. 2.2. All three modes have unique dispersion relations, which smoothly merge into one another for arbitrary directions of $\mathbf{M}$ and $\mathbf{k}$. Especially the spin wave manifold for both the magnetization as well as the wave vector in the sample plane will be investigated in this thesis.

In addition to an in-plane propagating wave vector, all modes can exhibit a standing wave pattern across the thickness of the ferromagnetic film due to confinement in this direction. These modes are called perpendicular standing spin waves (PSSW). In general, they are not purely harmonic, i.e. they do not exhibit a defined wave vector, and crucially depend on the imposed boundary conditions at the top and bottom of the film. The simultaneous treatment of both exchange boundary conditions [46, 47] as well as electromagnetic boundary conditions led to the development of the so called Green's function formalism [21, 48, 49, 50]. It is applicable for the full dipole-exchange spin wave spectrum and contains both dipolar as well as exchange spin waves as limits. Following this approach and Ref. [51], in the subsequent theoretical sections, the dispersion relation for all main modes are derived analytically for the lowest energy PSSW. Higher energy PSSWs are numerically investigated in Sec. 3.2.1.

Experimentally, this thesis discusses magnetostatic modes (with $\mathbf{M}$ in the plane), which are more easily accessible than exchange spin waves. Wavelengths are large enough (micrometer – millimeter) to be spatially resolved by magneto-optical imaging techniques such as TRMOKE [52] and Brillouin light scattering (BLS) [53, 54]. Together with the all-electrical propagating spin wave spectroscopy (PSWS) [55], they comprise the main measurement techniques for this wave vector regime.

This chapter starts by shortly formulating a theoretical basis within the framework of micromagnetism following Refs. [42, 56, 57, 58]. As already done in this introduction, we will denote vectors with bold symbols and their magnitudes with the respective italic symbol. In addition, tensors are also denoted with bold symbols. Unit vectors are denoted with $\mathbf{e}_i$, where the subscript i gives their direction.

2.1 Micromagnetism

The basis of micromagnetism is the description of the magnetization $\mathbf{M}(\mathbf{r}, t)$, which is a smooth, continuous vector field, defined on length scales well above the atomic scale, where the discrete nature of atoms can be neglected. This is true in both space $\mathbf{r}$ and time t [42, 58]. It can be defined as the sum of individual magnetic moments $\boldsymbol{\mu}$ per volume V

$$\mathbf{M}(\mathbf{r}, t) = \frac{\sum_V \boldsymbol{\mu}}{V} \, .$$

The vector field exists up to a material dependent Curie temperature T_C. This continuum approach enables a classical treatment of ferromagnetism, although magnetism must be regarded as a quantum mechanical phenomenon. The existence of magnetic moments $\boldsymbol{\mu}$ is closely connected to the spin. The long range ordering of individual $\boldsymbol{\mu}$ in ferromagnets — which allows us to define $\mathbf{M}(\mathbf{r}, t)$ — has its roots in the exchange interaction. Both are fundamentally of quantum mechanical nature, but their macroscopic influence can be grasped within the theory of micromagnetism.

At temperatures below T_C the magnetization vector is assumed to have a defined length M_S everywhere in space. This material parameter is called the saturation magnetization. The ground state of $\mathbf{M}$ is found by accounting for relevant magnetic field contributions $\mathbf{H}_{\text{eff}}$. These are usually derived from the free energy density F via [57]

$$\mathbf{H}_{\text{eff}} = -\frac{1}{\mu_0} \frac{\delta F}{\delta \mathbf{M}} \, , \tag{2.1}$$

with $\mu_0 = 4\pi \times 10^{-7} \, \text{VsA}^{-1}\text{m}^{-1}$ the permeability of vacuum. Then, the so called Brown's equation [42]

$$\mathbf{M} \times \mathbf{H}_{\text{eff}} = 0 \tag{2.2}$$

defines the equilibrium position of $\mathbf{M}$ — aligned parallel to $\mathbf{H}_{\text{eff}}$. In this work, three energy density contributions are considered for the derivation of $\mathbf{H}_{\text{eff}}$ [58]:

- The Zeeman energy density

$$F_{\text{zee}} = -\mu_0 \mathbf{M} \cdot \mathbf{H}_{\text{ext}} \, , \tag{2.3}$$

  which describes the action of an external field $\mathbf{H}_{\text{ext}}$ on the magnetization. It is obviously favorable if the magnetization is aligned parallel to $\mathbf{H}_{\text{ext}}$.

- The exchange energy density

$$F_{\text{exc}} = \frac{A}{M_S^2} \left((\boldsymbol{\nabla} \cdot M_x)^2 + (\boldsymbol{\nabla} \cdot M_y)^2 + (\boldsymbol{\nabla} \cdot M_z)^2 \right) \, , \tag{2.4}$$

  which tends to uniformly align the magnetization. Here, A is called the exchange stiffness constant.

- The demagnetizing energy density

$$F_{\text{dem}} = -\frac{1}{2}\mu_0 \mathbf{M} \cdot \mathbf{H}_{\text{dem}}\,, \tag{2.5}$$

which stems from long-ranged magnetic dipole interactions and depends on the given sample geometry. The demagnetizing field $\mathbf{H}_{\text{dem}}$ describes this interaction and is the dominant contribution for spin waves discussed experimentally in this thesis.

The last two energy contributions that lead to non-local fields also define a characteristic exchange length [57]

$$l_{\text{exc}} = \sqrt{\frac{2A}{\mu_0 M_{\text{S}}^2}} \tag{2.6}$$

that defines a scale, where exchange is dominant and the magnetization can thus be assumed as uniform. The sum of all contributions $F = F_{\text{dem}} + F_{\text{zee}} + F_{\text{exc}}$ defines the effective field via Eq. (2.1). It is given by $\mathbf{H}_{\text{eff}} = \mathbf{H}_{\text{ext}} + \mathbf{H}_{\text{dem}} + \mathbf{H}_{\text{exc}}$ with

$$\mathbf{H}_{\text{exc}} = l_{\text{exc}}^2 \Delta \mathbf{M}\,. \tag{2.7}$$

Typically, it is not trivial to calculate $\mathbf{H}_{\text{dem}}$ for arbitrary sample shapes. To this end, Sec. 2.3 is devoted to derive this field from magnetostatic Maxwell's equations. Alternatively, one could obtain $\mathbf{H}_{\text{dem}}$ by considering the microscopic dipolar fields originating from individual $\boldsymbol{\mu}$. Owing to these different points of view, $\mathbf{H}_{\text{dem}}$ is interchangeably called dipolar field, stray field (outside the sample) or magnetostatic field in the literature. Further contributions, e.g. magnetocrystalline anisotropy, anisotropic exchange, or strain are not discussed here, as they only play a minor role in our experiments.

2.2 Magnetization Dynamics

In a non equilibrium situation, where $\mathbf{M}$ is not aligned parallel with $\mathbf{H}_{\text{eff}}$, a torque acts on the magnetization resulting in a precessional motion of the magnetization around $\mathbf{H}_{\text{eff}}$. The temporal and spatial evolution of $\mathbf{M}$ is described by the Landau-Lifshitz-Gilbert equation (LLG) [41]

$$\frac{\partial \mathbf{M}}{\partial t} = \underbrace{-\gamma\mu_0(\mathbf{M} \times \mathbf{H}_{\text{eff}})}_{\text{precession}} + \underbrace{\frac{\alpha}{M_{\text{S}}}\left(\mathbf{M} \times \frac{\partial \mathbf{M}}{\partial t}\right)}_{\text{damping}}, \tag{2.8}$$

with $\gamma = |\frac{ge}{2m_{\text{e}}}|$ the gyromagnetic ratio, e the electron charge, m_{e} the mass of the electron, and g the Landé factor. The strength of the damping term is accounted for by a dimensionless material parameter, the damping constant α. This equation preserves the length of $\mathbf{M}$ and the trajectory of the magnetization spirals towards equilibrium if there is no external stimulus, e.g. a driving field that preserves the precession. The two torque terms — precession and damping — are depicted in Fig. 2.3.

To solve the LLG, we will assume a harmonic time dependence with angular frequency $\omega = 2\pi f$. Thereafter, the magnetization is divided in a space and time dependent, dynamic
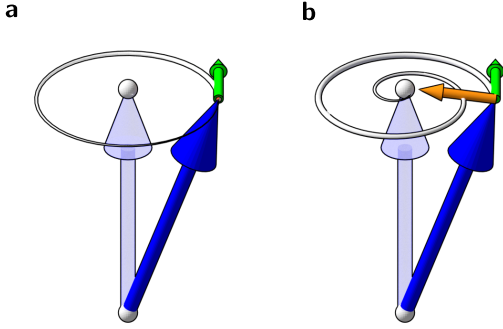
Figure 2.3: a The magnetization (blue) follows a precessional trajectory driven by the torque $-\gamma\mu_0(\mathbf{M} \times \mathbf{H}_{\text{eff}})$ (green arrow). **b** The dissipation of energy is accounted for by the torque $\frac{\alpha}{M_{\text{S}}}\left(\mathbf{M} \times \frac{\partial \mathbf{M}}{\partial t}\right)$ (orange arrow). The resulting motion is a spiral towards the equilibrium position (transparent blue) given by the direction of $\mathbf{H}_{\text{eff}}$.

part $\mathbf{m}(\mathbf{r}, t) = \mathbf{m}_0(\mathbf{r})\exp(\mathrm{i}\omega t)$ and a static, uniform part $\mathbf{M}_{\text{eq}}$. It is further assumed that the precession angle is small, such that the magnitudes fulfill $m \ll M_{\text{eq}}$ and $M_{\text{eq}} = M_{\text{S}}$. We choose a coordinate system attached to the magnetization as depicted in Fig. 2.4. In this coordinate system, the magnetization can therefore be written as

$$\mathbf{M}(\mathbf{r}, t) = \begin{pmatrix} m_x \\ M_{\text{S}} \\ m_z \end{pmatrix}.$$

Likewise, the field is separated into a dynamic part $\mathbf{h}$ and and a static part $\mathbf{H}$, such that $\mathbf{H}_{\text{eff}} = H\mathbf{e}_y + (h_x\mathbf{e}_x + h_z\mathbf{e}_z)$.

Put into Eq. (2.8) and neglecting non-linear terms of $\mathbf{h}$ and $\mathbf{m}$, the result is called the linearized LLG

$$\begin{pmatrix} \mathrm{i}m_x\omega \\ \mathrm{i}m_z\omega \end{pmatrix} = \begin{pmatrix} -\gamma\mu_0\left(-Hm_z + M_{\text{S}}h_z\right) + \mathrm{i}\alpha m_z\omega \\ -\gamma\mu_0\left(Hm_x - M_{\text{S}}h_x\right) - \mathrm{i}\alpha m_x\omega \end{pmatrix}. \tag{2.9}$$

For completeness, the linearized LLG excluding damping is obtained for $\alpha = 0$ and writes

$$\begin{pmatrix} \mathrm{i}m_x\omega \\ \mathrm{i}m_z\omega \end{pmatrix} = \begin{pmatrix} -\gamma\mu_0\left(-Hm_z + M_{\text{S}}h_z\right) \\ -\gamma\mu_0\left(Hm_x - M_{\text{S}}h_x\right) \end{pmatrix}. \tag{2.10}$$

The latter is the main equation solved in this thesis, as it allows for the derivation of dispersion relations of (linear) spin waves. For this reason, expressions for H and $\mathbf{h}$ are needed. In the following, the necessary steps towards their analytical form in certain circumstances are given. In Sec. 3.2, techniques to solve Eq. (2.10) numerically are described.

For the discussion of spin waves in the experimentally accessible $\mathbf{k}$-vector range, the demagnetizing energy and associated fields dictate the dispersion relation. Due to their non-local, dipolar nature, these are typically the most demanding to derive. The following section shall therefore give a formal basis for their understanding within the framework of magnetostatics. Afterwards, H and $\mathbf{h}$ are derived from the important energies in Secs. 2.4 and 2.5, which finally allows to derive the full film dispersion relations.

Figure 2.4: Coordinate system xyz. The (harmonic) dynamic magnetization components are m_x and m_z and the static, not-time-dependent magnetization $\mathbf{M}_{\text{eq}}$ will always be aligned parallel with y. It holds true that $m \ll M_{\text{eq}}$ and $M_{\text{eq}} = M_{\text{S}}$.
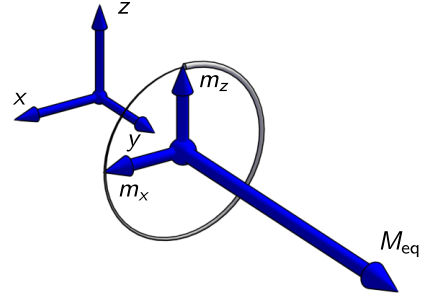
2.3 Magnetostatics

In the absence of currents, Maxwell's equations for ferromagnetic media in the magneto-static limit [42, 56, 59] read

$$\begin{aligned} \boldsymbol{\nabla} \times \mathbf{H} &= 0\,, \\ \boldsymbol{\nabla} \cdot \mathbf{B} &= \mu_0 \boldsymbol{\nabla} \cdot (\mathbf{H} + \mathbf{M}) = 0\,. \end{aligned} \tag{2.11}$$

The first equation implies the existence of a scalar potential function ϕ_M that fulfills

$$\mathbf{H} = -\boldsymbol{\nabla}\phi_M\,. \tag{2.12}$$

Together with the second Maxwell equation,

$$\nabla^2 \phi_M = \boldsymbol{\nabla} \cdot \mathbf{M} = -\rho_M \tag{2.13}$$

defines the magnetic charge density ρ_M in reminiscence on the electrostatic potential and respective electric charge density. The field defined by Eq. (2.12) is called the demagnetizing field $\mathbf{H}_{\text{dem}}$, which originates from ρ_M and therefore $\mathbf{M}$. The usual procedure to obtain $\mathbf{H}_{\text{dem}}$ is to find solutions for ϕ_M and then simply take the gradient of the potential. To do so, the Green's function G for the Laplace operator defined by

$$\nabla^2 G(\mathbf{r}) = \delta(\mathbf{r})$$

is used, where δ refers to the Dirac delta distribution. In three dimensions, this function is known to be

$$G(\mathbf{r}) = -\frac{1}{4\pi|\mathbf{r}|}\,. \tag{2.14}$$

It follows that the solution to Eq. (2.13) can be directly obtained as a convolution of G and ρ_M in a finite volume V' via

$$\phi_M(\mathbf{r}) = -\frac{1}{4\pi} \int_{V'} \mathrm{d}^3\mathbf{r}' \frac{\boldsymbol{\nabla}' \cdot \mathbf{M}(\mathbf{r}')}{|\mathbf{r} - \mathbf{r}'|}\,.$$

Here, the primed coordinate system represents the source of the potential, i.e. a finite magnetization. If V' is large enough such that it fully contains the region where $\mathbf{M}$ is not zero, an integration by parts yields

$$\phi_M(\mathbf{r}) = \frac{1}{4\pi} \int_{V'} \mathrm{d}^3\mathbf{r}' \boldsymbol{\nabla}' \left(\frac{1}{|\mathbf{r}-\mathbf{r}'|} \right) \cdot \mathbf{M}(\mathbf{r}') \,, \qquad (2.15)$$

since the surface integral vanishes. Note that far away from a region with a total magnetic moment $\boldsymbol{\mu} = \int_{V'} \mathbf{M}'$, the potential has the form of a dipole potential $\frac{\mathbf{r}\cdot\boldsymbol{\mu}}{4\pi\, r^3}$ [59], which further illustrates the terminology *dipolar field*.

In the literature, an equivalent definition of the potential is often used: after the divergence theorem is applied, ϕ_M is separated into a surface and a volume part. This approach then defines the magnetic surface charge density $\sigma_S = \mathbf{n}\mathbf{M}$, with the outward normal $\mathbf{n}$. The concept of magnetic surface charges as sources of magnetic field $\mathbf{H}_{\mathrm{dem}}$ often helps as an intuitive model to understand processes involving magnetostatic interactions. As the generation of $\mathbf{H}_{\mathrm{dem}}$ is associated with an increase in energy (cf. Eq. (2.5)), systems avoid the creation of charges. A simple example is the magnetization lying in-plane in an infinitely extended thin film in the absence of anisotropies. In this case, no surface charges are created as $\mathbf{n}\mathbf{M}$ vanishes, which constitutes the energetic minimum. Mathematically, there is no need to define a surface, as long as boundaries to non-magnetic materials are regarded as rapid, but smooth variations of $\mathbf{M}$ to zero [42, 59].

The spatial average of the demagnetizing field in a volume V is finally obtained from Eqs. (2.15) and (2.12) as

$$< \mathbf{H}_{\mathrm{dem}} >_V = -\frac{1}{4\pi\, V} \int_V \mathrm{d}^3\mathbf{r} \int_{V'} \mathrm{d}^3\mathbf{r}' \boldsymbol{\nabla}\boldsymbol{\nabla}' \left(\frac{1}{|\mathbf{r}-\mathbf{r}'|} \right) \cdot \mathbf{M}(\mathbf{r}') \,. \qquad (2.16)$$

Note that the averaging of the field is important in many practical applications, for instance if mean fields over some sample dimensions are considered. In numerical simulations, space is usually discretized in finite volumes and the above averaging is mandatory for a correct description of $\mathbf{H}_{\mathrm{dem}}$. Besides, it prevents non-physical singularities which can in principle arise at sample boundaries.

The kernel of the above expression is sometimes called Green's function tensor [51] defined as

$$\boldsymbol{\Gamma}(\mathbf{r}-\mathbf{r}') = -\boldsymbol{\nabla}\boldsymbol{\nabla}'\frac{1}{4\pi|\mathbf{r}-\mathbf{r}'|} \,.$$

In Cartesian coordinates, $\boldsymbol{\Gamma}$ is a 3×3 matrix with elements

$$\Gamma_{ij} = -\frac{\partial}{\partial r_i}\frac{\partial}{\partial r_j'} \frac{1}{4\pi|\mathbf{r}-\mathbf{r}'|} \,, \qquad (2.17)$$

where i, j are either of the three spatial coordinates. Some properties of the original Green's function, Eq. (2.14), are inherited, e.g. by using

$$\boldsymbol{\nabla}' \left(\frac{1}{|\mathbf{r}-\mathbf{r}'|} \right) = -\boldsymbol{\nabla} \left(\frac{1}{|\mathbf{r}-\mathbf{r}'|} \right) \,, \qquad (2.18)$$

the trace of $\mathbf{\Gamma}$ is

$$\text{tr}(\mathbf{\Gamma}) = -\nabla^2 G(\mathbf{r} - \mathbf{r}') = -\delta(\mathbf{r} - \mathbf{r}')\,. \tag{2.19}$$

Due to interchangeable derivatives, $\mathbf{\Gamma}$ has symmetric character i.e.,

$$\Gamma_{ij} = \Gamma_{ji}\,. \tag{2.20}$$

For any body with uniform magnetization (innately true for ellipsoids), the integral in Eq. (2.16) can be evaluated independently of $\mathbf{M}$ [60]. This implies the existence of a geometric demagnetizing tensor $\mathbf{N}$ (e.g. Refs. [61, 42]) that directly links the magnetization with its associated field via

$$\mathbf{H}_{\text{dem}} = -\mathbf{N} \cdot \mathbf{M}\,. \tag{2.21}$$

The components of the demagnetizing tensor N_{ij} are in general positive, accounting for the name-giving property of $\mathbf{H}_{\text{dem}}$ that its direction is opposite to $\mathbf{M}$, hence *demagnetizing* the sample. From Eqs. (2.19) and (2.20), we obtain that [62]

$$\text{tr}(\mathbf{N}) = 1 \quad \text{and} \quad N_{ij} = N_{ji}\,,$$

while the first condition is only true if the field is evaluated in the same volume as the magnetization (self-demagnetizing). For arbitrary sample geometries, the demagnetizing tensor is not easily calculated [63, 64] as the magnetization is generally non-uniform. To obtain magnetization patterns in these geometries, one usually resorts to simulations which subdivide the magnetic medium in small cells where $\mathbf{M}$ can be regarded uniform. Then, Eq. (2.21) holds and the problem is reduced to finding an appropriate demagnetizing tensor $\mathbf{N}$, which also accounts for the case where the volume of magnetization does not coincide with the volume of the field (mutual-demagnetizing). In that case, it follows $\text{tr}(\mathbf{N}) = 0$. The concept of demagnetizing tensors can be applied to static and dynamic parts of $\mathbf{H}_{\text{dem}}$ and is explained in the following two sections in more detail. We will denote the static demagnetizing tensor by $\mathbf{N}$ and the dynamic demagnetizing tensor by $\mathbf{n}$.

2.4 Static Field and Coordinate Systems

For the following derivations, we introduce a new Cartesian coordinate system with co-ordinates u, v, and w, attached to the laboratory frame. We define two transformation matrices

$$\mathbf{R}_u = \begin{pmatrix} 1 & 0 & 0 \\ 0 & \cos(\theta) & -\sin(\theta) \\ 0 & \sin(\theta) & \cos(\theta) \end{pmatrix}, \quad \mathbf{R}_w = \begin{pmatrix} \cos(\phi) & -\sin(\phi) & 0 \\ \sin(\phi) & \cos(\phi) & 0 \\ 0 & 0 & 1 \end{pmatrix}, \tag{2.22}$$

which link the laboratory frame with the magnetization frame via a rotation around the axes w and u with angles ϕ and θ, respectively. The two coordinate systems with the definitions of the angles are depicted in Fig. 2.5 **a**. A vector $\mathbf{r}^{xyz}$ and $\mathbf{r}^{uvw}$ in xyz and uvw
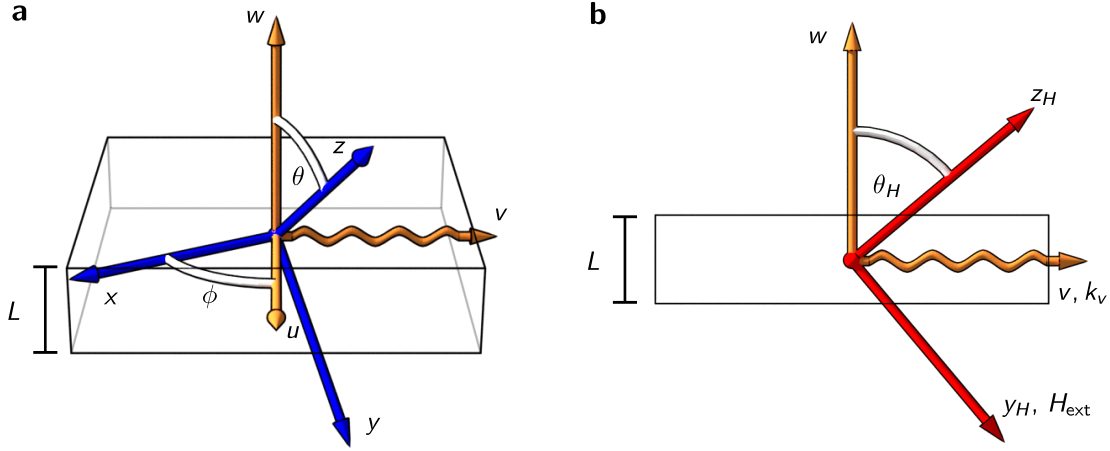
Figure 2.5: Definition of coordinate systems. **a** shows the definition of angles ϕ and θ that connect the coordinate systems uvw and xyz. The former is defined with respect to the sample with thickness L. The vector $\mathbf{e}_v$ will later be chosen as spin wave propagation direction. xyz is attached to the magnetization system and, as defined in Fig. 2.4, M_{eq} is directed along y-direction. In **b**, a coordinate system $y_H z_H$ is similarly defined as xyz with the external field H_{ext} always pointing along y_H.

coordinate systems, respectively, is therefore transformed by

$$\mathbf{r}^{xyz} = \mathbf{R}_u \cdot \mathbf{R}_w \cdot \mathbf{r}^{uvw} = \mathbf{R} \cdot \mathbf{r}^{uvw},$$
$$\mathbf{r}^{uvw} = \mathbf{R}_w^{\mathrm{T}} \cdot \mathbf{R}_u^{\mathrm{T}} \cdot \mathbf{r}^{xyz} = \mathbf{R}^{\mathrm{T}} \cdot \mathbf{r}^{xyz}.$$

The superscript T denotes a transposed matrix.

As pointed out in Section 2.1, three energy densities contribute to $\mathbf{H}_{\mathrm{eff}}$ and have to be considered for both static and dynamic fields. In the following, we will restrict the discussion to the case where the static part of magnetization and field are considered uniform in space. Then, the exchange interaction does not influence H as the gradient of $\mathbf{M}$ vanishes. It remains to discuss the fields associated with the demagnetizing and Zeeman energies.

For thin films, the demagnetizing tensor is particularly simple, since only the demagnetizing tensor component $N_{ww} = 1$ is different from zero [56, 65]. Then, the demagnetizing energy density takes the form $F_{\mathrm{dem}} = \frac{\mu_0}{2} M_w^2$ such that the whole static energy is given by

$$F = \frac{\mu_0}{2} M_w^2 - \mu_0 \mathbf{H}_{\mathrm{ext}} \mathbf{M}.$$

As mentioned before, a finite component M_w would lead to an increase in energy. Therefore, without additional energy contributions, the magnetization will always be in-plane for thin films. If an external field is applied in the film plane, the magnetization will be aligned parallel to this field and the internal field strength verifies $H = H_{\mathrm{ext}}$. By contrast, for an out-of-plane biased film, the effective field strength H has to be deduced from the

energy. In xyz, F reads

$$F = \frac{\mu_0}{2} \left(-M_y \sin\left(\theta\right) + M_z \cos\left(\theta\right)\right)^2 - \mu_0 \mathbf{H}_{\text{ext}} \mathbf{M} ,$$

with the external field $\mathbf{H}_{\text{ext}}$ in the uvw frame as

$$\mathbf{H}_{\text{ext}}^{uvw} = \begin{pmatrix} 0 \\ H_{\text{ext}} \cos\left(\theta_H\right) \\ -H_{\text{ext}} \sin\left(\theta_H\right) \end{pmatrix} .$$

The angle θ_H is the analogon to θ with respect to a coordinate system $y_H z_H$ defined as shown in Fig. 2.5 **b**. There, $\mathbf{H}_{\text{ext}}$ is pointing in y_H-direction. Equation (2.1) yields for the effective static field

$$\mathbf{H}^{xyz} = -\frac{1}{\mu_0} \boldsymbol{\nabla}_M F = \begin{pmatrix} H_{\text{ext},x} \\ H_{\text{ext},y} + \left(-M_y \sin\left(\theta\right) + M_z \cos\left(\theta\right)\right) \sin\left(\theta\right) \\ H_{\text{ext},z} - \left(-M_y \sin\left(\theta\right) + M_z \cos\left(\theta\right)\right) \cos\left(\theta\right) \end{pmatrix} . \tag{2.23}$$

To be compatible with this equation, the external field is transformed into xyz to read

$$\mathbf{H}_{\text{ext}}^{xyz} = \mathbf{R}_u^{\text{T}} \cdot \mathbf{H}_{\text{ext}}^{uvw} = \begin{pmatrix} 0 \\ H_{\text{ext}} \cos\left(\theta - \theta_H\right) \\ H_{\text{ext}} \sin\left(\theta - \theta_H\right) \end{pmatrix} .$$

By applying the premise that $\mathbf{M}$ and $\mathbf{H}$ point in y-direction, i.e. formally utilizing Eq. (2.2), the effective field is obtained from Eq. (2.23) as

$$\mathbf{H} = \begin{pmatrix} 0 \\ H \\ 0 \end{pmatrix} = \begin{pmatrix} 0 \\ H_{\text{ext}} \cos\left(\theta - \theta_H\right) - M_{\text{S}} \sin\left(\theta\right) \sin\left(\theta\right) \\ H_{\text{ext}} \sin\left(\theta - \theta_H\right) + M_{\text{S}} \sin\left(\theta\right) \cos\left(\theta\right) \end{pmatrix} . \tag{2.24}$$

The y and z-components define two equations that determine the angle of magnetization θ and the magnitude of the effective field H for a given direction and magnitude of the external field θ_H and H_{ext}. In the experiments presented in this thesis, exclusively the case $\theta = \theta_H = 0$ is discussed, which simplifies the situation to $H = H_{\text{ext}}$. Additionally, the case $\theta_H = 90°$ is investigated analytically and numerically, since it represents the FV spin wave geometry and should therefore be considered for completeness. In this case, $\theta = 90°$ holds and

$$H = H_{\text{ext}} - M_{\text{S}}$$

as long as $H_{\text{ext}} > M_{\text{S}}$.

2.5 Dynamic Field

If the LLG is solved for its eigenmodes, one does not consider external driving fields. Hence, exchange and demagnetizing fields are sufficient to describe the dynamic field $\mathbf{h}$.

First, we will seek the dynamic demagnetizing fields $\mathbf{h}_{\text{dem}}$, induced by the dynamic

magnetization $\mathbf{m}$. From Eq. (2.16), we obtain

$$< \mathbf{h}_{\mathrm{dem}} >_V = \frac{1}{V} \int_V \mathrm{d}^3\mathbf{r} \int_{V'} \mathrm{d}^3\mathbf{r}' \, \mathbf{\Gamma}(\mathbf{r} - \mathbf{r}') \cdot \mathbf{m} \,. \tag{2.25}$$

In order to derive the dynamic fields, it is most convenient to use the *uvw* reference frame, as the demagnetizing fields depend on the sample geometry. In this frame, the components of the Green's function tensor, Eq. (2.17), are given by

$$\Gamma_{ij} = -\frac{\partial}{\partial r_i} \frac{\partial}{\partial r_j'} \frac{1}{4\pi|\mathbf{r} - \mathbf{r}'|}, \qquad i, j \in \{u, v, w\} \,. \tag{2.26}$$

Since the dynamic fields are induced by spin waves with a defined wave vector $\mathbf{k}$, it is advantageous to evaluate the kernel in Fourier space. We utilize the Fourier representation of the rightmost part of the above equation [59, 51], i.e.

$$\frac{1}{|\mathbf{r} - \mathbf{r}'|} = \frac{1}{2\pi^2} \int \mathrm{d}^3\mathbf{k} \frac{\mathrm{e}^{\mathrm{i}\mathbf{k}(\mathbf{r}-\mathbf{r}')}}{k^2} \,.$$

Using the residuum theorem, this expression can be integrated over the out-of-plane component k_w yielding a dependence on the 2D in-plane wave vector $\mathbf{k}_{\mathrm{ip}} = k_u\mathbf{e}_u + k_v\mathbf{e}_v$ and on an in-plane space vector $\mathbf{r}_{\mathrm{ip}}$

$$\frac{1}{|\mathbf{r} - \mathbf{r}'|} = \frac{1}{2\pi} \int d^2\mathbf{k} \frac{\mathrm{e}^{\mathrm{i}\mathbf{k}_{\mathrm{ip}}(\mathbf{r}_{\mathrm{ip}}-\mathbf{r}'_{\mathrm{ip}})}\mathrm{e}^{-|w-w'|\,k_{\mathrm{ip}}}}{k_{\mathrm{ip}}} \,.$$

This step is performed as we are interested in spin waves traveling in the plane. Differentiation in r and r' in Eq. (2.26) yields the different components of the Green's function tensor in real space

$$\begin{aligned}
\Gamma_{ij}(\mathbf{r}, \mathbf{r}') &= -\frac{1}{8\pi^2} \int d^2\mathbf{k} \frac{k_i k_j}{k_{\mathrm{ip}}} \mathrm{e}^{-|w-w'|\,k_{\mathrm{ip}}} \mathrm{e}^{\mathrm{i}\mathbf{k}_{\mathrm{ip}}(\mathbf{r}_{\mathrm{ip}}-\mathbf{r}'_{\mathrm{ip}})}, & i, j \neq w \,, \\
\Gamma_{wj}(\mathbf{r}, \mathbf{r}') &= -\mathrm{sign}(w - w') \frac{\mathrm{i}}{8\pi^2} \int d^2\mathbf{k}\, k_j \mathrm{e}^{-|w-w'|\,k_{\mathrm{ip}}} \mathrm{e}^{\mathrm{i}\mathbf{k}_{\mathrm{ip}}(\mathbf{r}_{\mathrm{ip}}-\mathbf{r}'_{\mathrm{ip}})}, & j \neq w \,, \\
\Gamma_{ww}(\mathbf{r}, \mathbf{r}') &= \frac{1}{8\pi^2} \int d^2\mathbf{k}\, k_{\mathrm{ip}} \mathrm{e}^{-|w-w'|\,k_{\mathrm{ip}}} \mathrm{e}^{\mathrm{i}\mathbf{k}_{\mathrm{ip}}(\mathbf{r}_{\mathrm{ip}}-\mathbf{r}'_{\mathrm{ip}})} - \delta(\mathbf{r} - \mathbf{r}') \,.
\end{aligned} \tag{2.27}$$

For the last component, condition Eq. (2.19) has been used. As already indicated in the definitions of the coordinate systems, Fig 2.5, without loss of generality, $\mathbf{e}_v$ is chosen as propagation direction, i.e. $\mathbf{k}_{\mathrm{ip}} = k_v\mathbf{e}_v$ and $k_{\mathrm{ip}} = |k_v|$. We therefore seek for solutions of the magnetization in the form of plane waves

$$\mathbf{m}(t, \mathbf{r}) = \mathbf{m}_0(w)\mathrm{e}^{\mathrm{i}(\omega t - k_0 v)} \,, \tag{2.28}$$

with a wave vector component k_0, that can be either positive or negative. Note that k_v denotes a variable in Fourier space, while k_0 is the wave vector component of the propagating spin wave. Equation 2.28 implies that neither the dynamic magnetization nor the dynamic field depend on the second in-plane dimension u. The integration in

Eq. (2.25) can therefore be directly absorbed into the tensor via

$$\mathbf{\Gamma}(v, w, v', w') = \lim_{L_u \to \infty} \frac{1}{2L_u} \int_{-L_u}^{L_u} \mathrm{d}u \int_{-L_u}^{L_u} \mathrm{d}u' \, \mathbf{\Gamma}(\mathbf{r}, \mathbf{r}') \, .$$

Without prefactors, the integration reads

$$\lim_{L_u \to \infty} \int_{-L_u}^{L_u} \mathrm{d}u \int_{-L_u}^{L_u} \mathrm{d}u' \, \mathrm{e}^{-\mathrm{i}(u-u')k_u} = \lim_{L_u \to \infty} 4\frac{\sin^2(k_u L_u)}{k_u^2} \, .$$

This expression can be identified as Dirac delta distribution $4\pi L_u \delta(k_u)$ [51]. Hence, integrals over k_u in Eq. (2.27) are readily obtained. Afterwards, k_u can be set to zero, as we allow only for one finite component k_v. It follows that $\Gamma_{uj} = \Gamma_{iu} = 0$ as they depend on k_u. The tensor becomes effectively two dimensional and as an example

$$\Gamma_{vv}(v, w, v', w') = -\frac{1}{2\pi} \int dk_v \frac{|k_v|}{2} \, \mathrm{e}^{-|w-w'| \, |k_v|} \mathrm{e}^{\mathrm{i}k_v(v-v')} \, .$$

The expression on the right hand side coincides with the definition of an inverse Fourier transform of Γ_{vv} with respect to the pair k_v and $\tilde{v} = v - v'$. The respective Fourier components $\hat{\Gamma}_{ij}$ read

$$\hat{\Gamma}_{vv}(k_v, w, w') = -\frac{|k_v|}{2}\mathrm{e}^{-|k_v| \, |w-w'|} \, ,$$

$$\hat{\Gamma}_{vw}(k_v, w, w') = \hat{\Gamma}_{wv}(k_v, w, w') = -\mathrm{i}\,\mathrm{sign}(w-w') \frac{k_v}{2}\mathrm{e}^{-|k_v| \, |w-w'|} \, ,$$

$$\hat{\Gamma}_{ww}(k_v, w, w') = -\delta(w-w') - \hat{\Gamma}_{vv} \, . \tag{2.29}$$

These functions were used in Ref. [21, 50] to derive the full spin wave spectrum of a ferromagnetic film[1]. They can be utilized to elegantly rewrite the convolution defined in Eq. (2.25) as multiplication in k_v-space since the inner integration can be rewritten as

$$\mathbf{h}_{\mathrm{dem}} = \mathrm{FT}^{-1}(\hat{\mathbf{\Gamma}} \cdot \hat{\mathbf{m}}) \, . \tag{2.30}$$

As we only allow for waves with wave vector k_0, it holds $\hat{\mathbf{m}}(k_v) = \mathbf{m}_0\delta(k_v - k_0)$. Then, the inverse Fourier transform can be directly obtained and one integration is remaining in the out-of-plane direction w

$$< \mathbf{h}_{\mathrm{dem}} > = \int \mathrm{d}w \int \mathrm{d}w' \, \hat{\mathbf{\Gamma}}(k_0, w, w') \cdot \mathbf{m}_0(w') \, \mathrm{e}^{\mathrm{i}(\omega t - k_0 v)} \, . \tag{2.31}$$

From the definitions of $\hat{\Gamma}_{ij}$, only the off-diagonal components exhibit dependencies on the sign of k_0 and the sign of $(w - w')$. These components, that effectively mix in-plane and out-of-plane components of magnetization and field are therefore responsible for non-reciprocal phenomena of spin wave propagation. In particular, this includes the surface character of spin waves in Damon-Eshbach geometry. A numerical discussion of

---

[1]According to Refs. [48, 49], the original derivation of the functions (2.29), are found in Chartorizhskii's candidate's thesis. He is one of the authors of Refs. [48, 49].

this phenomenon is presented in Section 4.1.

Finally, the dynamic field associated with the exchange interaction can be straightforwardly derived from Eq. (2.7). It is given by

$$\mathbf{h}_{\mathrm{exc}}(w) = l_{\mathrm{exc}}^2 \Delta \mathbf{m} = l_{\mathrm{exc}}^2 \left(\frac{\partial}{\partial w^2} - k_0{}^2 \right) \mathbf{m}_0(w)\,\mathrm{e}^{\mathrm{i}(\omega t - k_0 v)}, \tag{2.32}$$

where l_{exc} was defined in Eq. (2.6).

2.6 Full Film Dispersion Relations in Thin Film Approximation

In this work, we are mainly concerned with spin waves propagating in comparably thin films with thickness L not too large with respect to l_{exc}. Then, *thin* implies a negligible dependence of the magnetization profile on the coordinate w, since exchange locks the magnetization in this direction. An assumption of a constant magnetization across the thickness is called the thin film approximation [66]. Consequently, any contributions of PSSWs are automatically disregarded. This approach will be quantitatively justified by numerically solving for the full spin wave spectrum including PSSWs in Section 4.1.

In thin film approximation, the gradient in w vanishes and therefore, by Eq. (2.32),

$$\mathbf{h}_{\mathrm{exc}} = -l_{\mathrm{exc}}^2 k_0^2 \, \mathbf{m}\,.$$

Since $\mathbf{m}$ is assumed to not depend on w, the integration in Eq. (2.31) can be performed on the Green's functions tensor across the thickness L such that

$$\hat{\boldsymbol{\Gamma}}_{\mathrm{TF}} = \frac{1}{L} \int_{-\frac{L}{2}}^{\frac{L}{2}} \mathrm{d}w \int_{-\frac{L}{2}}^{\frac{L}{2}} \mathrm{d}w' \, \hat{\boldsymbol{\Gamma}}\,.$$

This double integral without prefactors can be solved explicitly as

$$\int_{-\frac{L}{2}}^{\frac{L}{2}} \mathrm{d}w \int_{-\frac{L}{2}}^{\frac{L}{2}} \mathrm{d}w' \, \mathrm{e}^{-|k_0|\,|w-w'|} = \frac{2L}{k_0} f(|k_0 L|) \tag{2.33}$$

with the function f defined by

$$f(x) = 1 - \frac{(1 - \mathrm{e}^{-x})}{x}\,. \tag{2.34}$$

Due to their antisymmetric structure, the off-diagonal elements of $\hat{\boldsymbol{\Gamma}}_{\mathrm{TF}}$ vanish in thin film approximation and finally, the tensor can be identified as the negative dynamic demagnetizing tensor

$$\mathbf{n} = -\hat{\boldsymbol{\Gamma}}_{\mathrm{TF}} = \begin{pmatrix} 0 & 0 & 0 \\ 0 & n_{vv} & 0 \\ 0 & 0 & n_{ww} \end{pmatrix} \tag{2.35}$$

introduced in Section 2.3, with

$$
\begin{aligned}
n_{vv} &= f(|k_0 L|) \,, \\
n_{ww} &= 1 - f(|k_0 L|) \,.
\end{aligned}
\tag{2.36}
$$

Here, we have switched the terminology from $\mathbf{\Gamma}$ to $\mathbf{n}$, since n_{ij} can be considered simple geometric factors that are directly utilized to obtain dynamic fields via

$$
\mathbf{h}_{\mathrm{dem}} = - \left(\begin{array}{cc} n_{vv} & 0 \\ 0 & n_{ww} \end{array} \right) \mathbf{m} \,.
$$

In passing, it can be observed that they also fulfill the usual condition $\mathrm{tr}(\mathbf{n}) = 1$, since source and destination of this field coincide. In addition, there are no components remaining that depend on the sign of k_0. We will therefore drop the subscript in the following, since $k = |k_0| = |\mathbf{k}|$.

Now that we have obtained all dynamic fields in linear relation to $\mathbf{m}$, we are prepared to solve the linearized LLG, Eq. (2.10), defined in the xyz frame for its eigenmodes. All fields and in particular the demagnetizing field can be transformed into this frame by

$$
\mathbf{h}_{\mathrm{dem}}^{xyz} = -\mathbf{R} \cdot \mathbf{n} \cdot \mathbf{R}^{\mathrm{T}} \cdot \mathbf{m}^{xyz} \,.
$$

Note that in order to perform this rotation, $\mathbf{n}$ needs to be three dimensional. Demagnetizing, exchange, and external fields are used in the following two subsections to derive the dispersion relations $\omega(k)$ in the main geometries. When the damped LLG, Eq. (2.9), is used, the dispersion becomes complex and the imaginary part $\Im(\omega) = \frac{1}{\tau}$ can be identified as the reciprocal of a characteristic damping time τ. Its relation to the attenuation length L_{att} of a propagating spin wave is defined as [56]

$$
L_{\mathrm{att}} = v_{\mathrm{G}} \tau \,,
\tag{2.37}
$$

with $\mathbf{v}_{\mathrm{G}} = \frac{\partial \omega}{\partial \mathbf{k}}$ the group velocity. These important parameters will also be quantitatively discussed after their derivation. We distinguish between the initially mentioned main geometries Damon Eshbach (DE), backward volume (BV), and forward volume (FV), which are depicted in Fig. 2.2. DE and BV modes are described by a shared dispersion relation for the in-plane geometry in the following. Even though FV modes are not discussed experimentally, we will shortly mention their main features for completeness.

In-plane Geometry

Since $\theta = 0$ holds, $\mathbf{R}_w$ is enough to describe the in-plane spectrum with the angle $\phi = 0$ and $\phi = \pm\frac{\pi}{2}$ corresponding to BV and DE, respectively. Then, the non-vanishing demagnetizing fields read

$$
\mathbf{h}_{\mathrm{dem}}^{xyz} = \left(\begin{array}{c} h_x \\ h_z \end{array} \right) = - \left(\begin{array}{c} n_{vv} \sin^2(\phi) m_x \\ n_{ww} m_z \end{array} \right) \,.
$$

Put into the linearized LLG, Eq. (2.10), and solving the corresponding system of equations yields the in-plane dispersion relation for dipole exchange spin waves in thin film approximation

$$\omega^2 = (\gamma\mu_0)^2 \left(H + M_S l_{\mathrm{exc}}^2 k^2 + n_{vv} M_S \sin^2(\phi) \right) \left(H + M_S l_{\mathrm{exc}}^2 k^2 + n_{ww} M_S \right) . \qquad (2.38)$$

In case of finite damping, Eq. (2.9), the real part of ω will recover Eq. (2.38) while the imaginary part writes

$$\Im(\omega) = \frac{1}{\tau} = \frac{\alpha\gamma\mu_0}{2} \left(n_{ww} M_S + n_{vv} M_S \sin^2(\phi) + 2H + 2M_S l_{\mathrm{exc}}^2 k^2 \right) , \qquad (2.39)$$

when terms quadratic in α are ignored.

General expressions for the group velocity and attenuation length can be derived from these, but can be quite cumbersome. If $|kL| \ll 1$, however, exchange can be neglected and components n_{ij} are expanded as

$$n_{vv} \approx \frac{|kL|}{2} \qquad \text{and} \qquad n_{ww} \approx 1 - \frac{|kL|}{2} . \qquad (2.40)$$

Then, one can obtain expressions for group velocities of main directions to

$$v_G^{\mathrm{DE}} = \frac{\gamma^2 \mu_0^2 M_S^2 L}{4\omega} (1 - |kL|) ,$$

$$v_G^{\mathrm{BV}} = -\frac{\gamma^2 \mu_0^2 M_S L}{4\omega} H$$

and consequently the attenuation lengths to

$$L_{\mathrm{att}}^{\mathrm{DE}} = v_G^{\mathrm{DE}} \cdot \frac{2}{\alpha\gamma\mu_0(2H + M_S)} , \qquad (2.41)$$

$$L_{\mathrm{att}}^{\mathrm{BV}} = v_G^{\mathrm{BV}} \cdot \frac{2}{\alpha\gamma\mu_0(2H + M_S - M_S \frac{|kL|}{2})} .$$

With the approximations Eq. (2.40), the expressions for the in-plane dispersion relation will be used in Sec. 6.2. The attenuation length of spin waves is used in Chapter 7. Note that the main contribution to the dependence of L_{att} on the field H stems from the group velocity and hardly from the decay time.

If general expressions for group velocity and attenuation length are needed, they are computed numerically from (2.38) and (2.39). Nevertheless, it is important to note, that the radial part of the gradient, $\frac{\partial\omega}{\partial\phi} \propto \sin(2\phi)$, vanishes at the symmetry points corresponding to BV and DE modes. Therefore, the group velocity vector and wave vector will be aligned anti-parallel and parallel, respectively. In between, there is a finite radial component and therefore, $\mathbf{v}_G$ and $\mathbf{k}$ are not pointing in the same direction. Since the group velocity defines the direction of energy flow [67, 56] this has to be kept in mind when conducting refraction experiments that change the direction of $\mathbf{k}$ with respect to $\mathbf{M}$.

Out-of-plane Geometry

In the out-of-plane geometry, $\theta = \frac{\pi}{2}$, the dispersion is isotropic and reads

$$\omega^2 = (\gamma\mu_0)^2 \left(H + M_{\mathrm{S}} l_{\mathrm{exc}}^2 k^2 \right) \left(H + M_{\mathrm{S}} l_{\mathrm{exc}}^2 k^2 + n_{vv} M_{\mathrm{S}} \right)$$

for FV modes. Note that $H = H_{\mathrm{ext}} - M_{\mathrm{S}}$ as discussed in Sec. 2.4. The imaginary part is given by

$$\Im(\omega) = \frac{1}{\tau} = \frac{\alpha\gamma\mu_0}{2} \left(n_{vv} M_{\mathrm{S}} + 2H + 2M_{\mathrm{S}} l_{\mathrm{exc}}^2 k^2 \right) .$$

The group velocity and attenuation length are therefore derived to

$$v_G^{\mathrm{FV}} = \frac{\gamma^2 \mu_0^2 M_{\mathrm{S}} L}{4\omega} H$$

and

$$L_{att} = v_G^{\mathrm{FV}} \cdot \frac{2}{\alpha\gamma\mu_0(M_{\mathrm{S}} \frac{|kL|}{2} + 2H)} ,$$

respectively, by the same approximations as above.

Discussion of the Dispersion Relation for Py

Figure 2.6 shows all three main dispersion relations and respective group velocities for typical values of Permalloy with $L = 30\,\mathrm{nm}$ and a constant internal field H. In the out-of-plane case the external field H_{ext} must therefore be large enough to overcome the static demagnetizing field. In plane, $H = H_{\mathrm{ext}}$ holds. Here and henceforth, typical values, which are used for both analytical and numerical calculations, mean $\mu_0 M_{\mathrm{S}} = 1\,\mathrm{T}$, $\gamma = 185\,\mathrm{GHz\,T^{-1}}$, $A = 13\,\mathrm{pJm^{-1}}$, and $\alpha = 0.008$, resulting in $l_{\mathrm{exc}} = 5.7\,\mathrm{nm}$.

The blue shaded part marks the range that is accessible (for in-plane spin waves) with the current setup described in Sec. 3.3. FV waves are not directly accessible since they lack our experimental observable — a dynamic out-of-plane component of the magnetization.

The outstanding feature of the BV dispersion is the name-giving region of negative group velocity. Here, $\mathbf{k}$ and $\mathbf{v}_{\mathrm{G}}$ are opposed to each other. By increasing the angle ϕ, the dispersion smoothly transforms to the DE modes. There, the group velocity is largest and $\mathbf{k}$ and $\mathbf{v}_{\mathrm{G}}$ are aligned parallel. The full in-plane spin wave manifold is depicted in Fig. 2.7 **a**. The anisotropy of the propagation direction can be visualized in terms of iso-frequency plots in $\mathbf{k}$-space. Figure 2.7 **b** shows such a contour with constant frequency of $f = 8\,\mathrm{GHz}$, corresponding to the blue plane in **a**. It is noteworthy that DE modes have the smallest wave vector magnitude of all in-plane modes. Group velocities are plotted as pink arrows. It can be shown that these are always perpendicular to the iso-frequency curve [67, 68, 69]. The anisotropy gets smaller with larger wave vector until the dispersion becomes elliptic in the exchange regime, where the k^2 term dominates for all modes. The *true* BV modes, i.e. modes with negative group velocity, are not excitable for this combination of field and frequency, but rather exchange coupled spin waves with positive group velocity. Although the names of the modes originate from purely magnetostatic calculations, they nowadays describe modes that share the original geometry of $\mathbf{k}$ and $\mathbf{M}$. The FV dispersion is innately
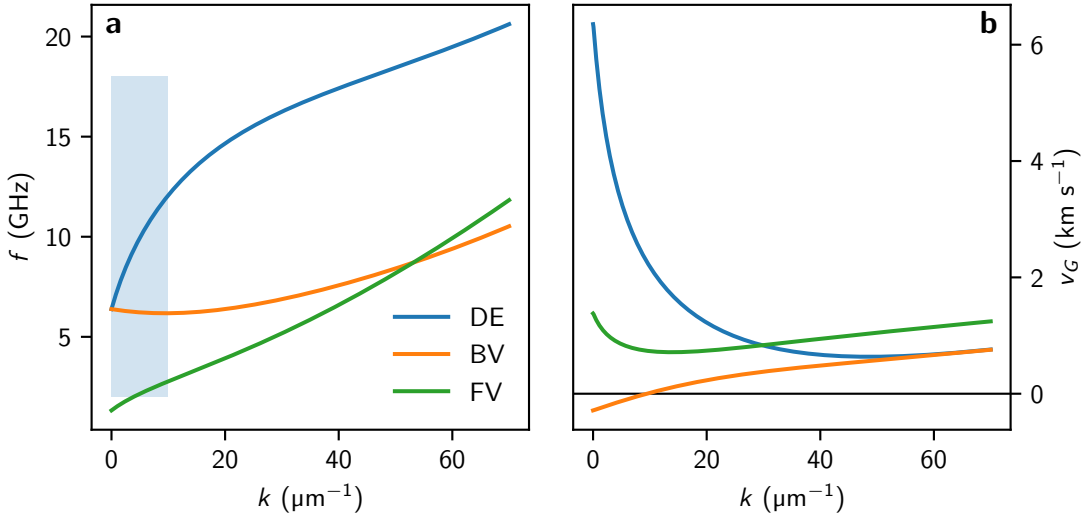
Figure 2.6: a Dispersion and **b** group velocity of the three main spin wave modes DE, BV, and FV. The curves are plotted for an internal field $\mu_0 H = 45\,\text{mT}$ and a thickness $L = 30\,\text{nm}$. All other values are the standard values of Permalloy mentioned in the main text. Group velocities are calculated numerically from the dispersion.
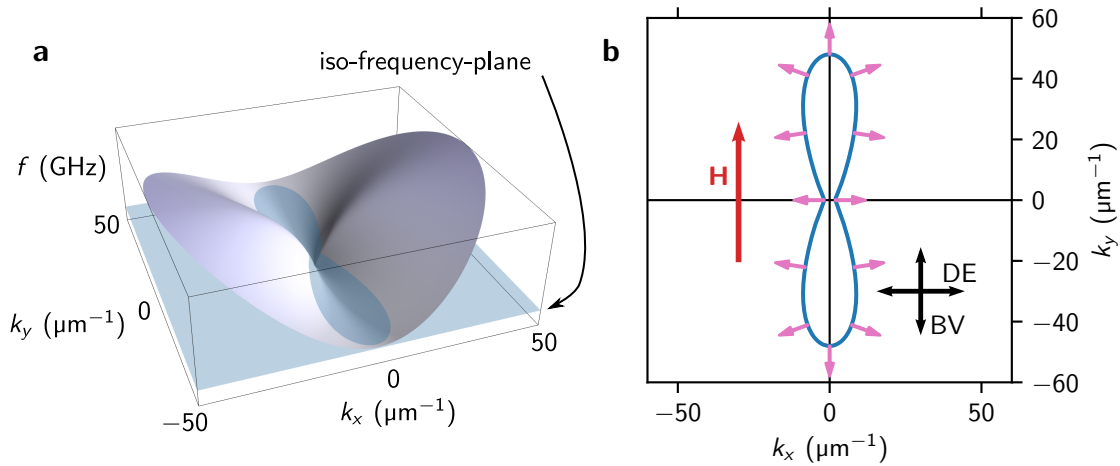
Figure 2.7: a In-plane spin wave manifold and **b** iso-frequency contour at $f = 8\,\text{GHz}$. Pink arrows give the direction of group velocity, which is always perpendicular to the iso-frequency curve and only parallel to **k** along DE and BV direction. The graphs are plotted for the same values as in Fig. 2.6.
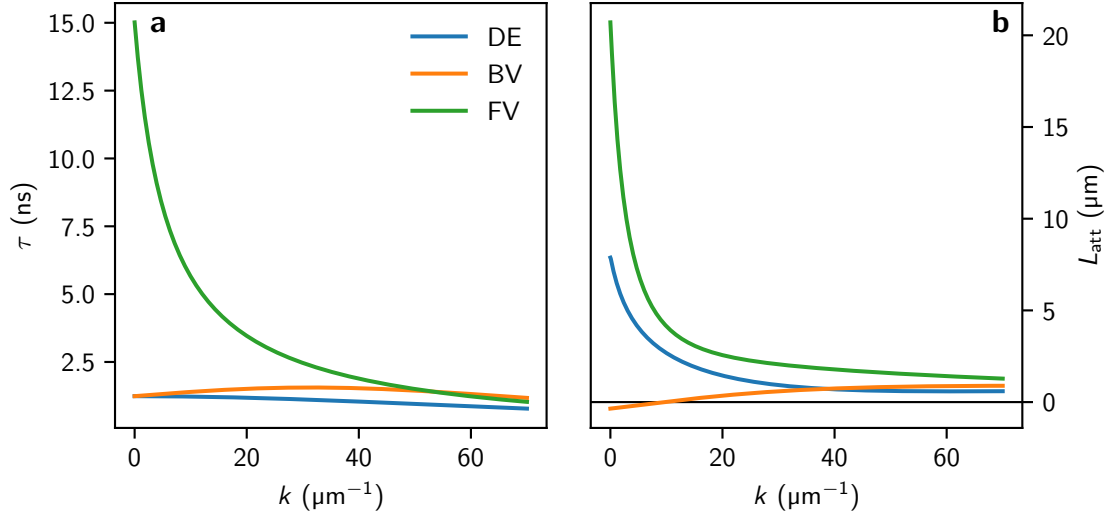
Figure 2.8: a Decay time τ and **b** attenuation length L_{att} of the three main spin wave modes DE, BV, and FV. The graphs are plotted for the same values as in Fig. 2.6. A negative attenuation length reflects the fact that group velocity and wave vector are opposed to each other.

isotropic since the respective dynamic components are subject to the same dynamic fields. In this figure, the iso-frequency curve would therefore resemble a circle with k roughly as big as in BV direction.

The decay times and attenuation lengths are shown in Fig. 2.8. Here it seems that despite a larger group velocity, FV modes are superior in terms of traveling time and attenuation length. However, from an experimental point of view it is more useful to compare the dependence of waves on the field H at constant frequency. Figure 2.9 **a** and **b** shows k and L_{att}, both vs. H, respectively. As noted, DE modes have the smallest k and are for small frequencies only excitable in a small field range. Still, DE modes have a larger attenuation length by a factor of approximately 3 for $f = 8\,\text{GHz}$ in Permalloy. This characteristic makes them attractive from an experimental point of view, since imaging is greatly facilitated. The same holds true for modes with angles close to the DE geometry.

2.7 Excitation of Propagating Spin Waves

So far, we have only considered the dispersion of spin waves without touching on the possibilities of spin wave generation. In most schemes, this is done by means of a high frequency magnetic field provided by a waveguide connected to a microwave generator. Besides thermal excitation, additional possibilities include spin Hall nanooscillators [70, 71, 72], the use of magnetic textures such as domain walls [73] or vortices [74], and optical excitation [75, 76].

In the conducted experiments of this thesis, a high frequency generator is attached to a microstructured coplanar wave guide (CPW), which acts as an antenna. The current
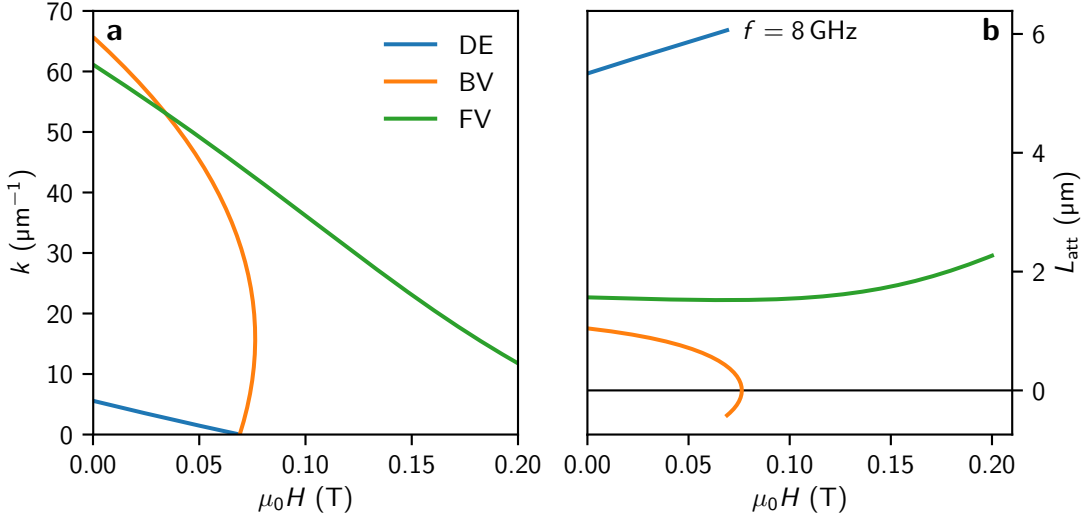
Figure 2.9: a Wave vector magnitude k and **b** attenuation length L_{att} of the three main spin wave modes vs. the internal field H. The curves are plotted for a constant frequency of $f = 8\,\text{GHz}$. All other values are identical to the ones in Fig. 2.6. To obtain the values in **a**, they have to be calculated implicitly from Eq. (2.38). A negative attenuation length reflects the fact that group velocity and wave vector are opposed to each other.

through the CPW induces a spatially inhomogenous magnetic field that can couple to the magnetization. A sketch of this situation is given in Fig. 2.10. If a spin wave is excited depends on two requisites: First, the structure of the CPW has to provide spatial frequencies in a range that matches the **k** vector of desired spin waves. This implies that its extent roughly defines the order of magnitude of the wavelength of the spin wave. Secondly, the frequency and — if applied, the static external field $\mathbf{H}_{\text{ext}}$ — have to be chosen such that the dispersion relation can be fulfilled with a finite **k** vector. In other words, the propagation characteristics are determined by the dispersion relation, i.e. the properties of the magnetic film, while the excitation efficiency is mainly determined by the structure of the antenna.

In the following, CPWs consist of two ground lines and a signal line in the micrometer range. A typical case is a signal line with width $2\,\mu\text{m}$ framed by two ground lines of width $1\,\mu\text{m}$. Each ground line is separated by $1\,\mu\text{m}$ from the signal line. The CPW is $100\,\text{nm}$ thick and consists of gold. It can be assumed to be infinitely extended in the direction of current flow.

In order to obtain an estimate of the induced field of such a structure, the 2D Biot Savart's law [65, 77]

$$\mu_0 \mathbf{h}_{\text{ext}} = \frac{1}{2\pi} \frac{\mathbf{I} \times \mathbf{r}}{r^2}$$

can be used. Here, **I** is the current assumed to flow in u-direction and, consequently, the v and w components are finite. An antenna structure can be discretized into individual current paths and their contributions to h_{ext} can be summed up. If the array consisting of

Figure 2.10: Sketch of the excitation of spin waves by a coplanar wave guide consisting of one signal (S) and two ground lines (G). This (yellow) structure acts as an antenna when attached to a high frequency generator. The so applied current through the CPW (black arrows) induces a high frequency field (orange arrows) that in turn generates spin waves (blue, **k**-vectors in green) to either side of the antenna in the magnetic medium. The figure is published in similar form in Ref. [78].
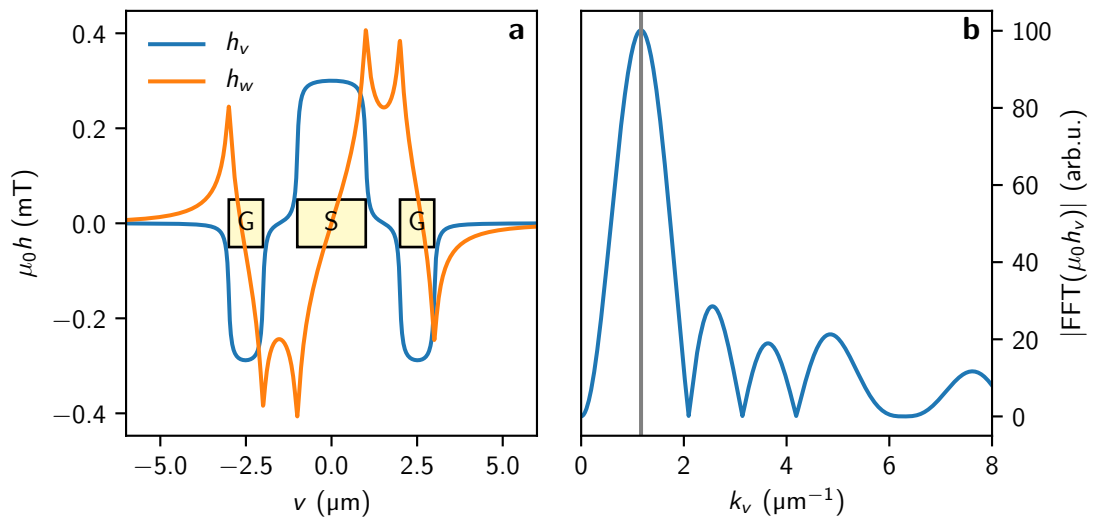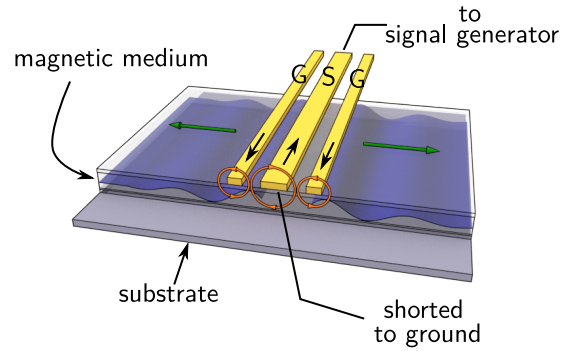
Figure 2.11: a Excitation field **h** of an antenna versus in-plane dimension v. Yellow rectangles mark the position of signal line (S) and ground lines (G) of the antenna. **b** The corresponding absolute of the fast Fourier transform (FFT) of the in-plane component, corresponding to $|\hat{h}_x|$. The gray line marks the maximal magnitude.

ground-signal-ground line is arranged in v-direction on top of a sample, the components are the in-plane and out-of-plane excitation field. Figure 2.11 **a** shows these versus v for the structure mentioned above and for a constant current distribution. In general, the current distribution is not uniform and its correct shape could be obtained numerically [77]. The fast Fourier transform of the in-plane component is shown in subplot **b**. It corresponds to the excitation efficiency for the spatial frequencies in v-direction, i.e. the wave vector components k_v that the antenna is in principle capable of exciting. The maximal efficiency corresponds to a wave with wavelength λ equal to the ground-to-ground distance of the antenna — in this case 5 µm.

In w-direction, the excitation field $\mathbf{h}_{ext}$ decreases on length scales of µm and can therefore be regarded constant for magnetic films of 60 nm thickness. In principle, however, the
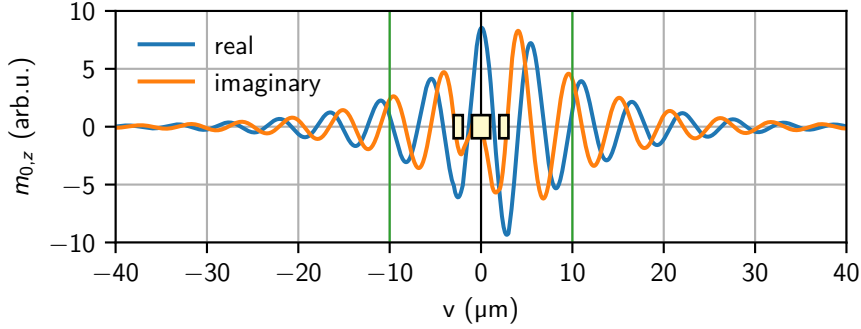
Figure 2.12: Real and imaginary part of the dynamic out-of-plane magnetization originating from an antenna structure as shown in Fig. 2.11 centered around $v = 0$ (yellow rectangles). Calculations are done in thin film approximation for standard values of Permalloy, for an external field of $\mu_0 H = 40\,\text{mT}$, $f = 8\,\text{GHz}$, and $L = 60\,\text{nm}$. By comparing m_z at $v = -10\,\mu\text{m}$ and $v = +10\,\mu\text{m}$ (green vertical lines) the excitation non-reciprocity gets visible. The external field points into the image plane.

same arguments will apply for the excitation of PSSWs. For the u-component, $\mathbf{h}_{\text{ext}}$ is by definition translational invariant, hence a plane wave with phase fronts along this direction ($k_u = 0$) will be generated on either side of the CPW.[2] These two waves will have different amplitudes, which is known as excitation non-reciprocity. The reason lies in the structure of $\mathbf{h}_{\text{ext}}$. The in-plane component is symmetric with respect to the middle of the antenna, while the out-of-plane component is antisymmetric. Roughly speaking, on one side, the precession of the magnetization is favored while on the other side it is suppressed. A quantitative discussion of this phenomenon can be conducted with the help of dynamic susceptibilities [79, 16, 80, 81, 82]. To this end, $\mathbf{h}_{\text{ext}}$ has to be introduced into the LLG, Eq. (2.10). Then, the corresponding systems of equations are most easily solved in k_v space since the integral in Eq. (2.30) is not directly solvable in real space if the structure of $\mathbf{m}$ is not a priori known. The resulting system of equations can be written as

$$\hat{\mathbf{m}} = \hat{\boldsymbol{\chi}} \cdot \hat{\mathbf{h}}_{\text{ext}} \,,$$

which defines the complex susceptibility tensor in Fourier space as $\hat{\boldsymbol{\chi}}$. It contains all information on the magnetic film's response to an external stimulus. Usually, one is interested in the real space representation of $\mathbf{m}$ which is given by

$$\mathbf{m} = \text{FT}^{-1}(\hat{\boldsymbol{\chi}} \cdot \hat{\mathbf{h}}_{\text{ext}}) \,.$$

This implies that, although $\hat{\mathbf{h}}_{\text{ext}}$ might drop to zero as depicted in Fig. 2.11, the respective modes can still be excited due to the finite extent of $\boldsymbol{\chi}$ in k_v-space.

For the antenna discussed above, the out-of-plane magnetization is depicted in Fig. 2.12. From this calculation, the non-reciprocity can be determined to

---

[2]The wavelength of photons in this frequency range is very large compared to the dimensions of the CPW such that no phase is added from this end.

$$\frac{m_0(v = 10\,\mathrm{\mu m})}{m_0(v = -10\,\mathrm{\mu m})} \approx 1.7$$

for the given values. In addition, few micrometers away from the CPW, the statement that spin waves are traveling with k_0 determined by the dispersion relation already holds. Still, for a full understanding of the excitation characteristics, it would be necessary to take the combined dynamics of film and antenna into account [83]. In many situations — including this thesis — this is not of importance and such a discussion is waived.

In addition to the targeted excitation of plane waves with an antenna, spin waves can be excited in uniform dynamic external fields. When the CPW meets the edge of the magnetic film, the translational invariance in u is broken and therefore finite $\mathbf{k}$-vector components k_u can be excited. The consequences of this behavior are investigated experimentally in Chapter 4. It is noteworthy, that this excitation mechanism can be exploited to generate spin waves without resorting to microstructured antennas [84, 69, 85]. It is therefore useful to influence the phase of spin waves by modulating the edges of the film [86, 87].

3 Methods

This Chapter starts with the description of the numerical methods, since these are closely related to the analytical formulas derived in the previous chapter. Afterwards, the experimental setup is described in Sec. 3.3.

Nowadays, micromagnetic simulations routinely accompany experimental research, since they allow to uncover and visualize physical processes or verify assumptions for analytical models in the relevant range of time (ps - ns) and length scales (nm – µm) for many experiments. In particular, they are used to solve the full LLG equation in space and time. There exist a collection of freely available solvers, e.g. [88, 89], but especially the fast GPU-based architecture and the ease of use led to a wide application of the software *mumax3* [90]. We will shortly cover the important aspects of such solvers in Sec. 3.1.

Since length scales in our experiments tend to become large (>20 µm), the general 3D solution of the magnetization trajectory by full micromagnetic solvers becomes impractical. We therefore develop a more specialized solver based on the linearized LLG equation in Sec. 3.2. During the course of this thesis, a detailed paper was published that thoroughly describes this technique [91] and together with Refs. [92, 93] coined the name dynamic matrix approach that we have adapted. Large parts of the notation and especially the dynamic fields for a stripe were used from there. However, our version of the full film approach was developed separately and follows roughly the coordinate system and formulas provided in [21]. In contrast to [91], we assume a constant static magnetization and define boundary conditions that include pinning of the magnetization for the full film solver and periodic boundary conditions for the stripe solver. The general technique is described in standard numerics textbooks [94] and was for instance used to solve Maxwell's equation for its eigenmodes, e.g. [95]. In this context it is usually referred to as finite difference frequency domain (FDFD). The results of our version of the dynamic matrix method was compared thoroughly to both analytical dispersion relations and numerical calculations found in the literature [96, 21, 97, 98, 91, 99].

3.1 Full Micromagnetic Simulations

In a typical micromagnetic simulation, the time evolution is taken into account by starting from a given magnetization pattern and using ordinary differential equation solvers like the Runge-Kutta algorithm. In most cases [88, 90] a finite difference scheme is adapted to discretize space, i.e. the magnetic medium is subdivided into a regular grid of cuboid cells. The LLG is solved by assuming a magnetization vector in the center of each cell and considering the interaction between the cells. There exist finite element solvers [89], but especially the implementation of dipolar fields heavily favors the use of a regular grid. The calculation of $\mathbf{H}_{\mathrm{dem}}$ is the most time consuming, since it depends on the whole magnetic sample and changes with the magnetization at every time step. Within the finite

difference scheme, $\mathbf{H}_\mathrm{dem}$ can be written as a convolution of a demagnetizing kernel with the magnetization. This can be implemented by exploiting the fast Fourier transform (FFT) algorithm. In Fourier space, the convolution is transformed to a multiplication, which can be rapidly calculated. FFT and the parallel calculation of the time evolution in many cells are tasks that favor the use of graphics processing units (GPU). Their use allow for a drastic increase in speed as compared to CPU based solvers.

In this work, the open source software mumax3 was used. Details of the implementation for the various field contributions can be found in Ref. [90]. Within the context of this thesis, mumax3 was mainly used to obtain static magnetization patterns as described in Sec. 6.3. For this task, the energy for a given sample structure has to be minimized. In mumax3, this is implemented by the `relax()` method that finds the minimum by ignoring the precession torque in the LLG, such that only the damping term prevails. By definition, the damping torque points towards the position of lowest energy (for every cell). This minimum is then found by propagating the system in time until the torque is small enough to cut into the noise floor of the simulation. Beyond this task, mumax3 was used as a general tool to visualize dynamic processes or confirm analytical models.

3.2 Dynamic Matrix Method

The dynamic matrix method aims at the numerical investigation of the equations developed in the previous chapter. In particular, the linearized LLG, Eq. (2.10), is solved in the xyz coordinate system. As shown there, all dynamic fields $\mathbf{h}$ in this equation can be expressed as linear combination of components of $\mathbf{m}$, which is equivalent to

$$\mathbf{h} = \mathbf{C} \cdot \mathbf{m},$$

with a 2×2 matrix $\mathbf{C}$. Then, the LLG can be written as an eigenvalue equation

$$\omega \begin{pmatrix} m_{0,x} \\ m_{0,z} \end{pmatrix} = \mathrm{i}\gamma\mu_0 \begin{pmatrix} M_\mathrm{S} C_{zx} & -H + M_\mathrm{S} C_{zz} \\ H - M_\mathrm{S} C_{xx} & -M_\mathrm{S} C_{xz} \end{pmatrix} \cdot \begin{pmatrix} m_{0,x} \\ m_{0,z} \end{pmatrix},$$

with the unknowns ω and $\mathbf{m}_0$. To take non-local fields into account, the dynamic magnetization is discretized in N cells with a finite cell size, where the magnetization is assumed to reside in the middle of the cells. In the following two subsections, we will consider both a discretization of an infinite film along its thickness as well as of an infinite stripe along its lateral, finite axis. In every cell, the LLG is solved, resulting in a system of equations represented by a $2N \times 2N$ matrix $\mathbf{D}$:

$$\omega \begin{pmatrix} m_{0,x}^{(1)} \\ m_{0,z}^{(1)} \\ \vdots \\ m_{0,x}^{(N)} \\ m_{0,z}^{(N)} \end{pmatrix} = \begin{pmatrix} D_{xx}^{11} & D_{xz}^{11} & \cdots & D_{xx}^{1N} & D_{xz}^{1N} \\ D_{zx}^{11} & D_{zz}^{11} & \cdots & D_{zx}^{1N} & D_{zz}^{1N} \\ \vdots & \vdots & \ddots & \vdots & \vdots \\ D_{xx}^{N1} & D_{xz}^{N1} & \cdots & D_{xx}^{NN} & D_{xz}^{NN} \\ D_{zx}^{N1} & D_{zz}^{N1} & \cdots & D_{zx}^{NN} & D_{zz}^{NN} \end{pmatrix} \cdot \begin{pmatrix} m_{0,x}^{(1)} \\ m_{0,z}^{(1)} \\ \vdots \\ m_{0,x}^{(N)} \\ m_{0,z}^{(N)} \end{pmatrix}.$$

The superscript letter of the magnetization components indicates the cell index $\alpha = 1 \ldots N$. The 2×2 block diagonal components $D^{\alpha\alpha}$ represent local interactions within a single cell, while off-diagonal components $D^{\alpha\beta}$ represent coupling between individual cells. The parameter β denotes the source cell of the respective interaction. The coupling strength is determined by the constants C_{ij} that include linear combinations of relevant energy contributions. They have to be determined as described in the following subsections. Then, **D** consists of numeric values and there exists a range of algorithms to solve such numerical eigenvalue problems. In the present case, algorithms provided through the package *numpy* in the *python* programming language have been used. Sample scripts can be found in Appendix B.

This procedure results in $2N$ eigenvalue/eigenvector pairs representing the frequencies and modal profiles of the normal modes of spin waves for the respective geometry. Note that in general one obtains N positive ω and N negative ω with normally the same absolute values. Since the magnetization is implicitly assumed to have the form $\mathbf{m} = \mathbf{m}_0 \exp(\mathrm{i}\,(\omega t - k_0 v))$, positive (negative) ω represent waves traveling in positive (negative) v-direction. Note that in this thesis we will only consider the modes with $\omega > 0$. Each unique pair $(\omega, \mathbf{m}_0)$ represents one eigenmode of the system calculated for a given in-plane k_0. In the case of the full film, these are the PSSWs and in the case of a stripe, the standing waves across the stripe width. It should be pointed out that $\mathbf{m}_0$ is in general complex but in all cases considered here, $m_{0,x}$ is purely real and $m_{0,z}$ is purely imaginary. In the following, we will therefore omit an explicit mentioning of real and imaginary parts. The full time and space evolution can be obtained by taking the real or imaginary part of $\mathbf{m}$.
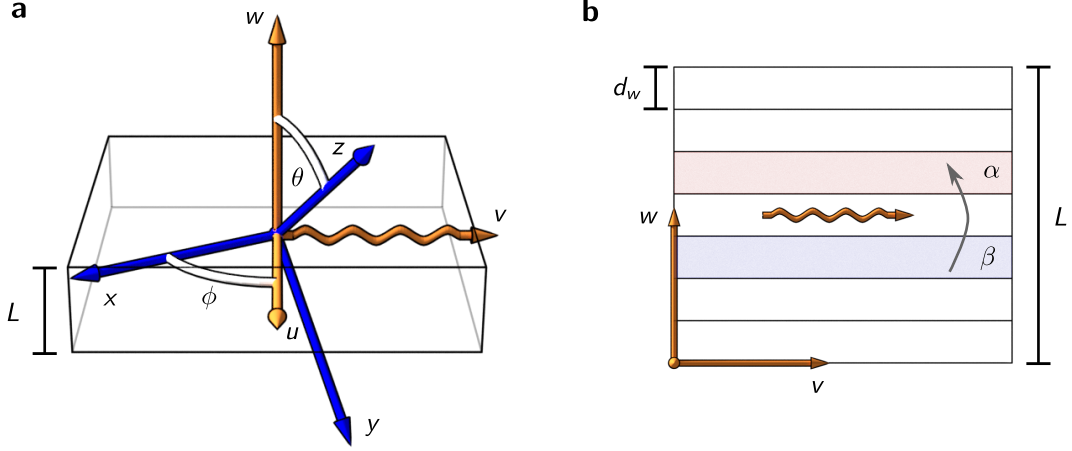
3.2.1 Full Film

This section aims to give the recipe to write a solver for the full dispersion relation for spin waves traveling in the plane of an infinitely extended film. We will use the same coordinate systems as in the previous chapter: The wave is always traveling along v in the laboratory frame, while the magnetization is attached to the xyz system, see Fig. 3.1 **a**. The full film of thickness L is discretized in laterally infinite slabs of finite thickness d_w as shown in **b**.

As mentioned in Sec. 2.4, the static magnetization is not necessarily aligned parallel with the external field H_{ext}. To find the equilibrium position — which is assumed to be the same in every cell — the two equations

$$H = H_{\text{ext}}\cos\left(\theta - \theta_H\right) - M_{\text{S}}\sin^2\left(\theta\right) ,$$
$$0 = H_{\text{ext}}\sin\left(\theta - \theta_H\right) + M_{\text{S}}\sin\left(\theta\right)\cos\left(\theta\right)$$

defined in Eq. (2.24) are numerically solved for a given field angle and strength by a standard solver. As a result, we obtain θ and H, where the former will be used to transform the dynamic fields into the correct coordinate system, while the latter directly contributes to $D^{\alpha\alpha}$. The dynamic fields that have to be considered are the same as for the analytical derivations, namely exchange and demagnetizing fields.

In order to discretize the differential operator, Eq. (2.32), one usually only includes the

Figure 3.1: Coordinate system used for the dynamic matrix method. **a** shows the transformation between magnetization coordinate system xyz and wave coordinate system uvw, as introduced in Sec. 2.4. In **b**, the full film with thickness L is discretized into laterally infinitely extended slabs with thickness d_w. The index β denotes a source cell and α denotes a destination cell.

nearest neighbor cells, i.e. $\beta = \alpha - 1$, and $\alpha + 1$ in the usual finite difference way [100, 94] such that

$$\mathbf{h}_{\text{exc}}^{(\alpha)} = l_{\text{exc}}^2 \nabla^2 \mathbf{m}(\mathbf{r}) = (-k_0^2 l_{\text{exc}}^2 + l_{\text{exc}}^2 \frac{\partial^2}{\partial w^2}) \mathbf{m}_0 e^{\mathrm{i}(\omega t - k_0 v)}$$

$$= -k_0^2 l_{\text{exc}}^2 \mathbf{m}^{(\alpha)} + \frac{l_{\text{exc}}^2}{d_w^2} (\mathbf{m}^{(\alpha-1)} - 2\mathbf{m}^{(\alpha)} + \mathbf{m}^{(\alpha+1)})$$

and, therefore, e.g.

$$C_{xx}^{\alpha\alpha} = -k_0^2 l_{\text{exc}}^2 - \frac{2l_{\text{exc}}^2}{d_w^2} \quad \text{and} \quad C_{xx}^{\alpha,\alpha-1} = \frac{l_{\text{exc}}^2}{d_w^2} \, .$$

Obviously, at the boundaries, $\alpha = 1$ and $\alpha = N$, there is a need for defined exchange boundary conditions. They are cast in the form of so called Rado-Wertmann type and described in the following subsection.

The demagnetizing fields can be separated into *mutual* and *self* interacting terms. The former denotes interactions where cell $\alpha \neq \beta$ and the latter where $\alpha = \beta$. The self interaction term has been previously obtained: We assume a constant magnetization within one slab. Hence, the propagation corresponds directly to the thin film approximation derived in Sec. 2.6. One can directly use the tensor $\mathbf{n}$, see Eq. (2.35), and transform it into the xyz coordinate system by

$$\mathbf{h}_{\text{dem,self}}^{(\alpha)} = -\mathbf{R}\mathbf{n}\mathbf{R}^{\mathrm{T}}\mathbf{m}^{(\beta=\alpha)} \, .$$

The mutual interaction between cells of distance $d_{\alpha\beta} = i \cdot d_w$, with an integer $i \neq 0$, can be taken into account by adjusting the integral limits in Eq. (2.31) to cover a source different from the destination and can be calculated analytically as

$$n_{vv}(d_{\alpha\beta}) = \int_{-\frac{d_w}{2}}^{\frac{d_w}{2}} \mathrm{d}w \int_{-\frac{d_w}{2}+d_{\alpha\beta}}^{\frac{d_w}{2}+d_{\alpha\beta}} \mathrm{d}w' \mathrm{e}^{-|k_0|\,|w-w'|} = -\frac{2\sinh^2\left(\frac{|k_0|d_w}{2}\right)}{|k_0|\,d_w}\mathrm{e}^{-|k_0|\,|d_{\alpha\beta}|}\,.$$

Here the non-diagonal components do not vanish and the evaluation of the corresponding integrals yield the mutual tensor

$$\mathbf{n}_{\mathrm{mut}}^{\alpha\beta}(k_0, d_{\alpha,\beta}) = \begin{pmatrix} 0 & 0 & 0 \\ 0 & n_{vv} & -\mathrm{i}\,\mathrm{sign}(d_{\alpha\beta})\,\mathrm{sign}(k_0)\,n_{vv} \\ 0 & -\mathrm{i}\,\mathrm{sign}(d_{\alpha\beta})\,\mathrm{sign}(k_0)\,n_{vv} & -n_{vv} \end{pmatrix}\,. \tag{3.1}$$

Finally the demagnetizing field in cell α can be written as

$$\mathbf{h}_{\mathrm{dem}}^{(\alpha)} = -\mathbf{R}\mathbf{n}\mathbf{R}^{\mathrm{T}}\mathbf{m}^{(\beta=\alpha)} - \sum_{\beta=1}^{N} \mathbf{R}\mathbf{n}_{\mathrm{mut}}\mathbf{R}^{\mathrm{T}}\mathbf{m}^{(\beta\neq\alpha)}\,.$$

Exemplary,

$$C_{xx}^{\alpha\alpha} = (\mathbf{R}\mathbf{n}\mathbf{R}^{\mathrm{T}})_{xx} \quad \text{and} \quad C_{xx}^{\alpha\beta} = (\mathbf{R}\mathbf{n}_{\mathrm{mut}}(d_{\alpha\beta})\mathbf{R}^{\mathrm{T}})_{xx}\,.$$

The respective interaction constants C from exchange and demagnetizing fields (and potentially other fields) can be summed up and the matrix $\mathbf{D}$ is complete. An evaluation of $\mathbf{D}$ yields the frequency spectrum for one value of k_0. If $\mathbf{D}$ is recalculated for different k_0, the full film dispersion relation for in-plane propagating spin waves can be obtained for a given geometry of $\mathbf{M}$ and $\mathbf{k}$. Usually, only the lowest PSSW modes are of interest due to their moderate frequencies. An example is given in Fig. 3.2 **a**, where the DE dispersion relation for a Py film of thickness $L = 30\,\mathrm{nm}$ is shown. The corresponding modal profiles across the thickness depicted in **b** are close to sine/cosine like standing waves and are accordingly numbered with an integer n. This is straightforwardly possible in cases where the modes are well separated in energy. By contrast, especially for larger thicknesses, the modes may hybridize. Such a case will be investigated in Sec. 4.1.
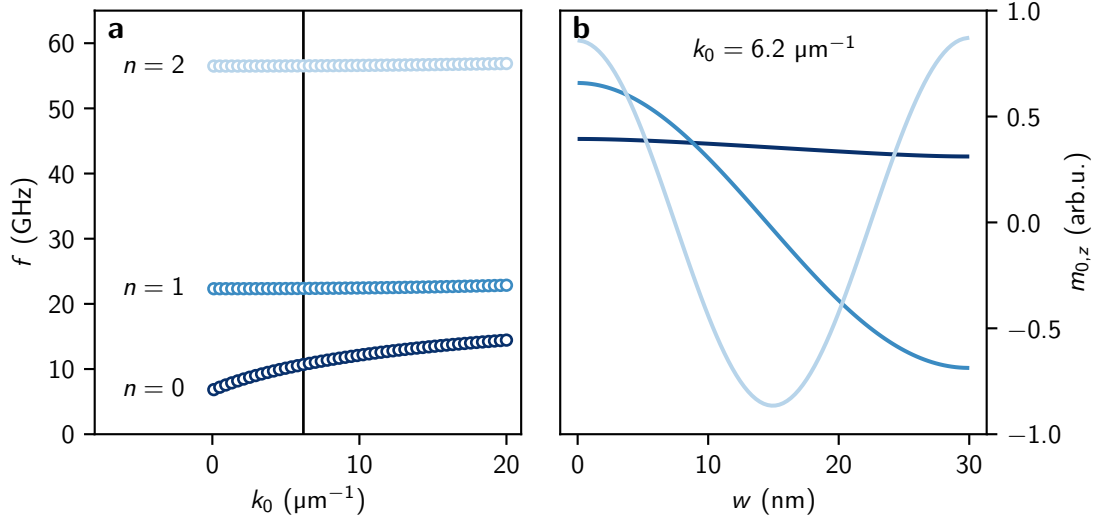
Discretization of Boundary Conditions

From the definiton of $\mathbf{h}_{\mathrm{exc}}$ it is obvious that at $\alpha = 1$ and $\alpha = N$ boundary conditions are needed. The generally accepted way [100, 91] is the use of unpinned boundary conditions of the form

$$\frac{\partial \mathbf{m}}{\partial w} = 0\,. \tag{3.2}$$

Alternatively, sometimes pinned boundary conditions are applied:

$$\mathbf{m} = 0\,. \tag{3.3}$$

Figure 3.2: Example for the full film dynamic matrix method. **a** shows the dispersion relation for a Py film with thickness $L = 30\,\mathrm{nm}$ in DE geometry for $\mu_0 H = 50\,\mathrm{mT}$. It is discretized into 100 cells yielding cell sizes well below the exchange length. The dynamic out-of-plane magnetization in these cells is shown in **b** for the three crossing points of the vertical black line in **a**.

If cell sizes are small enough, it is a good approximation to absorb these boundary conditions directly into the cells at the boundary, e.g.

$$\mathbf{h}_{\mathrm{ex}}^{(1)} = -k_0^2 l_{\mathrm{ex}}^2 \mathbf{m}^{(1)} + \frac{l_{\mathrm{ex}}^2}{d_w^2}\left(\mathbf{m}^{(2)} - \mathbf{m}^{(1)}\right),$$

which directly implies that the derivative towards an imaginary cell with index 0 is zero, thus fulfilling Eq. (3.2). For a pinned magnetization, $\mathbf{m}^{(1)}$ can be forced to zero by setting the two boundary matrices $\mathbf{D}^{11}$ and $\mathbf{D}^{NN}$ to zero.

The more sound approach is the use of a pinning parameter d_{pin} that can vary the degree of pinning between these two extreme cases. The pinning parameter for the exchange boundary conditions was introduced for a static out-of-plane magnetization by Rado and Wertmann [46] and generalized for arbitrary directions of magnetization by Soohoo [47]. In the literature, the name *Rado-Wertmann boundary conditions* is customary. In Refs. [46, 47], the pinning is induced by a uniaxial anisotropy that can arise due to oxidation of the surface. In our coordinate system, they read for the bottom surface

$$\frac{\partial m_x}{\partial w} - d_{\mathrm{pin}}^{(0)}\sin^2(\theta)\,m_x = 0, \qquad \frac{\partial m_z}{\partial w} + d_{\mathrm{pin}}^{(0)}\cos^2(2\theta)\,m_z = 0 \qquad \text{at } w = 0 \qquad (3.4)$$

and for the top surface

$$\frac{\partial m_x}{\partial w} + d_{\mathrm{pin}}^{(L)}\sin^2(\theta)\,m_x = 0, \qquad \frac{\partial m_z}{\partial w} - d_{\mathrm{pin}}^{(L)}\cos^2(2\theta)\,m_z = 0 \qquad \text{at } w = L. \qquad (3.5)$$

The pinning parameters are defined by

$$d_{\text{pin}} = -\frac{K_{\text{uni}}}{A}$$

and can account for different anisotropy constants K_{uni} at the top and bottom surface. If the boundary conditions are cast in this form, the anisotropy axis is assumed to be parallel to the film normal. If $K_{\text{uni}} > 0$, the anisotropy is of the easy axis type, while $K_{\text{uni}} < 0$ has a hard axis along the sample normal and therefore an easy plane in the plane of the sample surface. It is noteworthy that expressions of the form

$$\frac{\partial \mathbf{m}}{\partial w} + d_{\text{pin}}\mathbf{m} = 0$$

can also be derived to account for magnetostatic interactions at the lateral boundaries of stripes [101, 102].

In the discretized model, we absorb the boundary conditions into the exchange operator $l_{\text{ex}}^2 \nabla^2$ for $\alpha = 1$ and $\alpha = N$ by following the approach in [103]: We directly assume the boundary condition to apply at the film boundary and therefore at the cell boundary. At the bottom surface, the operator in cell $\alpha = 1$ is discretized via a series of Taylor expansions to

$$\frac{\partial^2 m_x}{\partial w^2} \approx \frac{1}{2d_w^2 \left(d_w d_{\text{pin}} + 3\right)} \left(-13 d_w d_{\text{pin}} - 10\right) m_x^{(1)}$$
$$+ \left(6 d_w d_{\text{pin}} + 12\right) m_x^{(2)} + \left(-d_w d_{\text{pin}} - 2\right) m_x^{(3)}. \tag{3.6}$$

The steps towards this equation are given in Appendix A.

If applied to a Py film of thickness $L = 60\,\text{nm}$, which is magnetized out-of-plane by an external field of $\mu_0 H_{\text{ext}} = 1.05\,\text{T}$, the modal profiles of the first PSSW mode with $k_0 = 1\,\mu\text{m}^{-1}$ will change as shown in Fig. 3.3. At the boundaries, both magnetization components change gradually from zero slope (unpinned boundary condition) to zero amplitude (pinned boundary condition).

3.2.2 In-plane Magnetized Stripe

The dynamic matrix approach for a stripe differs in the arrangement of discretization. Here, the cells are chosen as shown in Fig. 3.4. In contrast to the previous section, two choices are made that directly aim at utilizing this method more appropriately for the experimental circumstances described in Chapter 8. First, a coordinate system is chosen where the uvw frame is aligned with the xyz magnetization frame, i.e. $\theta = \phi = 0$. The derivation of the different contributions can therefore be directly carried out in the xyz magnetization frame and there are no static demagnetizing effects, such that $H = H_{\text{ext}}$ in every cell. As a consequence, the wave is traveling along y-direction, $k_y = k_0$, and also the static magnetization is pointing in y-direction. Within a cell, we assume that the magnetization is constant in x and z-directions. Second, we take advantage of the linear dependence of H on $\mathbf{m}$ and choose H as eigenvalue for the following discussion. This is
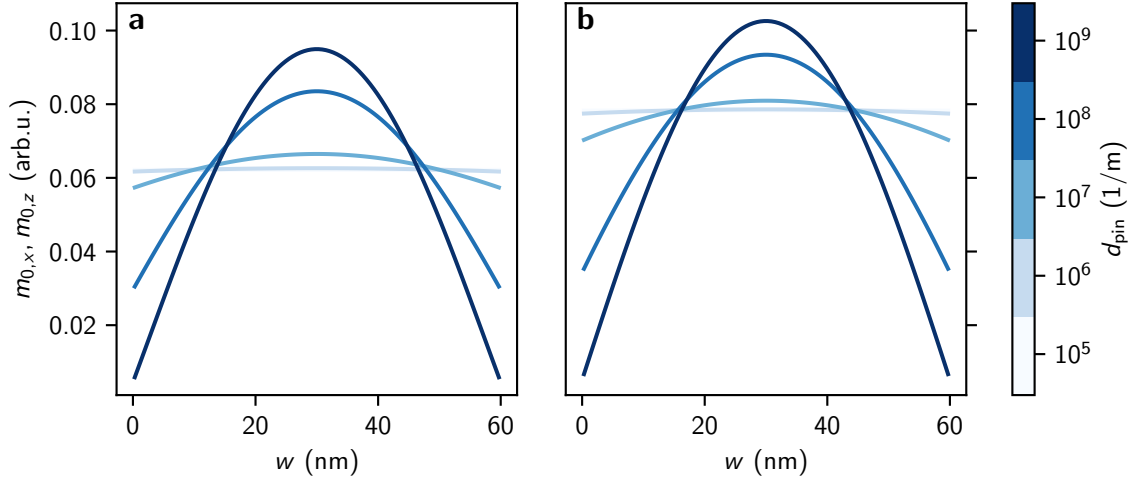
Figure 3.3: Dynamic in-plane magnetization components $m_{0,x}$ and $m_{0,z}$ are shown in subplots **a** and **b**, respectively. Different shades of blue illustrate different pinning parameters d_{pin} as indicated with the colorbar on the right. The profiles are calculated for a Py film of thickness $L = 60\,\text{nm}$ in FV geometry with $k_0 = 1\,\text{µm}^{-1}$, $N = 100$, and an internal field of $\mu_0 H = 50\,\text{mT}$.

done by rewriting the LLG with the field separated to the left as

$$
H \cdot \begin{pmatrix} m_{0,x} \\ m_{0,z} \end{pmatrix} = \begin{pmatrix} M_{\text{S}} C_{xx} & -\text{i}\dfrac{\omega}{\mu_0 \gamma} + M_{\text{S}} C_{xz} \\ \text{i}\dfrac{\omega}{\mu_0 \gamma} + M_{\text{S}} C_{zx} & M_{\text{S}} C_{zz} \end{pmatrix} \cdot \begin{pmatrix} m_{0,x} \\ m_{0,z} \end{pmatrix} , \qquad (3.7)
$$

which changes the order within a sub-matrix $\mathbf{D}^{\alpha\beta}$. This allows us to choose a fixed value of ω and get all possible values of H in a single evaluation of $\mathbf{D}$, which resembles our experiments, where usually ω is constant and H is varied. Note that this might yield negative values of H without physical meaning, since H is defined as the magnitude of a vector.

In contrast to the previous section, magnetic charges exist in all directions, so no component of the demagnetizing tensor is in general zero. Nevertheless, if the cells are arranged in a one dimensional array, it follows $n_{xz} = n_{zx} = n_{yz} = n_{zy} = 0$. This is due to the implicit thin film approximation in this geometry. In addition, components n_{yy}, n_{xy}, and n_{yx} can be excluded from the discussion, since h_y and m_y are zero by definition of the coordinate system. The remaining components n_{xx} and n_{zz} cannot be calculated explicitly, but have to be obtained by numerical integration. In Ref. [91], the respective integrals are given in Eqs. (38) – (41)[1]. As described there, their numeric values can be obtained by numerical integration using the *vegas* algorithm [104] provided for *python* in Ref. [105].

Exchange can be accounted for in the same manner as in the full film approach, with the discretization of the exchange operator along x-direction. An example evaluation for the stripe is shown in Fig. 3.5. One evaluation of a matrix yields all fields shown in **a** and the corresponding modal profiles in **b**. The profiles resemble standing waves in DE

---

[1] n_{xx} and n_{zz} and are called n_{ww} and n_{vv}, respectively, in their coordinate system.
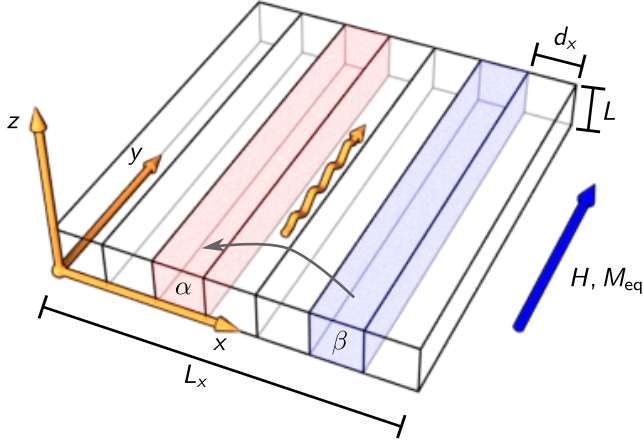
Figure 3.4: Discretization of cells in the DM approach for a stripe with finite width L_x and finite thickness L. The cells are arranged in x-direction and resemble rectangular bars, infinitely extended in y-direction and with finite width d_x. The vector $\mathbf{e}_y$ is the direction of (implicit) wave propagation and also the direction of the static magnetization. As in Fig. 3.1, the index β denotes a source cell and α denotes a destination cell.
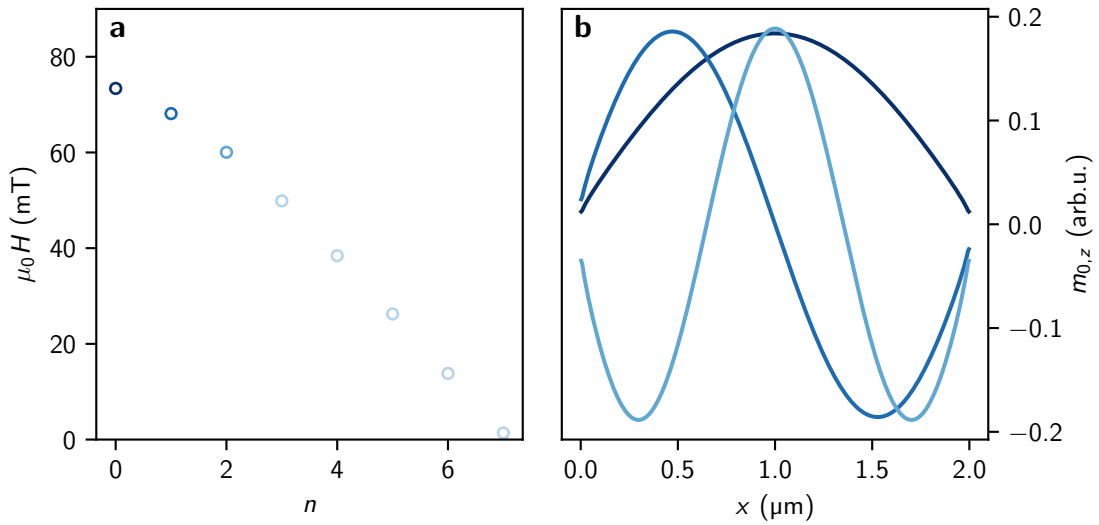
Figure 3.5: Example of the dynamic matrix method for a Py stripe of width $L_x = 2\,\mu m$ and thickness $L = 20\,nm$. It is discretized as shown in Fig. 3.4 into $N = 400$ cells with a wave with $k_y = 10\,\mu m^{-1}$ propagating in y-direction. **a** shows the fields associated with the different modes for a constant frequency of $f = 8\,GHz$. They are ordered with a mode-number n corresponding to the close-to-harmonic profiles shown in **b**.

geometry across the stripe width, while they are traveling in BV geometry along y.

Boundary Conditions

In the dynamic matrix approach for a stripe, we employ free exchange boundary conditions along the lateral edges. As described above, they are taken into account by rewriting the exchange operator in the zeroth cell as

$$\mathbf{h}_{\text{ex}}^{(1)} = -k_y^2 l_{\text{ex}}^2 \mathbf{m}^{(1)} + \frac{l_{\text{ex}}^2}{d_x^2}(\mathbf{m}^{(2)} - \mathbf{m}^{(1)}),$$

and correspondingly for cell $\alpha = N$. It is also possible to use periodic boundary conditions in the x-direction. It is straightforward to rewrite the exchange field in the first cell as

$$\mathbf{h}_{\text{ex}}^{(1)} = -k_y^2 l_{\text{ex}}^2 \mathbf{m}^{(1)} + \frac{l_{\text{ex}}^2}{d_w^2}(\mathbf{m}^{(N)} - 2\mathbf{m}^{(1)} + \mathbf{m}^{(2)})$$

and in the last cell as

$$\mathbf{h}_{\text{ex}}^{(N)} = -k_y^2 l_{\text{ex}}^2 \mathbf{m}^{(N)} + \frac{l_{\text{ex}}^2}{d_w^2}(\mathbf{m}^{(N-1)} - 2\mathbf{m}^{(N)} + \mathbf{m}^{(1)}).$$

Thus, the exchange is wrapped around the stripe.

The demagnetizing fields can also be cast in periodic form. One assumes that the stripe is extended in $\pm x$. In each direction, another array of N cells (with indices $\beta = -N+1\ldots 0$ and $\beta = N+1\ldots 2N$) is appended. If these new "stripes" have the same modal structure $\mathbf{m}(x)$ as the original stripe, one can treat their influence by a linear combination of a set of demagnetizing factors with $\mathbf{m}(x)$. Obviously, the demagnetizing factors need to be calculated with the appropriate distance to the original stripe. Afterwards, the sum of fields originating from inside and outside of the simulation domain give the dynamic demagnetizing fields

$$\mathbf{h}_{\text{dem}}^{(\alpha)} = -\mathbf{n}\mathbf{m}^{(\beta=\alpha)} - \sum_{\beta=1}^{N} \mathbf{n}_{\text{mut}}^{\alpha\beta}\mathbf{m}^{(\beta\neq\alpha)} - \sum_{\beta=-N+1}^{0} \mathbf{n}_{\text{mut}}\mathbf{m}^{(\beta\neq\alpha)} - \sum_{\beta=N+1}^{2N} \mathbf{n}_{\text{mut}}\mathbf{m}^{(\beta\neq\alpha)}.$$

In order to achieve "true" PBC, one would need to add fields from even further away, yielding an infinite series of demagnetizing fields. But since $L_x \gg L_z$ in the simulations considered here, the demagnetizing factors decrease rapidly with distance and the series can be used in the above form in good approximation.

Applied to the same values as for normal boundary conditions, the dispersion and corresponding modal profiles are shown in Fig. 3.6. Since x is periodically continued, the zeroth mode is now constant. The traveling wave along y implicitly assumed in the calculations corresponds to the pure BV case. For mode numbers $n > 0$, the profiles exhibit sine and cosine like standing waves that are pairwise degenerate, since they share the same wave vector component k_x. If dynamic fields are calculated for $k_y \to 0$, these profiles would be the DE modes in thin film approximation. For these limiting cases (and for arbitrary wave vector components) the associated field H could also be obtained by the
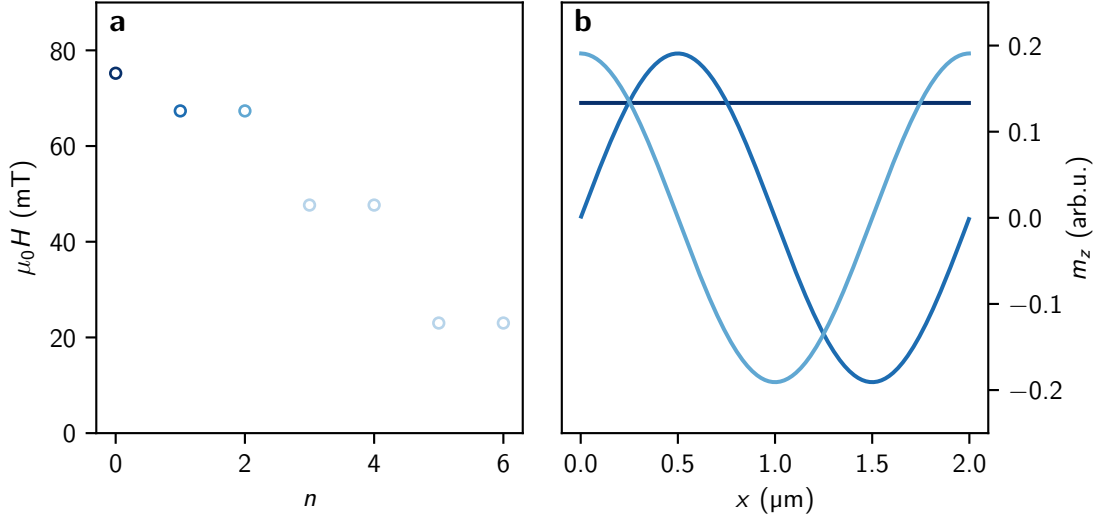
Figure 3.6: Example of the dynamic matrix method for a Py stripe with periodic boundary conditions in x-direction. The values for the calculations are the same as in Fig. 3.5. **a** shows the fields associated with the different modes for a constant frequency of $f = 8\,\text{GHz}$. The first three modes are shown in **b** versus x.

analytical dispersion relation deduced in Section 2.6. Since both analytical and numerical model share the thin film approximation, they should coincide up to numeric accuracy, which is usually given by the errors caused by the integration of the dynamic demagnetizing factors. The comparison of the two was therefore used to verify the model. Note that in a real film, k_x can be continuous, but the PBC in the exchange and demagnetizing fields prohibit non-smooth $\mathbf{m}$ between cell 1 and cell N, thus only allowing $k_x = \nu \pi L_x^{-1}$ with an integer ν.

3.3 Time Resolved Scanning Kerr Microscopy

The time resolved scanning Kerr microscope has been widely used to study magnetization dynamics and in particular spin waves [52, 106, 107, 16, 108]. TRMOKE is an optical pump-probe technique. In our setup, the pump is a microwave source with angular frequency $\omega = 2\pi f$ that is connected to a micro-structured antenna (cf. Sec. 2.7) thereby exciting coherent spin waves with the same frequency f in the GHz range. The repetition rate of the probing laser pulses f_{rep} has a constant phase with respect to f and with the help of the polar magneto-optic Kerr effect, the out-of-plane component of the magnetization can be probed. Since the duration of one laser pulse is very short with respect to one period of the excitation, the magnetization is only probed at one distinct phase. Since we are able to actively change (and stabilize) this phase, the technique more accurately allows for a phase resolution rather then a time resolution. It also implies, that f is limited to multiples of $f_{\text{rep}} = 80\,\text{MHz}$, since only then the phase can be constant. During the preparation of this thesis, there were attempts to overcome this restriction with the

help of a technique called either *undersampling* or *super-Nyquist sampling* [109]. Since the experimental results in the following sections were not obtained with this technique, it will be only shortly described in Appendix C.

Two similar setups are used, which only differ in the wavelength of the probing laser light and the mechanical parts. Although there are slight deviations, e.g. in the penetration depth into the magnetic material and magneto-optical constants between the wavelengths, these can be neglected in Py, as long as one is not interested in an absolute signal. For this reason, only the setup with $\lambda \approx 400\,\mathrm{nm}$ is described in the following sections. Similar descriptions can be found in previous theses [110, 111, 112, 113]. Before the technical details of the setup are described, a short introduction to the magneto optical Kerr effect is given following Refs. [114, 115, 65].

3.3.1 Magneto-Optical Kerr Effect

The magneto-optical Kerr effect (MOKE) describes the interaction of light with a ferromagnetic medium upon reflection and is closely related to the Faraday effect that describes the interaction during transmission. Its dependence on the direction of magnetization with respect to the direction of light $\mathbf{k}_{\mathrm{light}}$ allows the determination of hysteresis loops in in- and out-of-plane configurations of $\mathbf{M}$. For this reason, the MOKE is usually classified into polar ($\mathbf{M} \parallel \mathbf{k}_{\mathrm{light}} \parallel \mathbf{n}$, with $\mathbf{n}$ the sample normal), longitudinal ($\mathbf{M} \parallel \mathbf{k}_{\mathrm{light,ip}}$, with $\mathbf{M}$ in the sample plane and $\mathbf{k}_{\mathrm{light,ip}}$ the in-plane projection of $\mathbf{k}_{\mathrm{light}}$), and transverse ($\mathbf{M} \perp \mathbf{k}_{\mathrm{light,ip}}$, with $\mathbf{M}$ in the sample plane). The first two are characterized by a change of polarization from linearly to elliptically polarized, with the main axis of the ellipse rotated with respect to the polarization axis of the incident light. The transverse MOKE influences the intensity of light.

In this thesis, exclusively the polar MOKE is exploited. Both the rotation of the main axis of polarization and the ellipticity depend linearly on the magnitude of out-of-plane magnetization. Especially the former is easy to measure by means of crossed polarizes or a Wollaston prism, the latter detailed in the next subsection. Besides, at normal incidence, transverse and longitudinal effects vanish and a pure out-of-plane sensitivity is reached. In all other configurations, a mixture of these effects is measured.

The MOKE can be macroscopically understood with the help of the permittivity tensor $\boldsymbol{\epsilon}$ that describes the response of a medium to an external electric field, in this case light. It exhibits off-diagonal elements in the presence of spin-orbit coupling. For a magnetization pointing out-of-plane [65], it writes

$$\boldsymbol{\epsilon} = \epsilon_0 \epsilon_r \begin{pmatrix} 1 & \mathrm{i}Q & 0 \\ -\mathrm{i}Q & 1 & 0 \\ 0 & 0 & 1 \end{pmatrix},$$

with Q the magneto-optic parameter. The existence of these off-diagonal components is characteristic for a material exhibiting the MOKE. They lead to different complex refractive indices n for left ($+$) and right ($-$) circularly polarized light, i.e.

$$n^\pm \propto 1 \pm \frac{1}{2}Q\,.$$

As a consequence, the absorption of light is also different for $+$ and $-$ modes. When linearly polarized light — a superposition of circularly polarized light — is reflected from such a medium, one mode gets suppressed and elliptically polarized light will be detected.

3.3.2 Scanning Microscope

The optical components used to probe the MOKE are shown in Fig. 3.7. The main light source is a *Mira 900* mode locked Ti:Sa laser that emits laser pulses with a center wavelength of around 800 nm and a pulse length of around 120 fs with a repetition rate of 80 MHz. It is pumped by a *Laser quantum finesse* Nd:YAG laser. With a pump power of 10 W, a mean *Mira* output power of 1–2 W can be achieved. Further details of the dynamic part of this setup are given in the next section. The pulses are frequency doubled with the help of a barium borate crystal (BBO) that allows for conversion efficiencies of around 10%. The blue part of the resulting beam is filtered out and scaled to an appropriate power, usually few mW. Then, its diameter is adjusted with the help of a telescope before it enters the microscope via a periscope. After a polarizer, a pellicle (transmission ~92%) is used to reflect a small portion of the light onto an objective lens. The latter focuses the beam onto the sample. After reflection from the sample, the polarization has changed due to the polar MOKE, given a finite out-of-plane component of magnetization. The beam passes the pellicle again and the high transmission of the pellicle is now advantageous since most of the light carrying the magnetic information is transmitted. The latter is investigated with the help of a Wollaston prism, that splits the beam into two parts with perpendicular polarization. The optical axis of the prism is rotated by 45° with respect to the axis of the polarizer. Therefore, if the sample has not caused a change in polarization, the two beams after the Wollaston prism have the same intensity. A rotation of polarization is detected as the difference of intensity of the two beams, recorded by two photodiodes. In our experiments, this difference is the main measurement quantity called the Kerr signal. It is directly proportional to the out-of-plane component of the magnetization. In addition, the sum of the two diodes gives a measure of the reflectivity of the sample and is therefore used to normalize the Kerr signal.

The sample is mounted onto a piezostage that allows the scanning of the sample underneath the focus of the laser beam. This enables to scan up to 100 μm in each lateral dimension and 10 μm in out-of-plane (w) direction with a resolution in the nanometer range. The w-axis is usually only used to keep the focus plane of the laser constant, which will be detailed below. For distances in the range of millimeters, the piezostage is mounted on a mechanical uv-stage and the objective lens onto a w stage. By scanning with the piezostage, images of the Kerr signal and simultaneously the reflectivity are acquired. The first are the primary data investigated in Chapters $4 - 8$. The latter are used to localize differences in material, such as edges of microstructered magnetic films or the antenna. We therefore refer to this image as topography. These images are typically tens of micrometers in size and have around 10000 pixels.

As indicated by the sketch, there is a second, red beam path in the microscope originating from an LED. It passes the same components but is focused such that it creates a far field image of the sample. Blue and red beam paths are separated with the help of a dichroic mirror and the red image is recorded with a CCD camera. It is used as a reference

Figure 3.7: Sketch of the optical components of the TRMOKE setup. Starting from the top left, green depicts the pump laser, red shows the infrared pulses and blue the frequency doubled pulses. There is a second light source, a red LED, that shares the beam path with the blue light in purple regions.
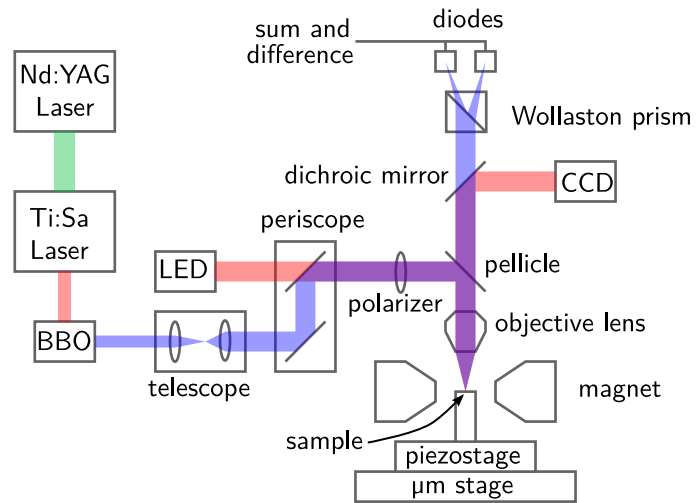
for focus and position of the sample. This is especially important as thermal drift can change the position of the piezostage relative to the laser beam on timescales of few hours. To prevent this, the image is fed to a PC and before a measurement scan, a reference image with the correct position of the focused laser is saved. In between measurements (that usually take approximately 1 h), the stage is actively adjusted such that the current image from the CCD is the same as the reference image. This procedure utilizes an image pattern recognition algorithm provided by the *Vision and motion* module in the LabView programming language.

The sample is located in between the pole shoes of a magnet. It provides external in-plane fields of up to $\mu_0 H_{\mathrm{ext}} = 250\,\mathrm{mT}$ and is rotatable. This allows to externally adjust the angle ϕ. Both magnitude and angle can be controlled by a computer.

3.3.3 Synchronization and Modulation

At the heart of the time resolution of the TRMOKE setup is the synchronization of laser pulse repetition rate with the high excitation frequency, which drives the magnetization precession. In particular, it is challenging to keep the phase between both as their frequencies differ widely (80 MHz vs. ≈ 8 GHz).

Figure 3.8 shows the components necessary to achieve this goal. A synchrolock accompanying the Mira 900 is used to actively stabilize the repetition frequency to exactly 80 MHz. A diode behind the output coupler provides a measure of the current repetition rate and a feedback loop adjusts the laser cavity via a piezotube mounted mirror. At present, the internal quartz of the synchrolock is the master clock of the setup. Its 10 MHz reference is fed to the high frequency generator, which is connected to the sample and in particular to the micro-structured spin wave antenna. In between, there is a PC-controlled phase shifter. Since the phase of the output of our frequency generator drifts with respect to the 10 MHz reference (on the order of minutes), we actively stabilize the relative phase
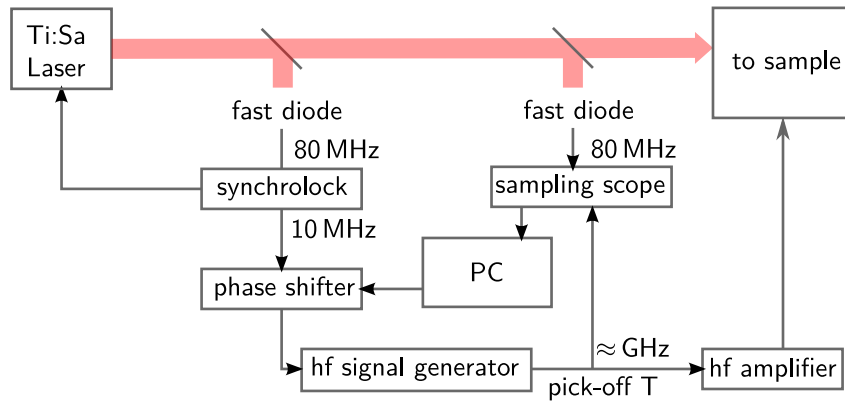
Figure 3.8: Phase stabilization circuitry of the TRMOKE setup. Red depicts the beam path originating from the laser. Black arrows represent electrical connections between the components.

between laser and frequency generator: An additional diode is used to trigger a high frequency sampling scope whose input is connected to the output of the signal generator. The resulting sine is fitted on the PC and its phase can be manually set and kept constant by continuously shifting the reference of the signal generator. Note, that the phase that is obtained from the sine fit cannot be identified as absolute phase of the microwave at the antenna as arbitrary phases can be introduced by all microwave components. However, it has been shown that these arbitrary phases can be regarded as constant in time. The active feedback loop of the phase extends its stability up to several days, thus allowing for long measurements. It also provides an estimate of the phase error that is usually considerably less than 10°.

In order to increase the signal-to-noise ratio of the setup, lock-in technique is used. In between signal generator and sample, a microwave chopper is introduced as shown in Fig. 3.9. The frequency of this on/off-modulation in the kHz regime is provided by a low frequency generator. Its reference, as well as the Kerr Signal — which is now modulated — is fed to a *Zurich instruments* HF2LI Lock-in. The X-channel of the lock-in gives a signal proportional to the out-of-plane component of the magnetization.

Instead of a microwave chopper, a mixer can be introduced into the circuit. When fed with a square modulation signal, this effectively shifts the phase of the magnetization by π. The resulting signals are depicted in Fig. 3.10 in a similar manner as in Fig. 3.9. Most importantly, the signal at the lock-in (sketched in Fig. 3.10 **c**) is twice as large as compared to an on/off modulation. For this reason, the technique was preferentially used in the experiments.

Next to an increased signal-to-noise ratio, both modulation techniques assure, that the signal only stems from dynamic contributions to the magnetization. This means that an out-of-plane tilt of the static magnetization (e.g. at sample edges or due to out-of-plane anisotropies) is not observed, which can be advantageous when investigating dynamics. Note that in these active modulation techniques, the transient of the magnetization oscil-
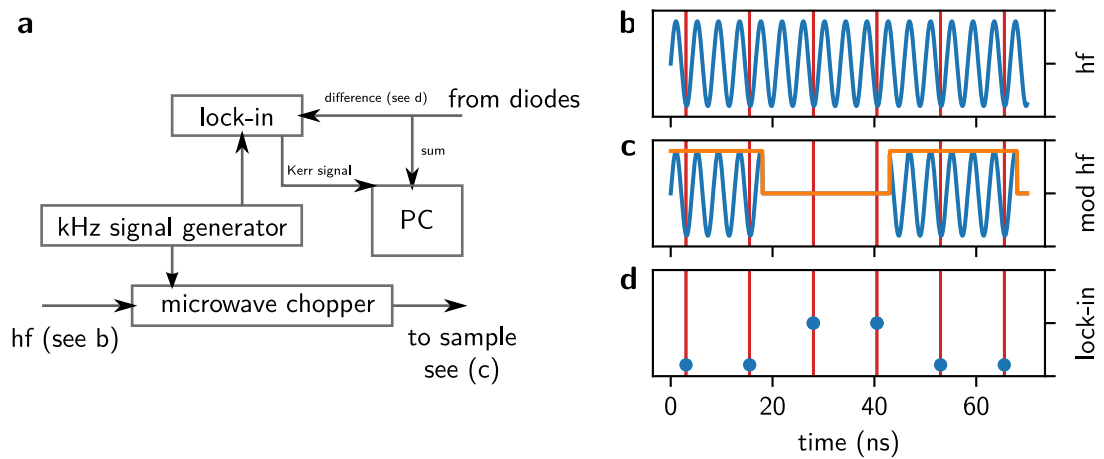
Figure 3.9: a Modulation circuitry of the TRMOKE setup if a microwave chopper is used. **b − d** show the signal after the hf generator, the signal that is fed to the sample, and the signal that is expected at the lock-in, respectively. Red vertical arrows are the laser pulses that are phase locked to the microwave excitation (blue lines). Blue dots show the current value of the magnetization when probed by a laser pulse. The time scales (except for the laser pulses) are not representative for a real measurement.

Figure 3.10: Signals as defined in Fig. 3.9 if a mixer instead of a microwave chopper is used.
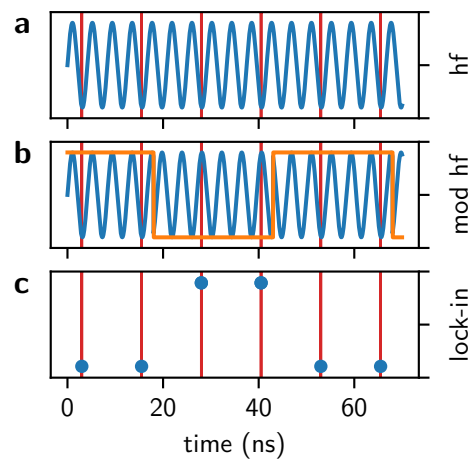
lation is ignored, which is a good approximation since this process is in the nanosecond range while the modulation is in the $100\,\mu s$ range.

4 Propagation Characteristics

This chapter aims at giving a first impression of spin wave propagation in thin films and is therefore a transition to the experiments in the following chapters. In Sec. 4.1, the numerical methods derived previously are applied to verify the thin film approximation used in the analytical dispersion relation. In addition, the modal profiles of zeroth and higher PSSWs are investigated numerically. In particular, the classically expected surface character of spin waves for $\phi \neq 0$ is examined. After this verification, in the following section first experimental results — recorded by TRMOKE — are shown. The analytical dispersion relation is used to explain the unique propagation characteristics of spin waves in thin films. In particular, the excitation of plane waves and caustics is discussed. The latter correspond to beams that form due to regions in iso-frequency curves with zero curvature [116, 117, 118].

In this chapter spin waves propagate in Py films with a nominal thickness of $L = 60\,\text{nm}$. Samples have been prepared by standard lithography and thin film deposition techniques as described in [113]. The values for Py on page 24 are used for both analytical and numerical calculations.

4.1 Applicability of the Thin Film Approximation and Surface Character of Spin Waves

As described in Section 2.6, the thin film approximation assumes a constant modal profile across the thickness of the film. The reason is exchange interaction that locks the magnetization along the w-coordinate. The length scale, where exchange is dominant, is defined by the exchange length l_{exc}, which is around $5\,\text{nm}$ in Py. In contrast to this length, the film thickness in our experiments is rather large ($60\,\text{nm}$), which raises questions about the applicability of the thin film approach for the dispersion relation. As described in Sec. 3.2.1, the dynamic matrix approach for full films is suitable to study the modal profile across the film thickness and is used here to verify the analytical dispersion relation. In order to do so, cases relevant in the experiments are discussed in the following.

A Py film of thickness $L = 60\,\text{nm}$ is discretized into $N = 100$ cells resulting in a cell size of $d_w = 0.6\,\text{nm}$. Since this is far below the exchange length, it allows for an accurate description even for higher order standing modes. No pinning is present at the boundaries. The dispersion relation of spin waves propagating at $\phi = 90°$ (i.e. DE modes) and $\phi = 30°$ are shown in Fig. 4.1 **a**. For both angles, two modes are visible, the zeroth propagating spin wave mode (close to the red lines) and the first PSSW. The latter are basically dispersionless and hardly affected by the direction of static magnetization. At the crossing points of the dispersion branches near $k_0 = 5\,\mu\text{m}^{-1}$, mode hybridization — and therefore avoided crossings — are observed. These are indications for interaction of
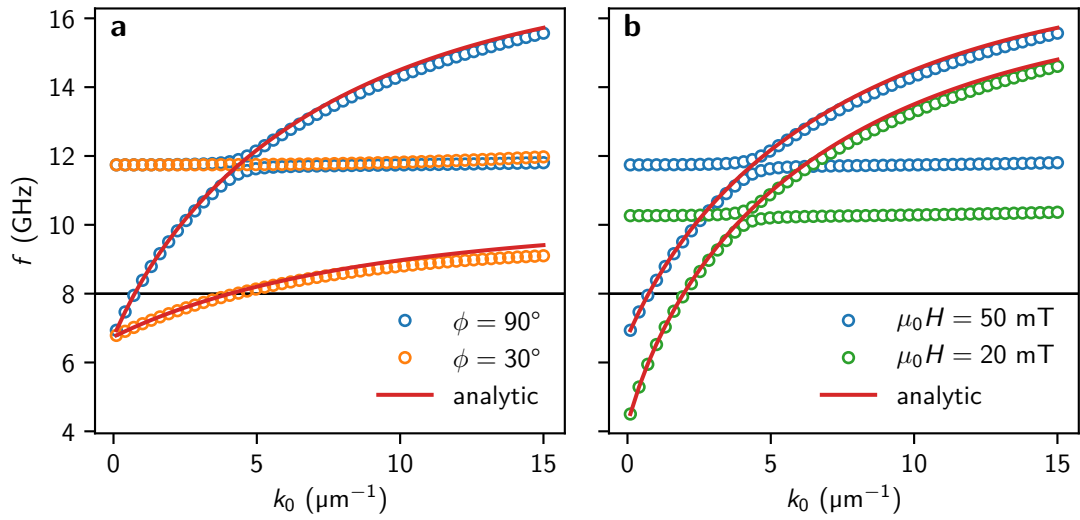
Figure 4.1: Dispersion relations for the two lowest PSSW modes with in-plane wave vector k_0, calculated by the dynamic matrix approach. **a** shows two different angles ϕ in a field of $\mu_0 H = 50\,\text{mT}$, while **b** shows two different fields at an angle of $\phi = 90°$. The blue dots represent the same data in both graphs.
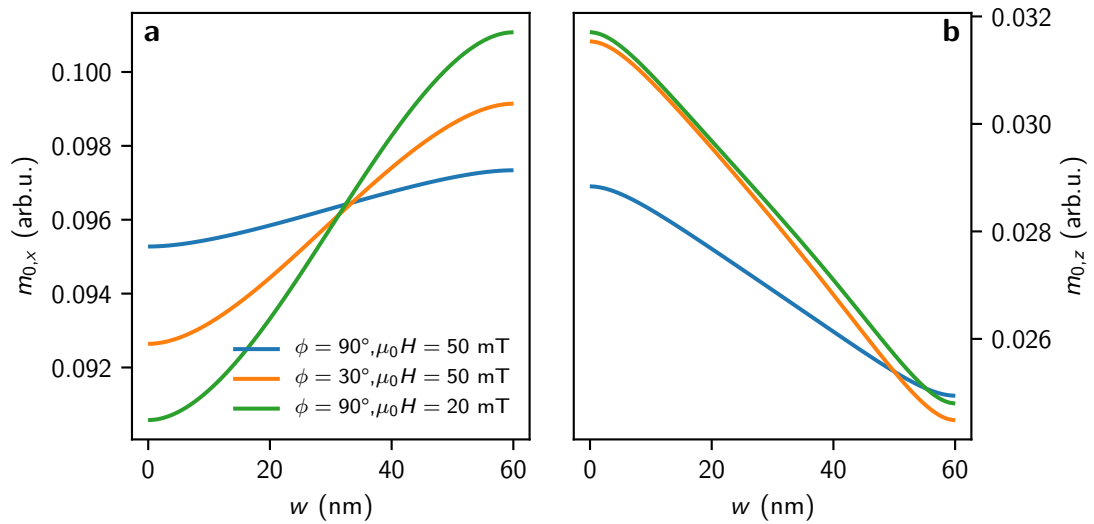
Figure 4.2: a In-plane and **b** out-of-plane dynamic magnetization component versus coordinate w, calculated by the full film dynamic matrix approach. Different fields H and angles ϕ between field and **k** are investigated as indicated by the legend. The modes correspond to the points at $f = 8\,\text{GHz}$ in Fig. 4.1.

the zeroth and first mode. The analytical thin film dispersion defined in Eq. (2.38) is plotted in red. It obviously does not account for higher order modes and therefore also fails near points of hybridization. In addition, for smaller angles between magnetization and $\mathbf{k}$, it deviates from the numerical points at comparatively small frequencies.

Figure 4.1 **b** compares two dispersion relations for different fields at the same angle $\phi = 90°$. The dispersion is shifted downwards with lower fields as is directly expected from the dispersion relation. Again, near points of hybridization, the analytical dispersion starts to deviate from numerical calculations. Experiments are usually conducted at 8 GHz, corresponding to the horizontal black line in both subplots. There, the analytical dispersion is less reliable for both smaller angles ϕ and smaller fields H. However, the deviation at 8 GHz never exceeds 1%, which makes the thin film approximation applicable within the experimental error.

Figure 4.2 shows the modal profiles for the different configurations discussed. They correspond to the points being closest to the 8 GHz line in Fig. 4.1. A stronger non-uniformity of modes across the thickness coordinate w can be made responsible for the deviations. It is also interesting to inspect the surface character of the profiles. In particular x and z-component, shown in **a** and **b**, respectively, have larger amplitudes on different sides of the film. This implies a change of ellipticity of the magnetization precession across the thickness of the stripe. In the classical DE picture, this is not expected. By contrast, the wave should exhibit an exponentially decaying profile with the same decay constant for both components of $\mathbf{m}$. The localization side is defined where the inward normal $\mathbf{n}$ verifies [56, 98]

$$\frac{\mathbf{k}}{k} = \mathbf{n} \times \frac{\mathbf{M}}{M} . \tag{4.1}$$

In the coordinate system discussed here, this is equivalent to the top side for $0 > \phi \geq -180°$ and the bottom side for $0 < \phi < 180°$. However, the modal profiles deviate from an exponential due to the exchange boundary conditions that are not considered in the DE approach. In addition, the localization condition Eq. (4.1) is only true for the out-of-plane component[1] cf. Fig. 4.2 **b**. However, the in-plane component $m_{0,x}$ and also the magnitude of precession m_0 is localized on the top side.

These "unexpected" modal profiles have been proposed and found for the pure DE geometry, $\phi = 90°$ [97, 98, 99]. In these references, the hybridization of zeroth and first PSSW is made responsible. Since for the cases of $\phi \neq 0°, 90°$, to our knowledge no studies have been published, this effect is qualitatively accessed for our case in Fig. 4.3. Modal profiles for different wave vector magnitudes k are shown for the three different cases discussed in Figures 4.1 and 4.2. They correspond to every second individual dot in Fig. 4.1 up to $5\,\mu m^{-1}$ for each lowest energy mode.

With increasing k, the profiles in **a** and **c** exhibit a sign change thus indicating their smooth transition towards the first standing mode. However, in **b**, the profiles hardly change and even in the upper k limit clear signs of hybridization are lacking. This is expected, since in the BV geometry, $\phi = 0°$, the interaction between modes of different symmetry should vanish [21]. There, the profiles are perfectly symmetric and antisym-

---

[1] We therefore expect this condition to be satisfied in our experiments, where we are only sensitive to the out-of-plane component.
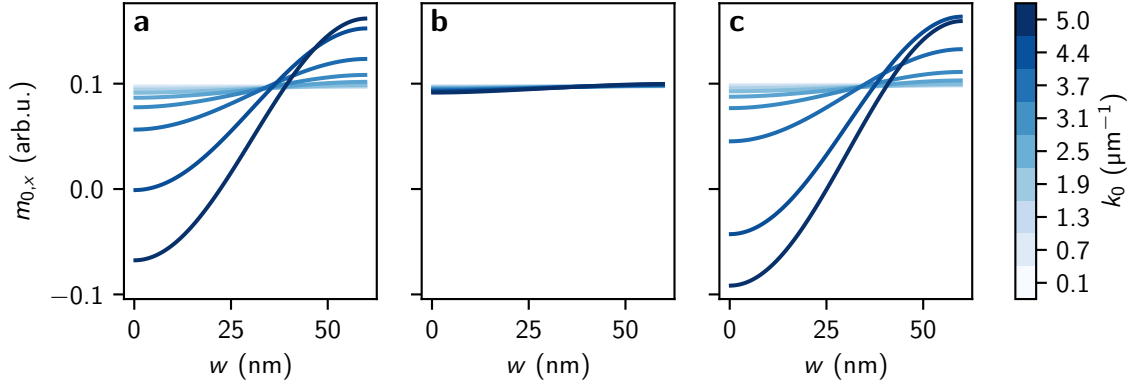
Figure 4.3: In-plane magnetization $m_{0,x}$ vs. thickness coordinate w of the lowest energy modes for different wave vector magnitudes k. These profiles are calculated by the full film dynamic matrix approach. **a**, **b**, and **c** discuss the three different cases $\mu_0 H = 50\,\text{mT}$ $\phi = 90°$, $\mu_0 H = 50\,\text{mT}$ $\phi = 30°$, and $\mu_0 H = 20\,\text{mT}$ $\phi = 90°$, respectively. These correspond to every second individual dot in Fig. 4.1.

metric. Based on this reasoning, it is astonishing that the mode with $\phi = 30°$ still has a stronger localization in Fig. 4.2. We suspect that the non-reciprocal components of dynamic fields, i.e. the dynamic demagnetization component n_{vw} in combination with the exchange boundary conditions are responsible for this behavior. These ingredients were found to dictate the hybridization between different dispersion branches [21, 97, 98].

Concluding this section, it is noted that analytical and numerical evaluations of the dispersion relation agree very well, especially for larger fields and angles around $\phi = 90°$. It is therefore reasonable to use the analytical dispersion relation in thin film approximation to extract magnetic parameters of a Py film. A correct understanding of the spin wave localization can be obtained by solving the relevant equations in dynamic matrix approach. With decreasing angle between propagation direction and static magnetization, the localization rises until it eventually vanishes for $\phi = 0$.

4.2 Plane Waves and Caustics

The anisotropic nature of the demagnetizing fields causes interesting features of spin wave propagation. Usually, these are assessed with the help of iso-frequency curves derived from the dispersion relation [68, 69]. In this subsection, the first experimental results are presented together with corresponding iso-frequency curves to give a first qualitative understanding of these features.

Figure 4.4 **a** shows an overview image of the propagation of a plane spin wave in a 60 nm thick Py film recorded by TRMOKE. The image was stitched from a series of 40 μm×40 μm images with a step size of 300 nm. On the right side, the contrast sharply vanishes because no further images where taken there. Note that the same color code is used for all following images and is therefore often omitted.

The wave is generated by a microwave antenna (depicted as light yellow rectangle), which defines the direction of the wave vector to be perpendicular (phase fronts parallel)
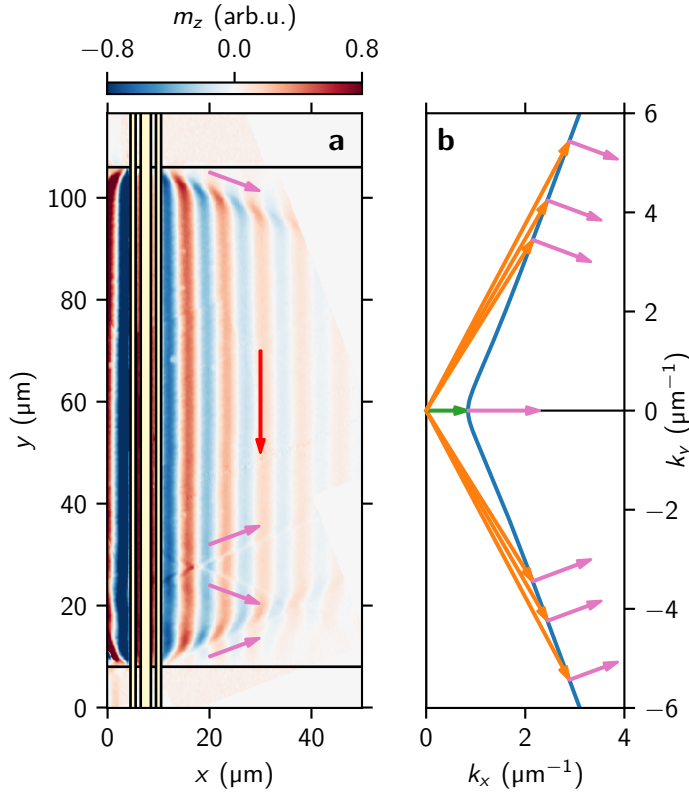
Figure 4.4: a Experimental data of plane wave propagation in a Py film of 60 nm thickness. The excitation frequency is 8 GHz and the external field (red arrow) is $\mu_0 H_{ext} = 48$ mT. Only the right side of the CPW (light yellow rectangle) is investigated. **b** Corresponding iso-frequency curve (blue) with the main **k** vector excited by the antenna in green. **k** with larger angles are shown in orange. In **a** and in **b**, the pink arrows are the directions of group velocities of caustics.

to it for most of the image. The external field is applied in the direction of the red arrow, which corresponds to the DE geometry. A wave differing to the first one only by its amplitude is also excited to the left of the antenna, and the excitation non-reciprocity is noticeable as discussed in Sec. 2.7. Notably, although of different origin, the excitation asymmetry favors the propagation direction defined in Eq. (4.1), where **n** denotes the inward normal for the side of the film, where the antenna is placed.

The black horizontal lines mark the edges of the Py film. There, the wave cannot be regarded as plane anymore and beam-like patterns with slightly higher intensity form. The latter mark the boundary of the plane wave (outer pink arrows). Similar textures can be found near $y = 28$ µm (inner pink arrows).

An iso-frequency curve of the Py film for the given external field and $k_x > 0$ is shown in subplot **b** as a blue line. The expected wave vector of the main wave (green arrow) can be found at the intersection of a line perpendicular to the antenna (along x-direction) and the iso-frequency curve. It corresponds to the case $\phi = 90°$. The group velocity and, therefore, the direction of energy flow is shown as a pink arrow which is parallel to the **k**-vector. For angles $\phi \neq 90°$, this is not necessarily the case as shown by the orange **k**-vectors and corresponding group velocities. In addition, in a wide range of angles, the iso-frequency curve has almost zero curvature and the group velocities are therefore pointing in the same direction. If a broad spectrum of waves is excited in this region in **k**-space, so called spin wave caustics are formed. They propagate in the form of beams with small divergence
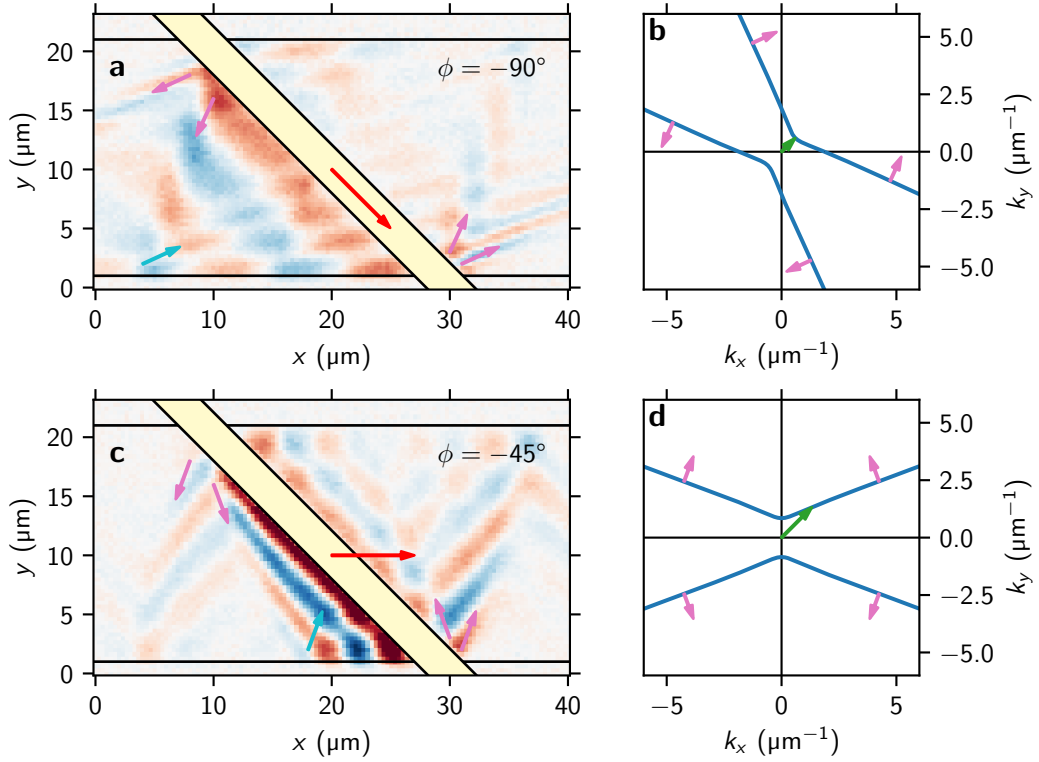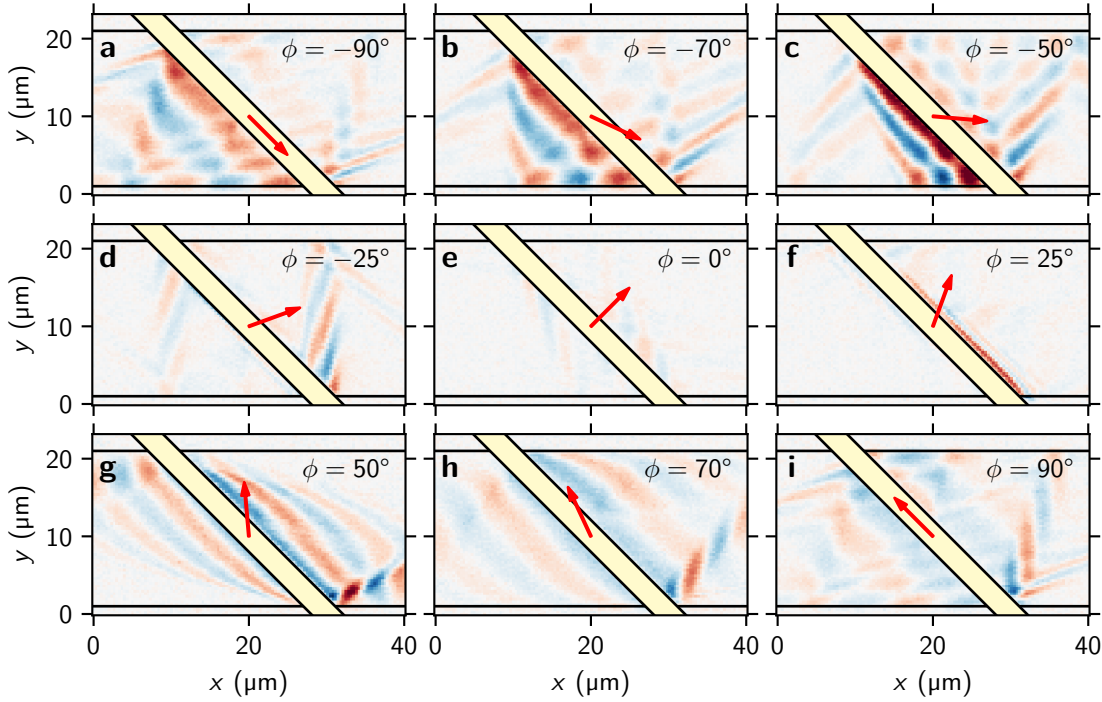
Figure 4.5: a and **c**: Experimental data of the interference pattern in a 20 µm wide Py stripe for $\mu_0 H_{ext} = 54\,\text{mT}$ and $\phi = -90°$ and $\phi = -45°$, respectively. **b** and **d**: Corresponding iso-frequency curves. The color code is the same as in Fig. 4.4. In addition, teal arrows show the direction of reflected caustics for the bottom left of the antenna.

and their direction of propagation is defined by the group velocity.

The aforementioned regions of higher intensity in the experimental data can now be identified as such caustic beams. They form due to the broad excitation spectrum of the antenna (along x-direction), as well as of the edge (along y-direction) as shortly mentioned at the end of Sec. 2.7. The beam diameter corresponds to the projection of the lateral dimension, where a finite excitation field of the antenna exists.

The smaller beams (inner pink arrows) are caused by a structural defect in the sample (observable in the reflection image, not shown), which can also act as an emitter of spin waves due to a local change of the dynamic fields that provides a broad excitation spectrum in all directions. Therefore, the beam diameter is given by the dimension of this defect and is of the order of few hundred nanometers. In Ref. [119], point defects as emitter of caustics have been investigated in more detail.

Since the direction of the main axis of the iso-frequency curve depends on the direction of the static magnetization, it can be easily influenced by the external field. In addition, if the antenna is structured at an angle to the Py film, one can suppress (or force) the creation of caustics near the edge. Figure 4.5 **a** and **c** show experimental data for a 20 µm

Figure 4.6: Experimental data for the angular dependence of the interference pattern in a 20 µm wide Py stripe for $\mu_0 H_{ext} = 54\,\text{mT}$. The respective angles of the external field ϕ are indicated by the red arrows and the numbers in the top right. They are given with respect to the main plane wave excited by the antenna and traveling towards the bottom left.

wide Py stripe, while **b** and **d** depict the respective iso-frequency curves. The antenna is at an angle of 45° to the Py edge.

In **a**, the main wave is again excited in the DE geometry, i.e. the static field is parallel to the antenna, perpendicular to the main **k**-vector ($|\phi| = 90°$). Four main caustics can be identified (pink arrows) and their directions can be understood by the four caustic directions of the iso-frequency curve in subplot **b**. For the interference pattern on the left side of the antenna, also a secondary, reflected caustic (teal arrow) is highlighted. Since the caustics mark the border of the plane wave, the triangle built by the edge of the film, the teal arrow and the antenna give the region where the reflection interference is due to plane waves. The quantitative investigation of this interference pattern of plane waves is one of the main topics in the following experimental chapters.

In **c**, the external field is applied parallel to the stripe and therefore $|\phi| = 45°$. The **k**-vector of the main wave is larger, which can be understood by the rotation of the iso-frequency curve with respect to the antenna (subplot **d**). Still, there is a region where phase fronts are parallel to the antenna and the wave can be regarded as plane. Note that wave reflected from the top side of the Py film propagates back towards the antenna and can therefore potentially influence the interference pattern in the aforementioned triangle on the bottom. In order to prevent this, the film width has to be large compared to the

attenuation length.

Fig. 4.6 gives an overview of the angular dependence. As can be seen from subplot **a** and **i**, upon reversal of the external field only the amplitude (and phase) of the interference pattern on either side is influenced, but the pattern itself remains unchanged. It is therefore enough to consider the interval from $-90°$ to $90°$ for the following discussion. On a side note, the amplitude in **a** is considerably more asymmetric than in **i**. Neither excitation non-reciprocity nor the classical modal profile non-reciprocity can explain this behavior as both depend on the direction of **M**. One candidate could be a stronger pinning of the magnetization on the top of the film, that causes an additional non-reciprocity that depends on the sample geometry and not on the magnetization.

For angles between $-90°$ and $-25°$ (**a** – **d**) the "plane wave triangle" gets smaller. At $\phi = -25°$, plane waves are hardly excited anymore, since the angle of the caustics approach the angle of the antenna and, in addition, the excitation efficiency of the antenna for the particular **k**-vector dictated by the dispersion relation vanishes. Consequently, in BV geometry, $\phi = 0$, the caustics are only faintly visible and there is no plane wave. With increasing positive angle, there exist plane waves that have the same wave vector as their negative counterparts (apart from a minor misalignment of the external field with respect to the antenna), since the dispersion is symmetric around the axis of $\phi = 0$. More importantly, in sharp contrast to the negative angles, there is no reflection of the plane wave from the bottom edge at $y = 1\,\mu\text{m}$. This is due to the fact that the group velocities point in different directions as can be directly seen from the caustics or could be quantitatively found from the iso-frequency curves.

In conclusion, it is noteworthy that a wide range of angles exists outside of the interval $-25° < \phi < 25°$ of the external field which allows for the excitation of plane waves. On which side of the film a plane wave reflection is observable, depends on a combination of the angle between antenna and edge — so in general of the patterning of the sample — and the direction of the external field.
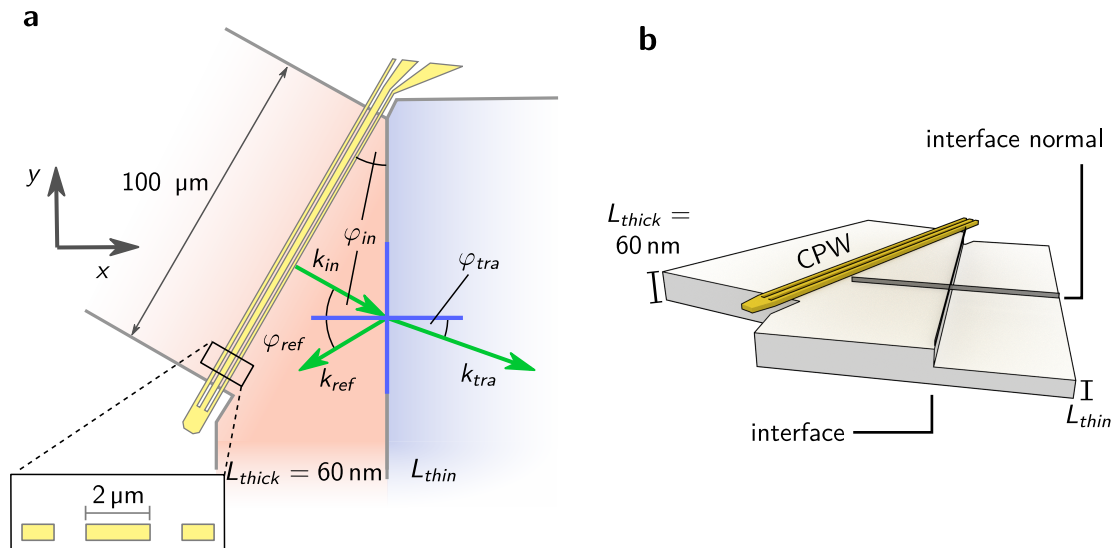
Part II

Experimental Results

5 Sample Design, Coordinate System, and Field Direction

The reflection and refraction of spin waves at thickness steps and edges will be quantitatively investigated in Chapters 6 – 8. A brief introduction to the sample design and the coordinate system used there is given in this chapter.

As has been shown in the previous chapter, different field directions have great influence on how (and if) a wave will propagate towards an interface and if reflection and refraction is observed at all. At the end of this chapter, we will therefore qualitatively discuss the influences of the field direction on a sample with a large angle between antenna and interface.

Fig 5.1 **a** shows a sketch of the general layout. For convenience, we will use a coordinate system, where x and y denote the image axis and z is pointing out-of-plane. The y-direction is always aligned with the thickness step, i.e. the interface of the refraction. To avoid confusion with the magnetization coordinate system, the direction of the external


Figure 5.1: a Sketch of the sample geometry. Spin waves with wave vector $\mathbf{k}_{in}$ impinge on the interface at φ_{in}, the latter determined by the orientation of the patterned antenna whose dimensions are shown in the inset. In this particular case, it holds $\varphi_{in} = 30°$. The blue cross marks the interface and interface normal between the thick (shaded red) and thin (shaded blue) Permalloy films. Note that there are also samples where $L_{thin} = 0$, i.e. there is only reflection taking place. **b** 3D sketch of the same sample, the z-axis is not drawn to scale. The thickness step acts as an interface for the refraction process.

field, i.e the static magnetization will always be marked in experimental data by a red arrow. For simplicity, wave vector components will as well be denoted in this reference frame.

The sample fabrication was done at the University of Kyoto in the group of Prof. Dr. Teruo Ono. Firstly, using rf magnetron sputtering, a Py film is deposited with thickness L_{thin} on an oxidized Si substrate. Secondly, a region on top (shaded red in Fig. 5.1 **a**) is structured by electron beam lithography, Py sputtering and lift-off process such that this part has $L_{\text{thick}} = 60$ nm. Therefore, an abrupt change of Py thickness is reached and this thickness step works as a boundary of different media in the experiments, see **b**. Thirdly, the final sample dimensions (red and blue parts in **a**) are patterned by electron beam lithography. With Ar^+ milling, the surrounding Py is removed. Afterwards, a multilayer of $SiO_2(63\,\text{nm})/Ti(5\,\text{nm})/Au(100\,\text{nm})$ is sputtered. Finally, a CPW is fabricated from this last Au layer (shown yellow) on top of the thick Py film. It consists of a 2-µm-width signal line and two 1-µm-width ground lines which are separated from the signal line by 1 µm. Such an antenna was studied in Sec. 2.7. Again, electron beam lithography and Ar^+ milling is used for this structuring. The SiO_2 layer remains and isolates the antenna from the conducting Py. It also protects the magnetic film from oxidation.

The antenna will generate a spin wave to either side, where the wave vector to the right is denoted $\mathbf{k}_{\text{in}}$. Note that in all following experiments, spin waves are excited in a film with $L_{\text{thick}} = 60\,\text{nm}$. Here, the wave traveling to the left of the antenna is not of importance. At the interface, we expect a reflected and a transmitted (refracted) wave with wave vectors $\mathbf{k}_{\text{ref}}$ and $\mathbf{k}_{\text{tra}}$, respectively. Since we want to study the angular dependence of refraction processes for spin waves, an angle φ is introduced to account for the propagation direction of the spin waves with respect to the interface normal. As the angle φ_{in} can only be influenced by different sample structuring, we will use $\varphi_{\text{in}} = \varphi$ to denote different samples. In addition, we distinguish them with the thickness L_{thin}. Note that there are also samples with $L_{\text{thin}} = 0$ such that only reflection is observable. With one structuring process, a chip that features samples with one thickness L_{thin} but many (typically four) angles φ is produced. In the following experiments, a total of six samples with incident angles φ_{in} from 10° to 60° is studied. The general structure of these does not differ from the one shown in Fig. 5.1, i.e. as φ_{in} increases, the Py film to the left of the antenna is still structured perpendicularly to it. Obviously, the distance from the bottom part of the antenna to the interface is thereby increased. The general dimensions are large enough (100 µm) with respect to the attenuation lengths (≈ 10 µm) such that secondary reflections or caustics do not disturb the plane wave interference pattern.

In order to obtain reflection and refraction, one has to make sure that there are components of the group velocity pointing towards the interface. As shown in the previous section, this can be achieved with the correct combination of external field angle ϕ and incident angle φ. This is analyzed qualitatively in Fig. 5.2, where the "extreme" case of $\varphi_{\text{in}} = 60°$ is depicted. In this sample, $L_{\text{thin}} = 0$ and there is no second medium where refraction can take place. The interface is marked by the vertical gray line. **a** shows data, where the external field (red arrow) is aligned at an angle $\phi = -80°$ with respect to $\mathbf{k}_{\text{in}}$. The wave does not hit the interface since the group velocity is almost parallel to it. In DE geometry, see subplot **b**, there already appear ripples on top of the main wave that exhibit a much larger wave vector magnitude than k_{in}. These can be identified as the reflected
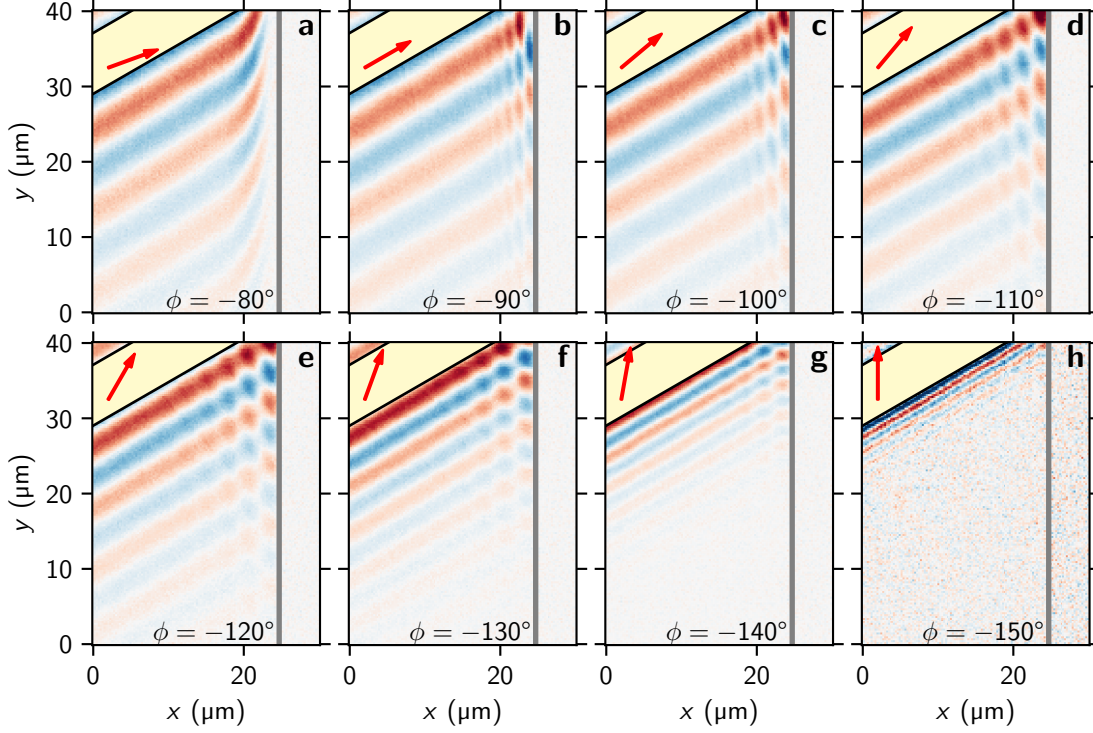
Figure 5.2: Experimental data for the angular field dependence of a sample with $\varphi_{\text{in}} = 60°$. The external field is $\mu_0 H_{\text{ext}} = 50\,\text{mT}$. The angle of the external field is indicated by the red arrow, ϕ denotes the angle between external field and main **k**-vector of the antenna. The color code in **h** is magnified by a factor of 5.

wave and, with increasing absolute angle, see subplots $\mathbf{c} - \mathbf{h}$, their wave vector magnitude k_{ref} decreases in comparison to k_{in}. The latter is increasing, due to a tilt away from DE geometry that exhibits the smallest wave vector of in-plane spin waves. Consequently, the amplitude drops because the excitation efficiency of the antenna decreases for larger k_{in}. In addition, L_{att} is smaller for these angles. Still, for an angle up to $\phi = -150°$ (parallel to the interface) some components of the group velocity are directed towards the interface, although the reflected wave can not be resolved without raising the pixel density. The quantitative relation between ϕ, φ, and k for all waves is the subject of the following chapters.

In $\mathbf{a} - \mathbf{c}$, near the edge of the film, the phase fronts of the main wave are not straight lines but slightly curved towards the top. This feature is the so called bending of spin waves [33], which originates from static dipolar interactions. Near the edge of the film, the internal field is decreased and the magnetization tilts away from the external field to avoid the generation of surface charges. Thus, the **k**-vector adjusts to this new dispersion, such that the phase fronts are not constant anymore. This behavior is reminiscent of light propagation in media with graded index of refraction and therefore linked to the mirage effect. It is quantitatively investigated in Sec. 6.3. When the external field is applied along the edge or interface (subplot **h**), these static effects are suppressed and a plane

wave propagation is expected.

In conclusion, for large incident angles, reflection is observed for the range of angles from DE geometry (**b**) to the case where the field orientation is pointing parallel to the edge (**h**). These cases will be quantitatively discussed in Chapter 6 and Chapters 7, 8, respectively. Due to large sample dimensions, the caustics do not disturb the interference pattern in this case and the plane wave model is applicable, except in regions close to the edge where bending is present.

6 Snell's Law for Spin Waves

Snell's law describes the refraction of waves at the transition between two media with different indices of refraction. The prototypical example is a light beam that gets refracted at the transition through a water or glass surface. The dispersion relation of light is in general isotropic and thus the relation between the incident and refracted angles is solely determined by the ratio of the refractive indices. In contrast, for spin waves we have shown in the previous chapters that the dispersion relation is inherently anisotropic in the dipolar regime and thus deviations from Snell's law in optics are expected.

In Refs. [120, 121, 122, 123], Snell's law has been investigated for exchange dominated spin waves, where dynamic dipolar interactions are negligible and the iso-frequency curves are circular or elliptic. Refs. [120, 121] consider two unbounded media with arbitrary parameters. In Ref. [122], the two media represent regions where the equilibrium position of $\mathbf{M}$ differs due to anisotropies and Ref. [123] considers an interface between a YIG and a Py film. In addition, there exist experimental works that either focus on reflection [124] or refraction [125, 126], but none of these consider both in a single experiment.

Thickness steps have been investigated experimentally [125, 127, 128] and numerically [129]. In Refs. [127, 129], their potential use as wavelength converters is mentioned, but a detailed analysis of the refraction and reflection process is lacking.

In the experiments presented in this chapter, we use a thickness step from $L_{\mathrm{thick}} = 60\,\mathrm{nm}$ to $L_{\mathrm{thin}} = 30\,\mathrm{nm}$ to realize the transition between two magnetic media with different dispersion relations for propagating spin waves. As can be seen in Fig. 6.1, after the transition
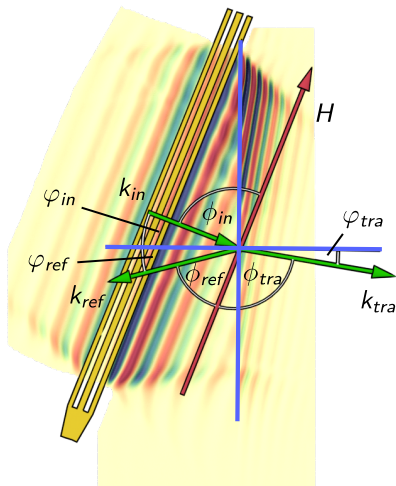
Figure 6.1: Overview of the experiment with exemplary data acquired by TRMOKE on a sample with $\varphi = 20°$. The green arrows show the wave vectors $\mathbf{k}_{\mathrm{in}}$, $\mathbf{k}_{\mathrm{tra}}$, and $\mathbf{k}_{\mathrm{ref}}$ relevant for the analysis. φ_{in}, φ_{tra}, and φ_{ref} denote the angles of the wave vectors with respect to the interface normal, while ϕ_{in}, ϕ_{tra}, and ϕ_{ref} denote the angles with respect to the external field.

at the interface (blue vertical line) both wave vector and angle change considerably. The angle and **k**-vector definitions are overlaid on the experimental data. Parts of the present chapter have been published in Ref. [23] and contain the first experimental results on the angular dependence of reflected and refracted waves in the dipolar regime, by measuring samples with different φ. The external field is always applied such that the incoming wave propagates in DE geometry. The excitation frequency is set to $f = 8\,\mathrm{GHz}$. A spin wave lens based on the refraction laws at a thickness step has meanwhile been published [130].

6.1 Quantitative Assessment of Wave and Sample Characteristics

So far, all experimental data has been only qualitatively discussed and dispersion relations were plotted with standard material parameters of Py. Although this has been shown to make many features accessible, a complementary quantitative discussion is mandatory.

To access spin waves characteristics, the data is fitted in 2D. The model function is defined as a single plane wave in the xy-plane as

$$f(x,y) = A \sin(k \cos(\beta)\, x + k \sin(\beta)\, y + p)\, \mathrm{e}^{-\frac{\cos(\beta)\, x}{L_{\mathrm{att}}} - \frac{\sin(\beta)\, y}{L_{\mathrm{att}}}} \qquad (6.1)$$

in regions where only one wave is expected. Here, the independent parameters that are fitted are the amplitude A, the phase p, the wave vector magnitude k, the attenuation length L_{att}, and an angle of propagation β defined with respect to the image axis. In regions where more than one wave is propagating — typically the incoming and reflected wave — a superposition of two functions $f(x,y)$ is used, yielding twice as many fitting parameters. A subset of data of a full image is obtained by truncating the data to that contained in a predefined polygon [131]. Here and henceforth this polygon represents the area where a wave is fitted and is marked with a white box in the images. This subset of data is then used to minimize the residual to the model function with respect to the independent parameters [132].

Figure 6.2 shows data ($\mathbf{a} - \mathbf{c}$) and corresponding fits ($\mathbf{d} - \mathbf{f}$) for a sample with $\varphi_{\mathrm{in}} = 20°$ and the external field applied in DE geometry, $\phi_{\mathrm{in}} = -90°$, for three different field strengths H. The position of the interface, as determined from topography data, is marked with a gray vertical line.

The parameters determined from such a field dependence can be used to further investigate the sample with the help of the analytical dispersion relation Eq. (2.38). Figure 6.3 $\mathbf{a}$ shows k and $\mathbf{b}$ shows β versus the field H. Within the error, β does not depend on the external field, while k shows an almost linear dependence. It is therefore possible to calculate ϕ directly from the mean of β. Then, the representation $k(H)$, Eq. (6.3), defined in the next section, can be straightforwardly used[1] to obtain the parameters M_{S} and L for all three waves. Roughly speaking, M_{S} determines the slope, while L determines the axis intersection.

This fit is shown in the graph and the parameters from the different fits are presented in $\mathbf{c}$. The quantity L_{thick} is the mean value obtained from both incoming and reflected wave

---

[1]Alternatively, the more accurate dispersion relation Eq. (2.38) can be used to fit the data implicitly.
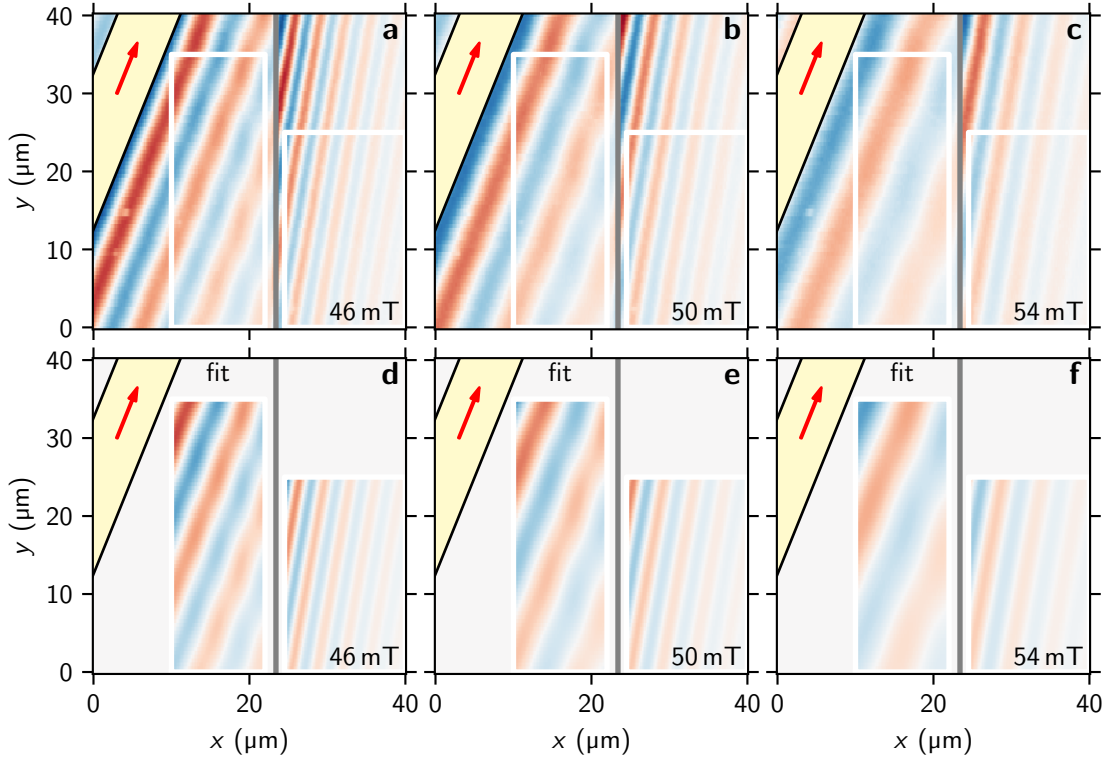
Figure 6.2: **a – c** Experimental data for different external field strengths $\mu_0 H_{\text{ext}}$ indicated in the figures for a sample with $\varphi_{\text{in}} = 20°$ and $L_{\text{thin}} = 30\,\text{nm}$. **d – f** Corresponding fits determined as described in the main text. The white rectangle to the left of the edge (gray vertical line) is fitted with two waves, while the rectangle to the right (thin part) is fitted with one wave. The direction of the external field is indicated by the red arrow. The light yellow rectangle marks the position of the antenna.

and M_{S} is the mean value from all three waves. The individual parameters agree within the error. Note that we fixed the gyromagnetic ratio to the standard value $\gamma = 185\,\text{GHz}\,\text{T}^{-1}$, because an independent access to both γ and M_{S} is not possible in this wave vector regime. Notably, M_{S} agrees well with the expected value for Py and the thicknesses are within 10% error of the nominal values.

6.2 Analytical Formulation

To predict refraction and reflection angles, we have to incorporate the anisotropic dispersion relation for spin waves in thin films into Snell's law. At first, we consider the case of a plane dipolar spin wave impinging on an arbitrary interface between two isotropic magnetic media. The continuity of the tangential component of the wave vector **k** of any wave, when experiencing reflection or when being transmitted to a different medium, can
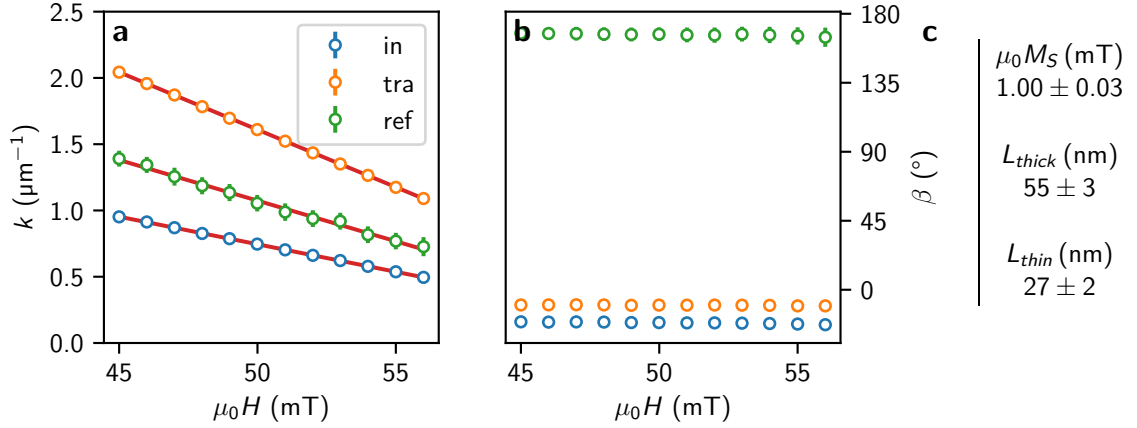
Figure 6.3: Summary of the field dependence on the sample with $\varphi_{in} = 20°$. **a** shows the wave vector amplitude k and **b** the angle of propagation with respect to the image axis β. The data points are obtained from fits as shown in Fig. 6.2. *in*, *tra*, and *ref* denote the incoming, transmitted, and reflected wave, respectively. **c** summarizes the structural parameters of Py as determined by a fit to the dispersion relation.

be regarded as Snell's law, namely

$$\sin(\varphi_{in}) = \frac{k_{ref,tra}}{k_{in}} \sin(\varphi_{ref,tra}) . \tag{6.2}$$

In optics, this reduces to the well known Snell's law for refracted waves, where $k_{ref,tra}$ can be substituted by the respective refractive indices due to isotropic and linear dispersion relations in most materials. For the same reasons, it simply follows $\varphi_{in} = \varphi_{tra}$ for a reflected wave since it remains in the same medium. By contrast, the wave vector of spin waves in thin films depends on the angle ϕ between the propagation direction with respect to the direction of the externally applied field $\mathbf{H}_{ext}$. This has been extensively discussed and can be quantitatively evaluated with the dispersion relation in thin film approximation, Eq. (2.38). Since the waves discussed experimentally verify $kL \ll 1$ [2] and exchange can be neglected, it can be rewritten as $k(\phi, H)$ and reads

$$k = \frac{\left(-\sqrt{((H + M_S)\sin^2(\phi) + H)^2 - \left(2\sin(\phi)\frac{\omega}{\mu_0\gamma} \right)^2} + (H + M_S)\sin^2(\phi) - H \right)}{L\, M_S \cdot \sin^2(\phi)} . \tag{6.3}$$

This expression for the wave vector magnitude can be inserted into Eq. (6.2) to obtain Snell's law for spin waves.

In this chapter, the external field is always aligned parallel to the CPW. Therefore, DE spin waves, $\phi = -90°$, get excited by the antenna. As has been shown in Sec. 2.6, they exhibit the largest attenuation length of all modes, which favors imaging. It remains to

---

[2]The difference between Eqs. (6.3) and (2.38) is below 10% at a wave vector magnitude of $k = 6\,\mu m^{-1}$ — the largest wave vector investigated.
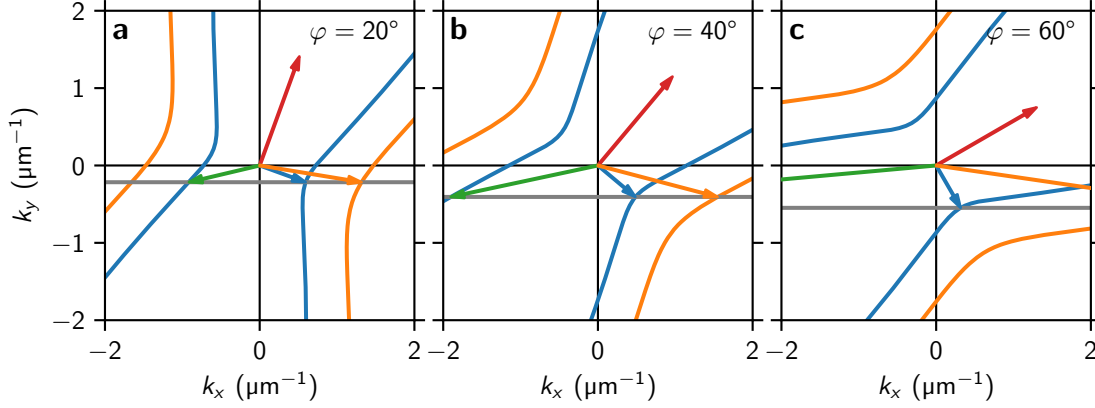
Figure 6.4: Iso-frequency curves for the refraction of DE spin waves (blue arrow) at an interface between a Py film of $L_{thick} = 60\,$nm (blue curve) to a film of $L_{thin} = 30\,$nm (orange curve). **a** – **c** show three different samples with $\varphi_{in} = 20°$, $40°$, and $60°$, respectively. The interface is directed along y. The field direction is shown as red arrow, refracted and reflected wave are shown as orange and green arrows, respectively.

identify the magnetic angle ϕ with the angle to the interface normal φ as $\phi_{tra} = (90° + \varphi_{tra} - \varphi_{in})$, see Fig. 6.1. Besides the known material and experimental parameters, the resulting implicit equation only depends on φ_{tra} and can therefore be used to predict refraction angles for spin waves for a given φ_{in}. Similarly, the angle of reflection can be determined by identifying $\phi_{ref} = 90° - \varphi_{ref} - \varphi_{in}$. Feeding the calculated angles back into Eq. (6.3) allows calculating the wave vector amplitudes. The formalism is not limited to experiments where different media are modeled with a different thickness of the film; it can also be used for interfaces consisting of different magnetic materials.

The above formalism can be illustrated with the use of iso-frequency curves defined by Eq. (6.3) and is depicted in Fig. 6.4 for thick (blue) and thin (orange) Py films. The values to calculate them are taken from the previous section. Each subplot shows a different sample, i.e. different φ. The incoming wave is just the DE wave in the thick film (blue arrow). Snell's law, Eq. (6.2), demands the continuity of the tangential component of the wave vector k_y. Transmitted and reflected wave vectors can therefore be found by the intersection of the gray line (that visualizes this component) with the respective iso-frequency curve [68]: blue for reflection and orange for transmission. By comparing **a** – **c**, one expects a non-linear increase of k_{tra} and k_{ref} with increasing φ (and constant k_{in}). One should note, that the angular dependence of the refracted wave depends crucially on the orientation of the external magnetic field, while its magnitude is negligible. By contrast, the wave vector amplitude is influenced substantially by the magnitude of the external field. This has already been experimentally observed in the previous section.

In the trivial case of spin waves impinging at normal incidence onto the thickness step, i.e. $\phi = 90°$, $\varphi = 0°$ for all waves, it is straightforward to define an angle-independent
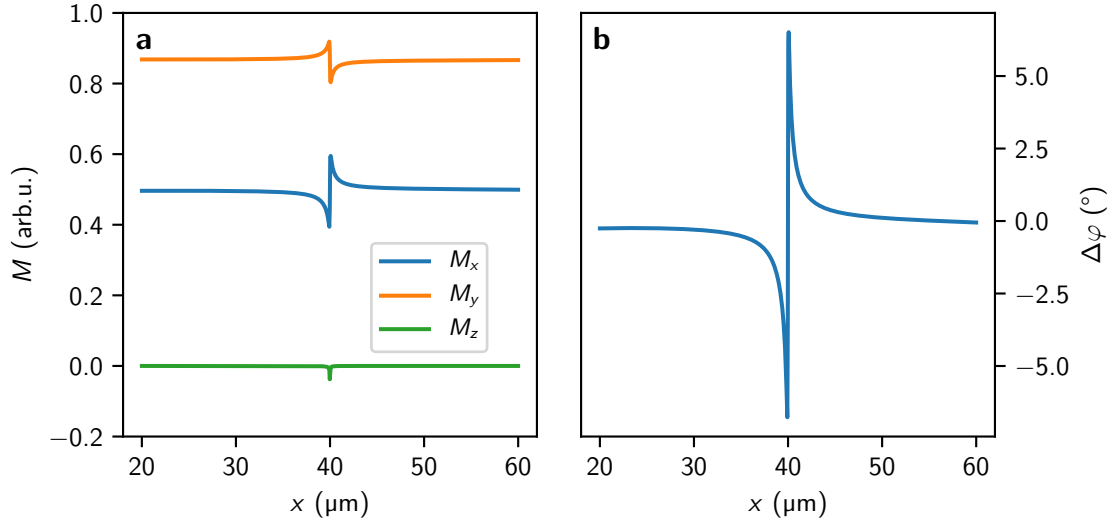
Figure 6.5: a Simulated magnetization profile along x-direction (perpendicular to the interface) for a sample with $\varphi = 30°$. This corresponds to an angle of the external field of 60° with respect to the x-axis. Its magnitude amounts to $\mu_0 H_{\text{ext}} = 54$ mT. **b** Corresponding in-plane deviation of the direction of the magnetization from the direction of the external field.

relative refractive index: since $k \propto \frac{1}{L}$, the expression $\frac{k_{\text{tra}}}{k_{\text{in}}}$ in Eq. (6.2) reduces to $\frac{L_{\text{thick}}}{L_{\text{thin}}} = 2$ and likewise to respective ratios in Chapter 7. This relative refractive index is later used when the experiments are compared to Snell's law in optics.

6.3 Bending of Spin Waves

In Chapter. 5, we have shortly touched on the topic of bending near the interface due to static dipolar effects. It is obvious that the inconstant wave fronts do not allow to use the plane wave fitting procedure described in Sec. 6.1.

To quantify the influence of the dipolar effects arising at the thickness step, we use mumax3 described in Sec. 3.1. The static magnetization is simulated on a grid of $16384 \times 16 \times 16$ cells and dimensions of $80000\,\text{nm} \times 80\,\text{nm} \times 60\,\text{nm}$ with periodic boundaries along the y-direction assuming a standard xyz-coordinate system. The step is located at $x = 40\,\mu\text{m}$ and is eight cells (30 nm) high. An external field of 54 mT is applied and the energy minimum is found via the built-in `relax()` function. After saving the magnetization and the effective field, the field is rotated and the procedure starts again. This is performed for a range of angles between $\varphi = 5°$ and 70°. From the magnetization, we calculate the deviation of the in-plane angle from the direction of the external field by $\Delta\varphi = 90° - \varphi - \arctan\left(\frac{M_y}{M_x}\right)$. Magnetization profile and deviation from the external field direction $\Delta\varphi$ are depicted in Fig. 6.5 for $\varphi = 30°$. One can observe a tilt of the magnetization near the edge, such that it is pointing more along the direction of the edge for the thick film, while in the thin film the component perpendicular to the edge becomes larger. Both
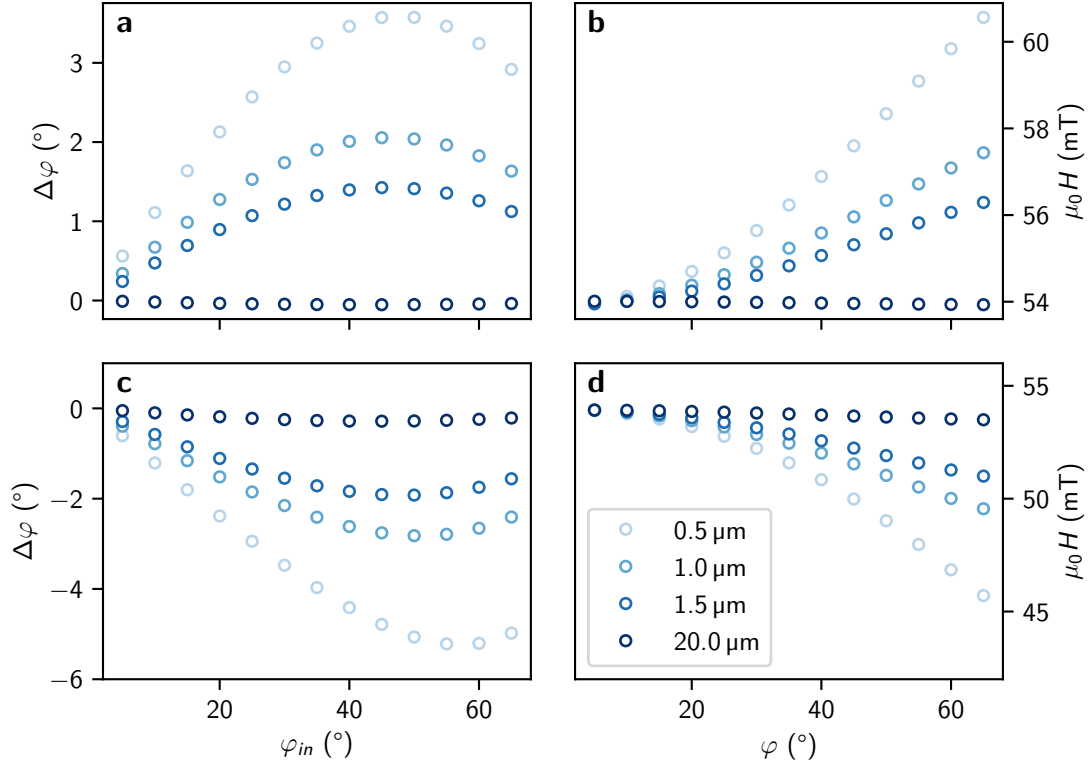
Figure 6.6: a and **c**: Simulation results for the angular deviation evaluated at different distances from the interface, for thin and thick part, respectively. **b** and **d**: Results for the effective field at different distances from the interface, for thin and thick part, respectively. All simulations where performed at $\mu_0 H_{ext} = 54$ mT.

effects can be understood by the charge avoidance at the thickness step.

In addition to this tilt of magnetization, the effective field is also influenced by the charge avoidance. In the thick film, it reduces the effective field due to its demagnetizing nature, while in the thin part, it enhances the effective field due to the stray field of the step. Both tilt and field contributions affect the dispersion relation and therefore the propagation of spin waves. Their influence is shown for different angles φ in Fig. 6.6. Here, subplot **a** and **b** show the thin film, while **c** and **d** are plotted for the thick film. As can be seen, the effects are stronger closer to the interface and amount to almost $\mu_0 \Delta H = 10$ mT and $\Delta \varphi = 5°$. When compared to the experimental results in the previous section, these deviations are certainly strong enough to change the dispersion relation near the interface.

We use these results to determine the change in k according to the procedure in Ref. [34]. As a first step, we calculate the wave vector magnitude k_{in} in the homogeneous region $x_{eval} = 15$ μm away from the interface by using the dispersion relation Eq. (2.38). The components are determined to $k_y = -k_{in} \sin(\varphi)$ and $k_{x,0} = k_{in} \cdot \cos(\varphi_{in})$.

According to Snell's law, k_y (the component along the interface) should be fixed in the entire sample. We evaluate the iso-frequency curves of the dispersion relation on a grid
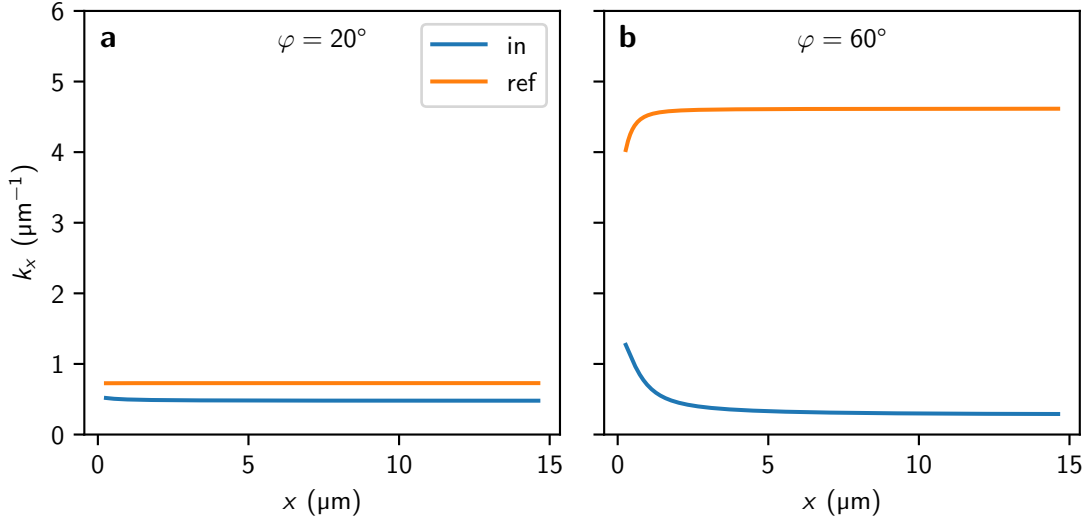
Figure 6.7: a and **b**: Wave vector component k_x versus distance from the interface for an external field angle of 20° and 60°, respectively. The latter corresponds to the results for the largest incident angle studied experimentally. Here, the effect of spin wave bending is the largest.

with cell size $d_x = 25\,\mathrm{nm}$ along the x-direction from x_{eval} to the interface and take into account the changing magnetization direction and the effective magnetic field. From these calculations we obtain different values of k_x for every grid point. We repeat the same procedure for the reflected wave. The results are presented in Fig. 6.7 for two different angles. In case of $\varphi = 20°$, the wave is hardly affected by the bending. By contrast, for large incident angles and, in particular, for $\varphi = 60°$, the bending can be strong near the interface. It is therefore mandatory to evaluate points sufficiently far away from the interface when analyzing experimental data. This is in conflict with the short attenuation lengths expected for the reflected waves. Since we are mainly interested in φ_{ref} and (as we surely know φ) the change of $k_{\mathrm{ref},x}$ can be used as reference for the starting point of fits — i.e. where the wave can be regarded as a plane wave. From **b** it is determined to at least $1\,\mathrm{\mu m}$ away from the interface for the reflected wave. Since $k_{\mathrm{in},x}$ is more heavily influenced by the bending, we accept fitting errors for the parameters of the incoming wave since it cannot be easily disentangled from the reflected wave in an interference pattern. On the upside, the more important values for the reflected wave are still trustworthy.

The bending can also be observed for the refracted wave. Similar calculations show that the effect is of the same order, therefore the above discussion applies as well for the transmitted wave and for $\varphi = 60°$ the fitting should start at least $1\,\mathrm{\mu m}$ away from the interface.

One should note that these calculations provide an upper bound of the change in k since this approach assumes an adiabatic change of spin wave characteristics with the variation of the effective field [34]. However, this is not true as the wavelength is much larger than the area where these demagnetizing effects are effective.

## 6.4 Angular Dependence of Snell's Law for Spin Waves

In total, six different samples with varying angle of incidence φ_{in} between 10° and 60° in steps of 10° were measured at a fixed excitation frequency of $\omega = 2\pi \cdot 8\,\text{GHz}$. Examples of the raw Kerr data are shown in Fig. 6.8 **a** – **d**. In the data, we recognize the incoming wave in the thick film (left of the grey line) and the refracted wave in the thin film (right of the grey line). When accurately analyzing the dynamic magnetic contrast in medium 1, a reflected wave can be observed as well. To emphasize the reflected waves, we show linescans along the wave fronts of the incoming waves in Fig. 6.8 **i** – **l**, corresponding to the blue lines in the images.

As clearly seen in the images, k is significantly enhanced behind the thickness step. This means that the natural limit for short wavelength spin wave generation given by the geometrical constraint of the CPW can be elegantly overcome. Furthermore, near the interface the signal in the thin part of the Py film is substantially larger than in the thick part. This is counter-intuitive at first, since the refracted wave is induced by the incoming wave. However, the combined action of exchange and dipolar interactions leads to an increased excursion angle. To avoid dynamic magnetic charges, purely dipolar coupling would lead to a doubling of the excursion angle (since the thickness ratio of the two media is 2:1). At the same time, exchange prefers reducing the tilt angle between the precessing magnetic moments in both media. As a result, the Kerr signal increases by a factor of 1.5 – 1.7. Note that an increased demagnetizing field in the thin film also contributes to the deviation from the factor of two. The enhancement of the amplitude is an important point and means that we can in fact boost the signal some distance from the excitation, thus counteracting natural attenuation by damping. This is a local effect, since the attenuation length in the thin part becomes shorter mainly due to the reduction of the group velocity that scales linearly with thickness. The attenuation length is further reduced since k increases and since the propagation direction tilts away from the DE geometry. However, a net boost of the signal can clearly be observed some micrometers away from the interface.

To further analyze the experiments, we fit the data for the refracted waves to obtain the quantities of interest, namely wave vector amplitudes k_{tra} and the angles of refraction φ_{tra}. Additionally, amplitude, phase, and attenuation length are included in this model as described in Sec. 6.1. The thick part is fitted with a superposition of incoming and reflected wave yielding k_{ref} and φ_{ref}. The fits are displayed in Fig. 6.8 **e** – **h**. Care is taken that bending near the interface and caustics from defects (e.g. in **d**) are not disturbing the fits.

The results extracted from the data are presented in Fig. 6.9. They are compared to the expectations for Snell's law in optics (green lines), i.e. for a wave propagating in an isotropic medium with a relative refractive index of 2 between the two media. The orange line is determined as described in Sec. 6.2. As already anticipated from the iso-frequency curves, a significant deviation from Snell's law in optics is observed for incidence angles $\varphi_{\text{in}} > 25°$ in the case of refraction and $\varphi_{\text{in}} > 10°$ in the case of reflection.

One of the important results that we conclude from our experiments is that the wave vector can be very efficiently enhanced for incidence angles $\varphi_{\text{in}} > 25°$. We observe that, while the refracted angle starts decreasing again for $\varphi_{\text{in}} > 40°$, k_{tra} keeps increasing due to the anisotropic dispersion relation (in the case of reflection, a decrease is observed for
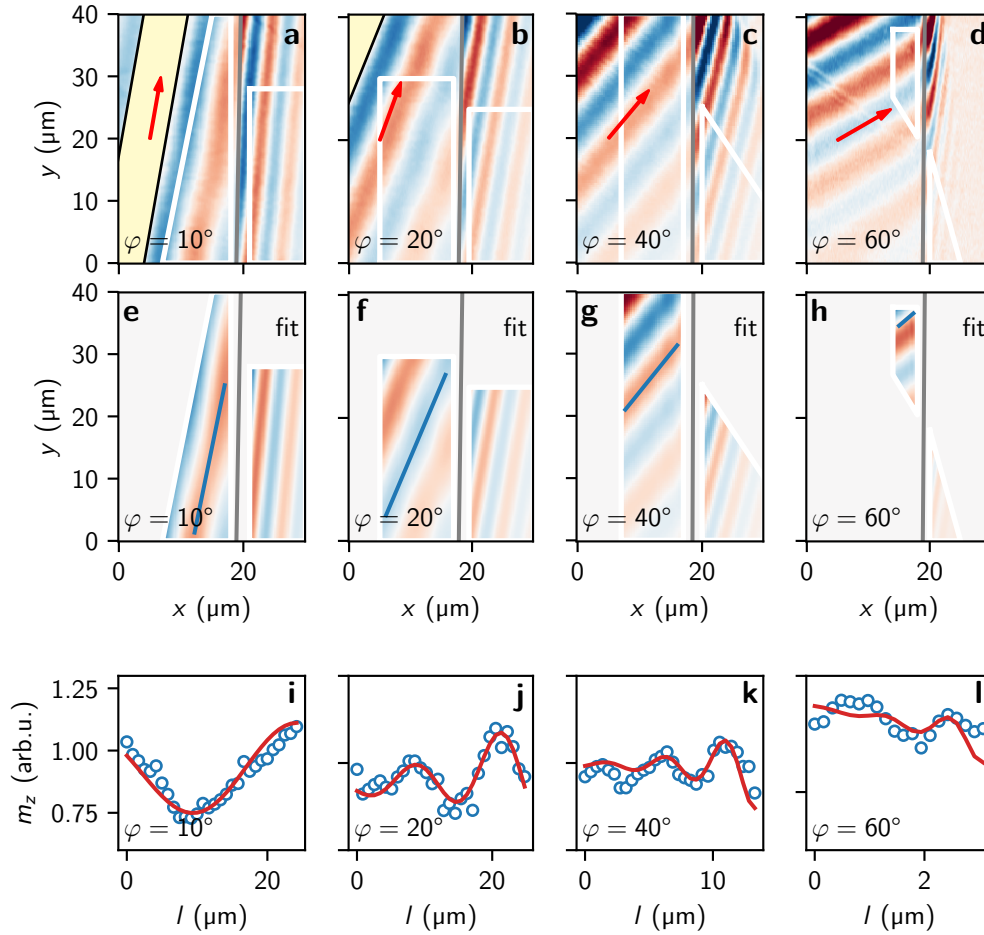
Figure 6.8: Experimental results and fits for four samples. Columns show experimental data (first row), 2D fits (second row), and line scans of both data and fit (third row) for samples with $\varphi_{in} = 10°$, 20°, 40° and 60°. In the images, the gray line marks the step between thick (on the left) and thin (on the right) Py. The white box indicates the area of the fit. The data is recorded at a fixed frequency of $f = 8\,\text{GHz}$ and an external field of $\mu_0 H_{ext} = 54\,\text{mT}$ directed along the wave fronts of the incoming wave (red arrows). The color-scale in **c** and **d** is cropped to enhance the contrast in the areas with lower signal. To emphasize the reflected waves, **i** – **l** show line scans along the blue lines in **e** – **h**. The blue dots are interpolated from the data, the red lines are extracted from the fits. The quantity l denotes the distance from the lower left to the upper right of the blue lines.
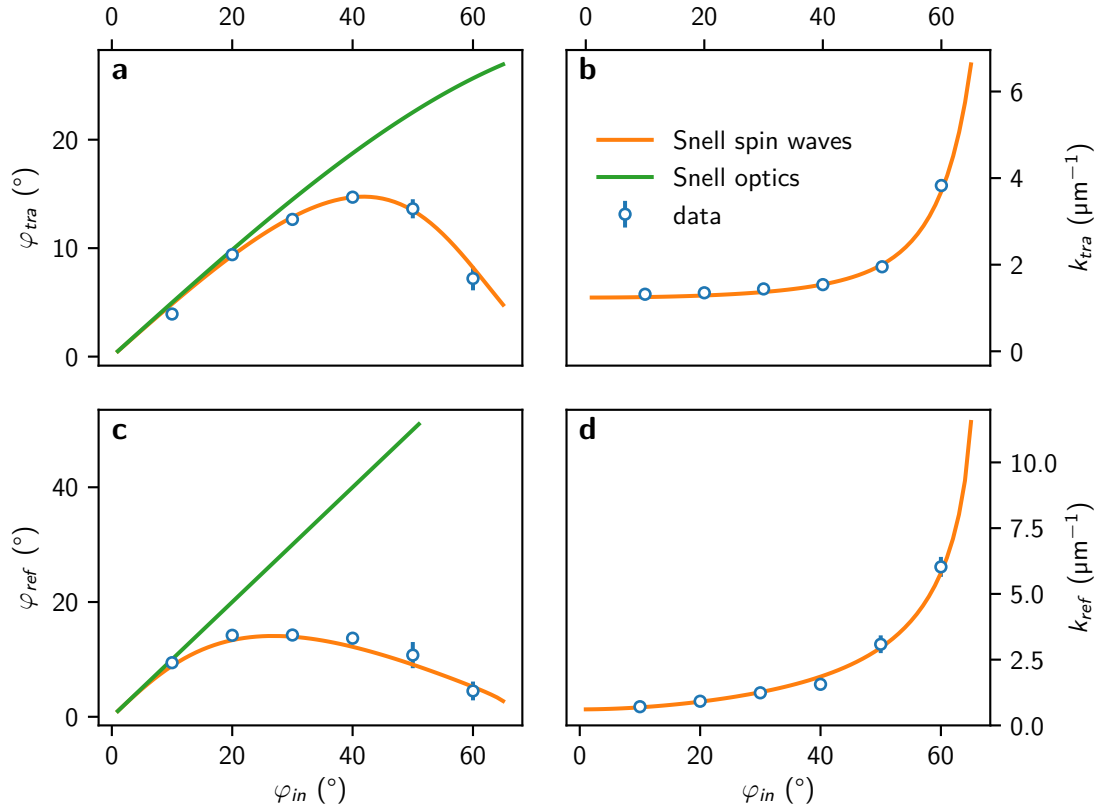
Figure 6.9: a Refracted angle φ_{tra} **b** refracted wave vector magnitude k_{tra} **c** reflected angle φ_{ref} and **d** reflected wave vector k_{ref}, all shown versus incident angle φ_{in}. In all graphs, the blue dots are experimental values. The green line shows Snell's law for an isotropic dispersion relation and the orange curves Snell's law for spin waves. The latter are calculated with the help of Snell's law and the anisotropic dispersion relation, Eqs. (6.2) and (2.38), as described in the main text. The data was recorded at an external field of $\mu_0 H_{ext} = 54\,\text{mT}$ and an excitation frequency of $8\,\text{GHz}$. The error bars are the result of least square fitting.

$\varphi_{\mathrm{in}} > 25°$) . Essentially, to match the condition of Snell's law and the dispersion relation at the same time, the wave vector needs to increase considerably for dipolar spin waves: on an iso-frequency curve, DE spin waves have the lowest k. This allows reducing the wavelength efficiently. By contrast, in an isotropic system — where the wave vector is solely determined by the refractive index, which is generally not angle dependent — it would stay constant. In addition, we qualitatively found an increase of Kerr signal behind the thickness step, effectively boosting the wave. We expect this feature to increase with smaller L_{thin}, which will be further investigated in the following chapter.

We conclude that Snell's law for spin waves in the dipolar regime can be predicted with high accuracy. Our experiments can be fully reproduced by incorporating the anisotropic dispersion relation. We find efficient spin wave steering due to the step interface while at the same time the wavelength of the spin waves can be reduced. In the vicinity of the interface, a signal boost is observed that we attribute to dynamic dipolar coupling. Our findings are of relevance in the field of magnonics, where efficient spin wave steering remains a problem to be solved. Note that Snell's law in the form presented here, should also hold for hetero-interfaces composed of different magnetic materials. In this case, the material parameters (e.g. saturation magnetization and gyromagnetic ratio) of the different regions have to be inserted in Eq. (6.3).

7 Thickness Dependence of Refraction

Parts of the present chapter are published in Ref. [24].

The targeted generation of coherent spin waves with small wavelengths is challenging, since the standard way of generating spin waves is linked to using microwave antennas whose dimensions put a natural limit on the wavelength, as discussed in Sec. 2.7. Overcoming this limit is a field of research in magnonics: Demidov et al. injected spin waves into a tapered Py stripe and observed that, as the internal field gradually decreases the wave vector magnitude increases [25]. Yu and coworkers made use of the so called grating coupler effect, where an array of ferromagnetic disks is structured on top of an insulating ferrimagnetic YIG film [26, 2]. There, modes that match the periodicity of these arrays are resonantly enhanced in excitation efficiency. Approaches that circumvent the use of an antenna are pursued as well: they include spin torque nano-oscillators [70, 133] or the use of magnetic textures like vortices [74] and domain walls [134, 73].

In this chapter, we will further analyze the refraction at thickness steps with a stronger emphasis on the wavelength conversion and its efficiency. To prevent the static bending that might lead to an inaccurate description of the incident waves, we will direct the field along the interface. Samples with three different thicknesses L_{thin} (10 nm, 15 nm, and 20 nm) and three different angles φ (10°, 20°, and 30°) are investigated.

7.1 Fitting and Characterization

In contrast to Sec. 6.4, we use different fitting functions. Instead of two independent fits for thin and thick part, we fit both regions (again marked with a white polygon) within a single step. This allows us to make direct use of Snell's law for spin waves by fixing the tangential component of the **k**-vector directly in the fit for all three waves. As has been shown in the previous section, Snell's law holds and we can therefore reduce the number of independent variables. This will be especially useful in the definition of reflection and transmission coefficients as well as phase shifts between waves.

The knowledge about a possible rotation of the sample axis with respect to the image axis is mandatory for this goal. We call this angle φ_{off} and it is determined by the topography image, where the two thicknesses have different contrast. The angle φ_{off} is positive when the sample is rotated counter-clockwise with respect to the image axis. This situation is depicted in Fig. 7.1. The angle β — defined as propagation direction with respect to the image axis — can then be expressed as

$$\beta_{\text{in}} = -\varphi_{\text{in}} + \varphi_{\text{off}} \,,$$
$$\beta_{\text{tra}} = -\varphi_{\text{tra}} + \varphi_{\text{off}} \,,$$
$$\beta_{\text{ref}} = \varphi_{\text{ref}} + \varphi_{\text{off}} - \pi \,.$$
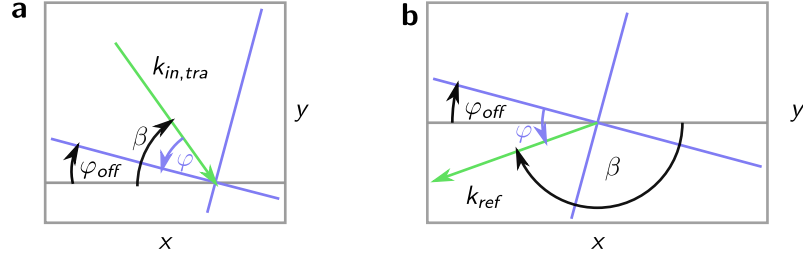
Figure 7.1: Relation of the different angles φ_{off}, β, and φ, that are used in the main text. Gray lines are the image axis. Blue lines mark the interface and interface normal. The situation differs for incoming and reflected wave as shown in **a** and **b** respectively. All angles have a positive sign if the arrow points counter-clockwise and a negative sign if the arrow points clockwise.

The fitting function Eq. (6.1) can be utilized again for the thin part, while the superposition of two such functions can be used for the thick part. Within the fitting function, we can then reduce the number of parameters by calculating two out of three angles φ by

$$\varphi_{\text{ref,tra}} = \arcsin\left(\frac{k_{\text{in}}}{k_{\text{ref,tra}}}\sin(\varphi_{\text{in}})\right)$$
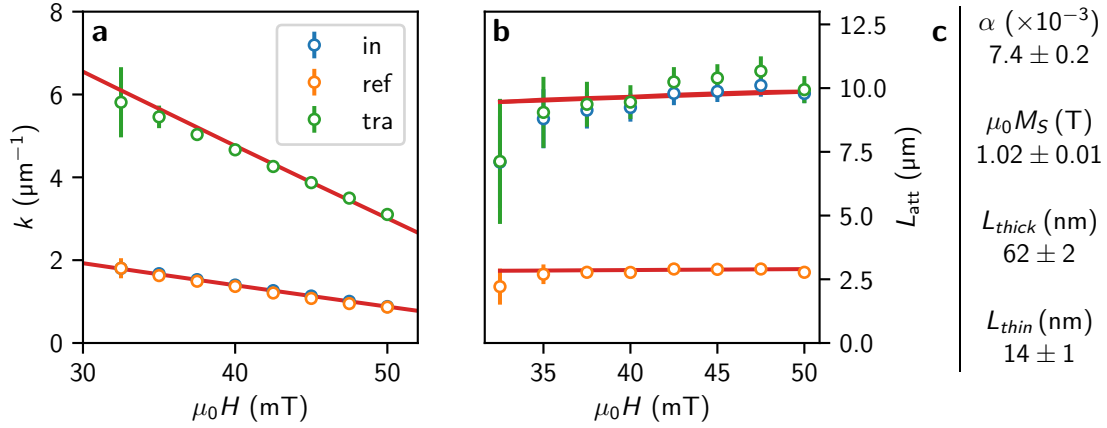
and a single attenuation length

$$L_{\text{att}}^{\text{ref,tra}} = L_{\text{att}}^{\text{in}}\frac{\sin(\varphi_{\text{ref,tra}})}{\sin(\varphi_{\text{in}})} \ .$$

In a single step, the residual of both thin and thick part is minimized to yield amplitude, phase, and wave vector for each of the three waves. Additionally, one attenuation length $L_{\text{att}}^{\text{in}}$ and one angle β_{in} are obtained, from which all other attenuation lengths and angles can be calculated by the above equations. This procedure is equivalent to demanding the conservation of both real and imaginary part of the wave vector component along the interface.

To illustrate the process of the characterization, we show the values obtained for a sample with nominal thickness of the thin film $L_{\text{thin}} = 15\,\text{nm}$ and the incident angle $\varphi = 30°$ in Fig. 7.2 **a**. As in the preceding chapter, the wave vector shows a linear dependence on H. The reflected wave almost perfectly matches the wave vector magnitude of the incoming wave, since the angle of external field with the propagation direction is equal in both cases. This field sweep is used for an implicit fit to the dispersion relation Eq. (2.38). With a fixed gyromagnetic ratio $\gamma = 185\,\text{GHz}\,\text{T}^{-1}$, we retain the parameters saturation magnetization $\mu_0 M_{\text{S}} = 1.02 \pm 0.01\,\text{T}$, $L_{\text{thick}} = 62 \pm 2\,\text{nm}$, and $L_{\text{thin}} = 14 \pm 1\,\text{nm}$, using a single set of parameters for incoming, reflected, and refracted wave. The errors correspond to one standard deviation of the fitting.

Fig. 7.2 **b** shows the field dependence of the attenuation length. The result is a rather flat dependence of the attenuation length on the external field. This is expected from

Figure 7.2: **a** Dependence of wave vector magnitudes k and **b** the attenuation lengths L_att on the external magnetic field for a sample with $\varphi = 30°$ and $L_\text{thin} = 15\,\text{nm}$. Dots are experimental data and red lines correspond to fits to the dispersion relation as described in the main text. **c** shows the values obtained by the fit.

Eq. (2.41), i.e.

$$L_\text{att} = v_G \cdot \frac{2}{\alpha \gamma \mu_0 (2H + M_\text{S})}\,,$$

since $2H$ is significantly smaller than M_S in the sum in the denominator and v_G only weakly depends on H. To fit the data, we make use of the parameters obtained for the field dependence of the wave vector. The vector $\mathbf{v}_\text{G}$ is then calculated for the waves and projected onto the direction of the wave vector. Again, the data for all three waves is used to fit to a single parameter $\alpha = 0.0074 \pm 0.0002$. As shown in Sec. 2.6, the dependence of τ on the direction of the static magnetization for the in-plane configuration is rather weak and therefore neglected.

All values obtained in this section are close to standard values of Py and reflect the nominal thicknesses of the individual films (within the error). Similar field-sweeps for the other thicknesses L_thin give comparable results. A proper quality of Py films is thus ensured and allows for comparison between the samples.

7.2 Main Results

Figure 7.3 shows the experimental data on the thickness dependence of the wave refraction. It is taken on a sample with $\varphi = 30°$ and an external field of $50\,\text{mT}$. The magnitude of H is chosen slightly off the maximum of antenna excitation efficiency to allow for the identification of the transmitted wave. For smaller fields, k_tra increases and the wave becomes harder to spot, although it is still possible to fit the parameter.

Figure 7.4 summarizes the parameters obtained by the data in Fig. 7.3. The wave vector magnitude k (**a**), the attenuation length L_att (**b**), and the angle with respect to the interface normal φ (**c**) remain constant within the error for incoming and reflected wave, as expected for an external field applied along the interface. The quantity k_tra increases non-
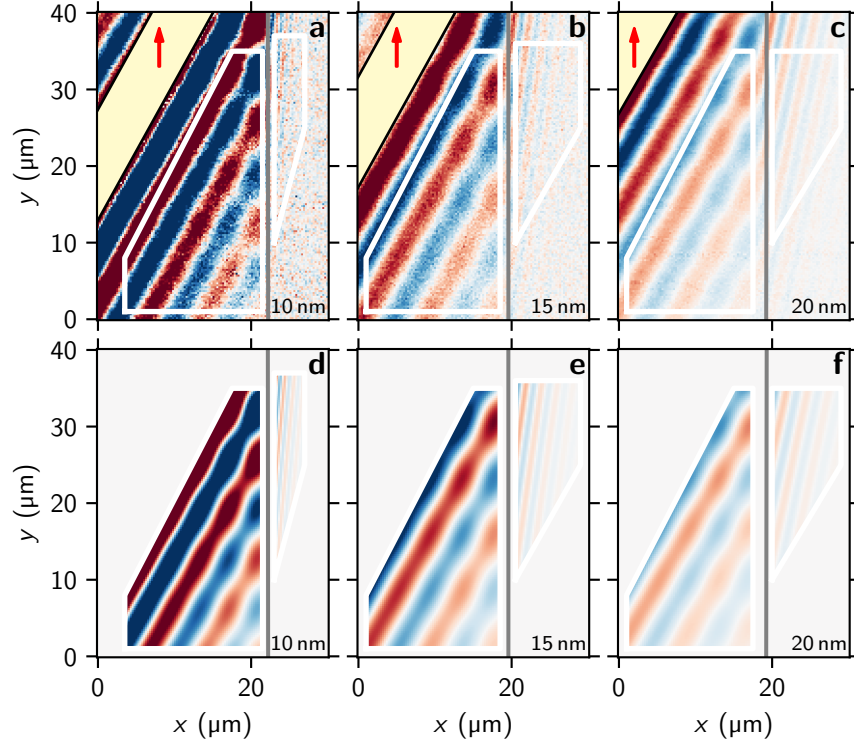
Figure 7.3: **a – c** Data recorded at $f = 8\,\mathrm{GHz}$ and $\mu_0 H_{\mathrm{ext}} = 50\,\mathrm{mT}$ for an incident angle of $\varphi = 30°$ for thicknesses of 10 nm, 15 nm, and 20 nm, respectively. **d – f** Corresponding fit obtained as described in the main text. Note, that the color code is clipped in order to facilitate the recognition of the spin wave in the thin part.

linearly with decreasing thickness, reflecting the dependence $k \propto L^{-1}$ in Eq. (6.3). Note that this dependence does not hold for all angles, since φ_{tra} also depends on L_{thin}, as seen in subplot **c** and also in the raw data (Fig. 7.3). The attenuation length of the transmitted wave increases linearly due to a linear dependence of the group velocity on the thickness. In **d**, a transmission coefficient T, defined as the ratio of amplitudes of transmitted versus incoming wave at the interface, is plotted in green. Likewise, a reflection coefficient R is defined as the ratio of amplitudes between reflected and incoming wave (orange data). The latter will be investigated further in the following chapter and is plotted for completeness.

As reported in the previous chapter, a transmission coefficient $T > 1$ is possible. This finding is confirmed for $L_{\mathrm{thin}} = 20\,\mathrm{nm}$. However, for lower thicknesses of the thin film, the transmission ratio drops linearly — in contrast to the expectancy in the previous chapter. Other incident angles show qualitatively similar behaviors. It is noteworthy, that we have a finite optical penetration depth of roughly 15 nm in Py [135], which complicates the interpretation of T. For all except the 10 nm film this should be negligible, since we always probe the same top part of the films. In the case of $L_{\mathrm{thin}} = 10\,\mathrm{nm}$, the value given is therefore underestimated as less light contributes to the Kerr signal.
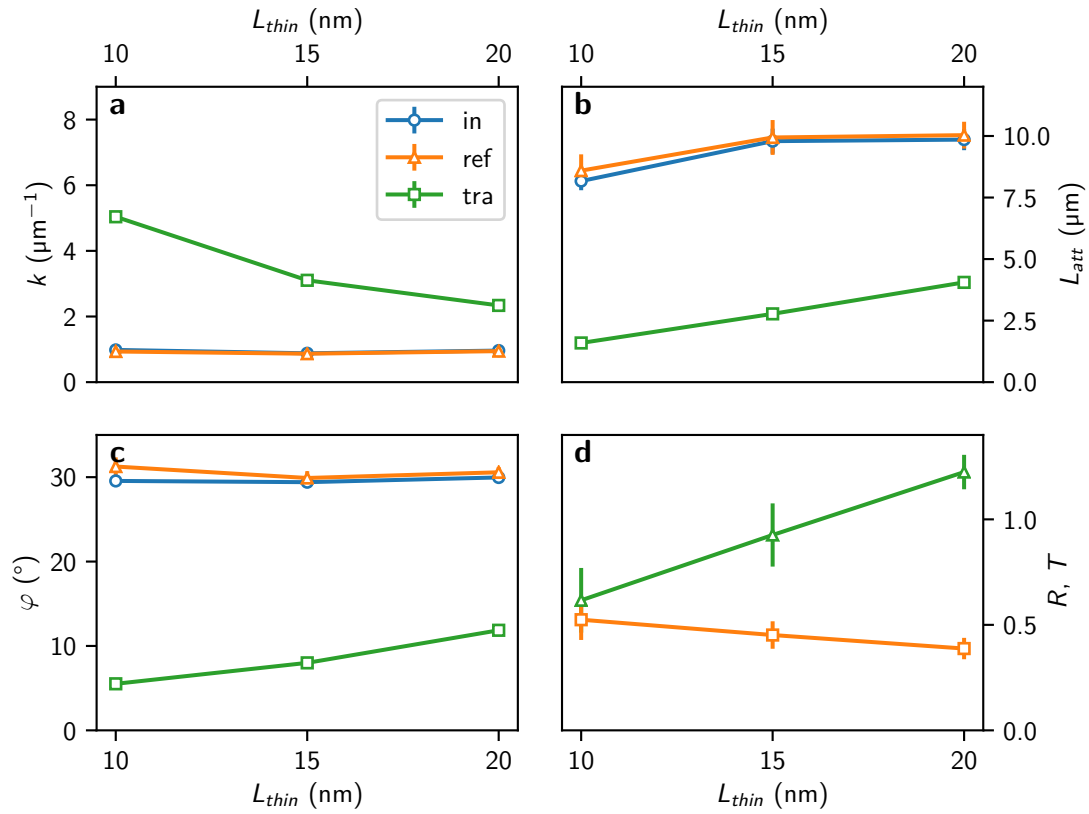
Figure 7.4: Summary of thickness dependence for an incident angle of $\varphi = 30°$ at an external field of $\mu_0 H_{ext} = 50\,\text{mT}$. The values are directly obtained from the fits in Fig. 7.3. **a – c** Wave vector magnitude k, attenuation length L_{att}, and angle with respect to the interface normal φ, respectively. *in, ref,* and *tra* denote incoming, reflected, and transmitted waves. **d** Transmission coefficient T (and the reflection coefficient R), defined as the amplitude ratio between transmitted (reflected) and incoming wave — evaluated at the interface.
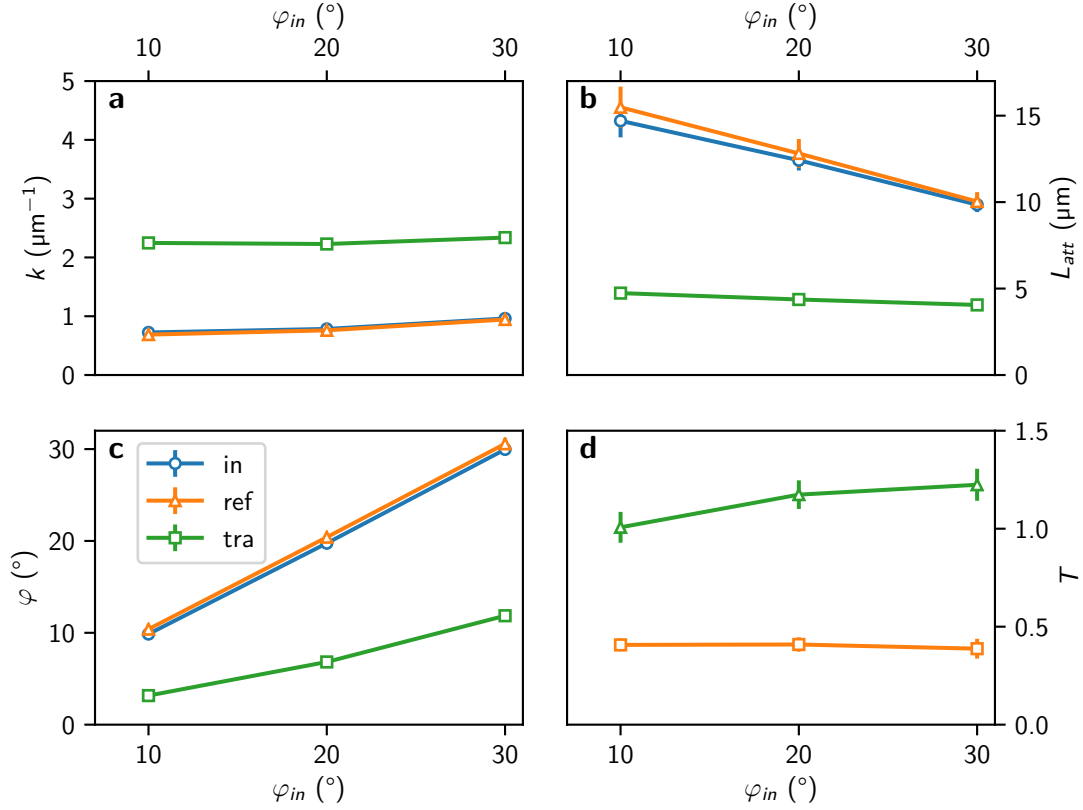
Figure 7.5: Angular dependence of **a** the wave vector magnitudes, **b** the attenuation lengths, **c** the wave vector angles with respect to the interface normal, and **d** the transmission coefficient. The data is recorded at an external field of $\mu_0 H_{\text{ext}} = 50\,\text{mT}$ and $L_{\text{thin}} = 20\,\text{nm}$. The legend is as in Fig. 7.4.

From the data presented here and in the previous chapter, we expect a particular thickness ratio, that maximizes T. A theory that predicts T would be desirable to effectively calculate this *sweet spot* of thickness ratios for the refraction process. The complicated part in formulating such a (quasi-) analytical theory is the 3-dimensionality of the problem: besides the obvious dependence on x and y in our comparably thick 60 nm film, the surface character of spin waves might already play a role. Even if the problem can be treated in thin film approximation, the combined (non-local) demagnetizing fields of incoming, refracted, and reflected wave have to be taken into account. One route towards this goal might be the utilization of dynamic magnetic susceptibilities introduced in Sec. 2.7. With their help, the magnetic response of the thin film to dynamic stray and exchange fields of the thick film could be studied. Experimentally, these may be verified by introducing a small gap between thin and thick film, thus prohibiting an influence of exchange. Similar numerical calculations as in Sec. 3.2.2 might provide additional insight into the refraction process.

To further verify such a model, the angular dependence for $L_{\text{thin}} = 20\,\text{nm}$ is depicted in Fig. 7.5. The wave vector magnitudes of incoming and reflected waves, shown in **a**,

decrease with smaller incident angle as the dispersion approaches the minimum of k with respect to the angle of the external field. The minimum of the incoming wave vector magnitude is reached for a wave traveling along x-direction ($\varphi_{in} = 0°$). Note, that this propagation is perpendicular to the static magnetization, i.e. the DE configuration. This can be also seen in **b**, where the respective attenuation lengths increase by lowering φ_{in}, since the DE geometry also has the highest group velocity. As φ_{in} tends to zero the ratio of transmitted k (k_{tra}) to incoming k (k_{in}) approaches the ratio of $\frac{L_{thick}}{L_{thin}} = 3$, because the dispersion of DE spin waves only contains dependencies of $k \cdot L$. In Fig. 7.5 **c**, the angles of reflection and refraction are shown. The incoming angle, shown in blue, matches the angle of reflection, as the corresponding k-vectors share the same angle with the static magnetization. Subplot **d** shows the transmission coefficient. Within the error, there is only a small difference between the values obtained for different incident angles with a slight increase of T with increasing angle. As a result, the efficiency of the transmission process seems to be slightly favoring larger angles investigated here.

In conclusion, we examined the transmission of spin waves through different thickness steps. To gain insight into the magnetic film properties as well as the refraction process, we also studied the dependence on the external magnetic field and the incident angle, respectively. The increase in the wave vector magnitude scales with the thickness of the film and can be seamlessly tuned to produce a desired wave vector in the sub-micrometer range. The downside of the up-conversion of wave vectors is the enhanced wave attenuation, which is mainly due to a reduced group velocity in thinner films. However, the reduced group velocity is a characteristic of the dispersion relation and is therefore shared by all wavelength-conversion techniques that aim to inject waves in such a film.

As shown in our experiments, a conversion with a factor of 3–4 is achieved with a high transmission efficiency. In this range of wave vectors, the use of a thickness step is attractive from a technological viewpoint, especially because the main alternative — the grating-coupler technique [26, 2] — can reach even lower wavelengths but only allows for conversion efficiencies of approximately 0.2 between fundamental and higher-order modes. Care must be taken when designing devices that feature these large wave vectors. If the dispersion is increasingly influenced by the exchange interaction, the k ratio no longer matches the thickness ratio.

8 Goos-Hänchen-Like Phase Shift for Spin Waves

Parts of the present chapter have been published in Ref. [36].

In optics, a light beam experiences a spatial shift in the beam plane upon total internal reflection, which is usually referred to as the Goos-Hänchen (GH) shift [31, 136]. Recently, it has been proposed for spin waves for different geometries of wave vector **k** and static magnetization [32, 33, 34, 35]. Depending on the geometry and wave vector magnitude k, it is expected to be useful in characterizing interfaces [32, 34] or to reveal Berry curvature effects in the dispersion of spin waves [35]. It is also related to the so called spin wave bending [33] investigated in Sec. 6.3. Owing to these different sources, the GH shift should be observable over many orders of magnitude of k. In the context of magnonics it therefore needs to be considered in any scheme that involves the reflection of spin wave beams [137].

In the dipolar regime, it is not straightforward to realize coherent, non-diffracting spin wave beams [118, 138] and to directly observe a GH shift. However, according to the so-called stationary phase method [30] discussed in the following section, a phase shift between an incident and its reflected plane wave is the basis of the GH shift of beams, as
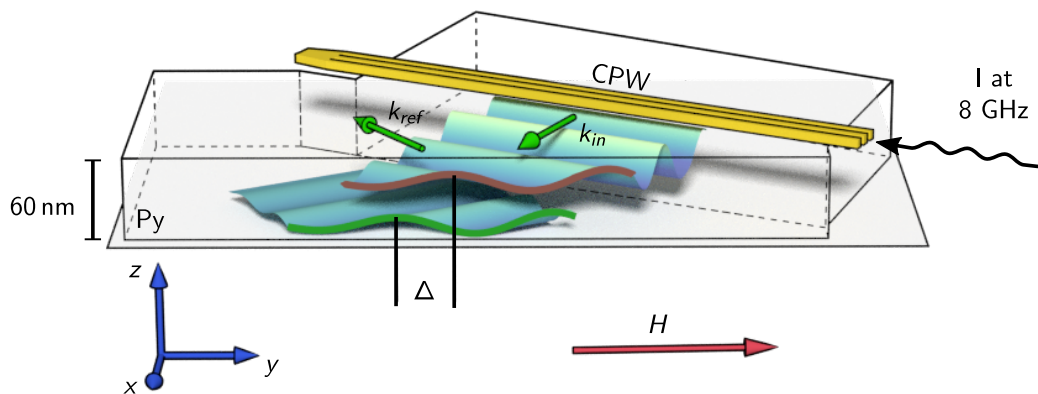
Figure 8.1: Sketch of the experiment: A spin wave hits the edge of a Py film. Upon reflection, the side the spin wave is traveling on is switched from top to bottom, and a phase shift Δ is observed. Brown and green curves mark the cut lines of incoming and reflected wave with the sample edge. The shift Δ can be defined as the distance between two maxima. A static external field is applied along the edge in y-direction and $f = 8\,\mathrm{GHz}$.

long as it depends on the wave vector component along the interface. The study of this phase shift reveals all physics governing the GH shift and it can therefore be regarded as the fundamental quantity.

By using the sample design as presented in Chapter 5 with $L_{\mathrm{thin}} = 0$, the reflected wave is studied to investigate this phase shift. An overview of the experiment is given in Fig. 8.1. As in the previous chapter, the static external field is applied along y-direction such that no static demagnetizing fields arise. After reflection, the wave will change the side it is traveling on and by evaluating fits to the interference pattern, the phase shift Δ can be obtained. The results for different external field magnitudes are presented in Sec. 8.2. Note, that this switch of sides can cause a shift between the observed waves of the order of the film thickness $L_{\mathrm{thick}} = 60\,\mathrm{nm}$. As will be evident later, this effect is negligible compared to the shift we observe.

Different samples with angles φ will be investigated to prove a dependence on k_y in Sec. 8.4. To explain our results, we employ numerical simulations in Sec. 8.3, as no prediction covers our experimental findings. References [32, 33, 34, 139] mostly consider exchange dominated spin waves. There, the main contribution to the phase shift are either surface anisotropies or the exchange coupling to a second film. Both influence the exchange boundary conditions. Since the effect of exchange is weak in our wave vector regime, we seek for explanations involving dipolar interactions. In Refs. [140, 34], boundary conditions for magnetostatic spin waves are derived. In these articles, only the case of the static magnetization pointing perpendicular to the edge is considered and therefore the dynamic magnetization does not have components perpendicular to the interface, which would create dynamic charges. As a result, the effect is dominated by static bending of spin waves. Ref. [35] predicts a GH shift for the magnetization pointing out-of-plane. The proposed Berry curvature effect that is responsible for this shift is claimed to vanish for the magnetization in the plane [141, 142, 143]. In the experimental works [144, 145], a phase jump for standing spin waves is proposed — which is equivalent to a phase shift for spin waves upon reflection — but not quantitatively examined. A theory that accounts for dipolar effects at boundaries was developed by Guslienko et al. [101, 102]. There, only the special case $k_y = 0$ is investigated.

In Sec. 8.3, we utilize the numerical model described in Sec. 3.2.2, which allows for finite k_y to describe the experimentally observed phase shift. Finally, this chapter concludes with the experimental results of the angular dependence of the phase shift, which are compared to the numerical investigations.

8.1 Stationary Phase Method

The so called stationary phase method was developed by Artmann [30]. It gives quick insight on the influence of a phase shift between an incoming and reflected plane wave for a beam. Since a beam is laterally confined, it can be understood as a superposition of (possibly infinitely many) elementary plane waves with different amplitudes. Mathematically, the Fourier transform provides these amplitudes. Artmann's method revolves around these elementary waves for the description of the Goos-Hänchen shift.

We consider a plane wave with an amplitude of unity incident onto an reflecting surface,

infinitely extended along y-direction. It can be described by $\Psi_{\mathrm{in}} = \mathrm{e}^{\mathrm{i}(-k_y y)}$ on a particular cut parallel to the interface in a coordinate system like the one described in the previous chapters. The reflected wave is $\Psi_{\mathrm{ref}} = \mathrm{e}^{\mathrm{i}(-k_y y + \Phi)}$ with a phase shift Φ with respect to the incident wave. A second elementary wave $\Psi_{\mathrm{in}}^{(2)}$ with neighboring wave vector component $k_y + \delta k_y$ will in general cause a reflected wave $\Psi_{\mathrm{ref}}^{(2)}$ with a phase shift $\Phi + \delta\Phi$. The interference of both reflected waves will exhibit a beating with its maxima at

$$-\delta k_y y + \delta\Phi = 2\pi\nu\,,$$

with an integer ν. If Φ does not depend on the wave number, then $\delta\Phi = 0$. The distance between the maxima of a reflection with and without dependence on k can be calculated as

$$Y = y(\delta\Phi) - y(\delta\Phi = 0) = \frac{\delta\Phi}{\delta k_y}$$

and considering the limit $\delta k_y \to 0$, we obain

$$Y_{\mathrm{GH}} = \frac{\partial\Phi}{\partial k_y}\,, \tag{8.1}$$

where Y_{GH} is the Goos-Hänchen shift along y-direction expected for beams. This equation has been used in Refs. [140, 33, 34, 139] to describe GH shifts for spin waves. It is also clear that the same derivation could have been carried out for a "time-like" phase, causing a time delay of waves upon reflection, when Φ depends on t [140]. Difficulties usually arise in the derivation of Φ which is the quantity that will depend on the nature of the wave propagation and therefore differs for different kinds of waves.

8.2 Field Dependence of Reflection

To determine a phase shift at the interface, it is obviously crucial to accurately determine the position of the edge. For this purpose, we use the topography data that is recorded simultaneously with the Kerr data. An example of such an image is given in Fig. 8.2 **a** for a $\varphi = 30°$ sample. The exact position of the edge as well as a possible tilt φ_{off} with respect to the image axis is determined by a fit to this topography data. Figures 8.2 **b** and **c** show a line scan at $y = 20\,\mu\mathrm{m}$ and its gradient, respectively. The latter is fitted with a general 2D elliptical Gaussian function with infinitely extended width along the direction of the edge. The width perpendicular to the edge is a measure of the focus of our laser beam. We determine it to about $400\,\mathrm{nm}$ full-width half-maximum in the given experiments. In all three graphs, the so-determined-edge is marked by a gray line, the red line in **c** is one line cut of the fit.

The Kerr signal of the same measurement can be found in Fig. 8.3 **a**, for an external field of $45\,\mathrm{mT}$. A shift between Kerr and reflection data is avoided by scanning the sample in a meander like path. In **c**, the field is reversed with the most obvious consequence being that the dynamic contrast is larger to the left of the antenna due to the excitation non-reciprocity. By further comparing the two images, it seems that the checkerboard-like interference pattern is slightly more pronounced in **c**. Additionally, the wave neither
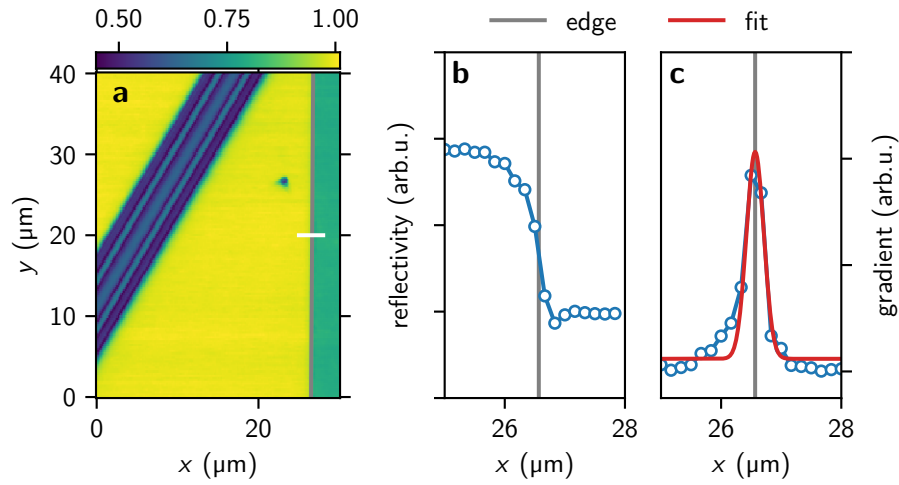
Figure 8.2: **a** Reflectivity of a sample with $\varphi = 30°$. A line scan at $y = 20\,\mu m$ (white line in **a**) is shown in **b** and its gradient **c** is fitted with a Gaussian (red line) to determine the position of the step (gray line in all figures). Note that the whole image contributes to the fit and the red line only represents a single line cut.
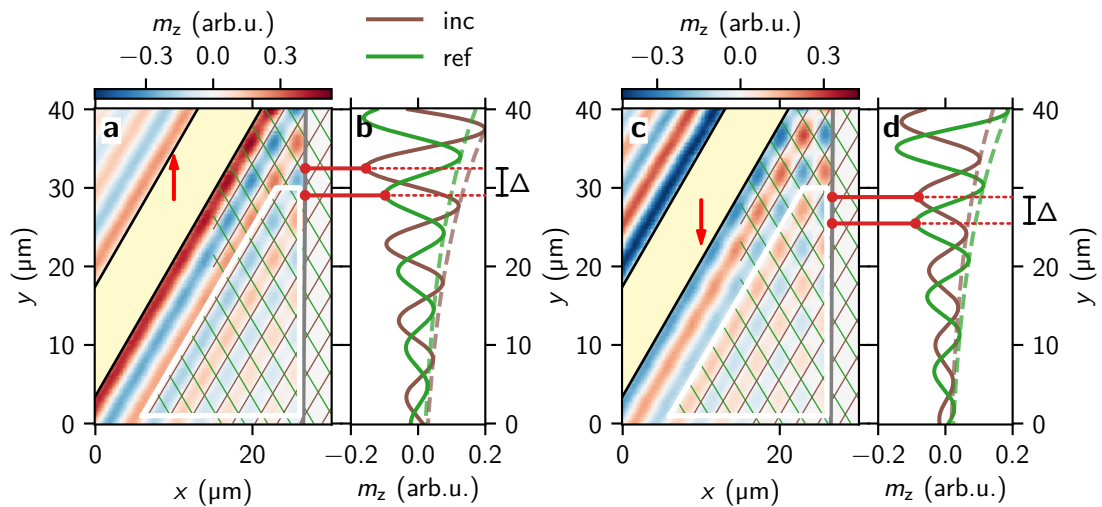
Figure 8.3: **a** and **c**: Typical experimental data, recorded at $\mu_0 H_{ext} = 42.5\,mT$ on a sample with incident angle of $\varphi = 30°$. They differ by the direction of the external field (red arrow). The interference pattern is fitted in the white box. Green and brown lines correspond to the so-determined phase fronts of incoming and reflected waves, respectively. **b** and **d** show the respective fits evaluated along the interface. The phase difference in real space Δ is evaluated as the distance between the horizontal red lines. The reflection coefficient R can be calculated from the ratio of the amplitudes of both waves, corresponding to the dashed lines in **b** and **d**.

exhibits a maximum nor a minimum at the edge, which corresponds to partially pinned boundary conditions.

To quantify these impressions, the data is fitted with a superposition of two plane waves in the area indicated by the white box. Wave fronts of incident and reflected waves are highlighted by brown and green lines, respectively. As described in Sec. 7.1, the tangential components of the incident and reflected complex wave vectors share a single fitting parameter, i.e. $k_y^{\text{in}} = k_y^{\text{ref}}$ and $L_{\text{att},y}^{\text{in}} = L_{\text{att},y}^{\text{ref}}$. Errors are calculated with the help of a bootstrap analysis. We take twice the standard deviation of the residual of the fit and generate normal distributed random data with this standard deviation. Afterwards, the fit and calculation of the parameters is repeated. An uncertainty of the position of the edge is also included (100 nm), as this is a crucial part in the determination of a shift and dominates the error in most cases. After repeating these steps 100 times, twice the standard deviation of the set of resulting parameters yields a 95% confidence interval of each fitted or calculated parameter. The error bars in the following figures delimit this interval.

In the next step, the fit is evaluated along the edge. Incident and reflected waves are plotted separately in Fig. 8.3 **b** and likewise for the reversed field in **d**. The red dots indicate the position of two nearest minima of the waves. We define the absolute shift Δ as the distance between the two red horizontal lines. The reflection coefficient R is the ratio of amplitudes of the reflected wave and the incoming wave (dashed lines). The quantities Δ and R together with the wave vectors of both waves are the primary parameters extracted from the raw data.

For further calculations, we normalize Δ to a phase shift in units of radians by defining $\Phi = -\Delta \cdot k_y$. From the definition of the shift, it is also clear that we can access Φ only up to translation by integer multiples of 2π. By convention, we choose the shift to be in the interval $-\pi$ to π. Zero shift corresponds to an in-phase reflection, i.e. the interference pattern of incident and reflected waves has a maximum at the edge. This corresponds to unpinned boundary conditions. By contrast, a phase shift of $\pm\pi$ implies a trough of the interference pattern, i.e. the dynamic magnetization is pinned at the interface. Note that k_y is negative and Δ is positive in the given coordinate system.

Similar images are recorded for different external fields and both the reflection coefficient and the phase shift are obtained as described above. In Fig. 8.4 **a** the dependence of R on the external field is shown. Since an increase of H causes a linear decrease of the wave vector of incoming and reflected waves, k (as determined from the fit) is indicated on the top axes labels. The wave vector magnitudes of incoming and reflected waves agree very well, as expected in the geometry, where the external magnetic field is directed along the edge. For this reason, k is referring to either wave vector magnitude.

For positive (negative) fields, R is smaller (larger) than unity. Naively, one would expect a reflection coefficient of exactly unity, corresponding to a lossless process. This discrepancy can be explained with the aforementioned surface character of spin waves. The laser penetrates the sample from the top, therefore our measurements are more sensitive on this side. After reflection, the wave changes the side it is traveling on and the fitted amplitude drops or increases accordingly. By changing the direction of the external field, the initial traveling side is switched. The geometric mean of both directions then gives the real reflection coefficient (gray circles), which is in good agreement unity, corresponding
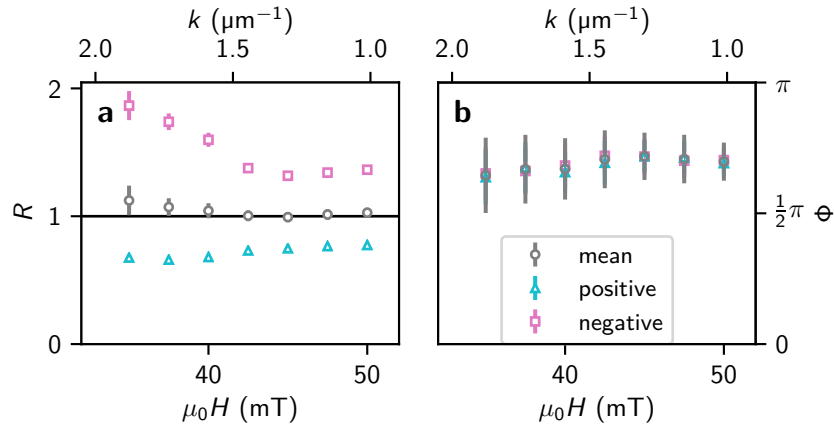
Figure 8.4: a and **b**: reflection coefficient R and phase shift Φ, respectively, recorded on the 30° sample for different external fields. Both field directions (positive and negative y-direction) together with their geometric mean are shown. k indicated on the top axes reflects its linear dependence on H (see e.g. Fig. 7.2). It is determined from the fit and agrees well for both field directions and both incident and reflected wave. All four data sets were used to create this scale.

to the anticipated lossless reflection. For larger magnetic fields, k approaches zero, i.e. the sample is in ferromagnetic resonance. There, the profile is constant, hence R will approach unity for both field directions. This method therefore enables an estimation of the modal profile across z for the wave. Together with simulations of the full film dispersion relation across the thickness, cf. Sec. 3.2.1, it might be possible to access the pinning parameter and its associated anisotropy constant. This is, however, not further pursued in this thesis, since the focus is centered on the phase shift.

In Fig. 8.4 **b**, Φ is plotted for the same measurements. It can be observed that a reversal of the external field yields basically the same values. This experimentally verifies that the the surface character and the side the wave is traveling on do not influence the phase shift between the waves substantially. We deduce that the thin film approximation is suitable to investigate the phase shift further. This will be done numerically in the subsequent section. The data also shows that the shift is neither zero nor π, so the magnetization is neither fully pinned nor unpinned at the interface. In addition, we find a small dependence on the external field, hence on the wave vector.

8.3 Numerical Evaluations

To describe the reflection of spin waves, the numerical model for a stripe, cf. Sec. 3.2.2, is directly utilized. As described there, the result of the simulation is standing waves along x-direction for the dynamic magnetization $\mathbf{m}$ and associated external fields H at which they are excited. Since $\mathbf{m}$ can be interpreted as a superposition of traveling incoming and reflected waves, the model is well suited to describe reflections: in the middle of the stripe, they exhibit defined wave vector components k_x and $-|k_x|$, respectively. An
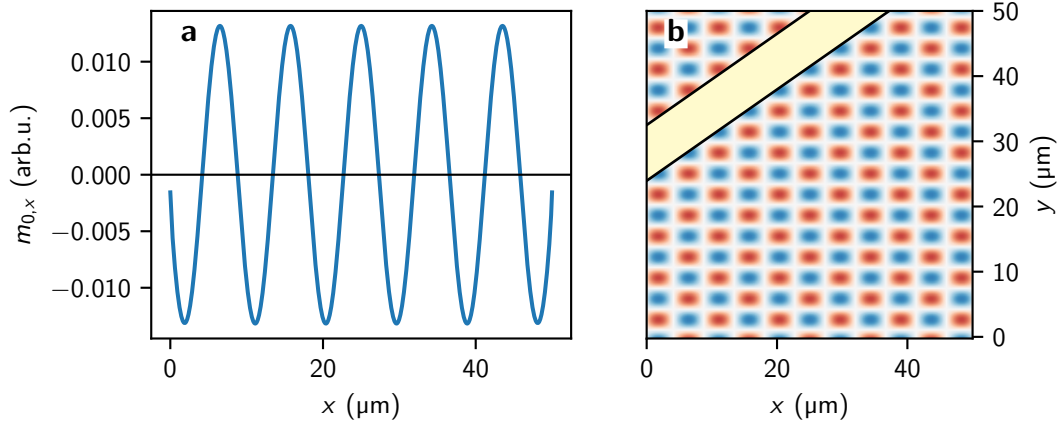
Figure 8.5: Dynamic matrix approach for a stripe. The simulation parameters are given in the main text with $k_y = 1\,\mu m^{-1}$. **a** shows the x-component of the standing wave, corresponding to mode $n = 10$ and $k_x = 0.68\,\mu m^{-1}$ with an eigenvalue of $\mu_0 H = 60\,mT$. In **b** the standing wave is expanded in y-direction by considering the implicit harmonic dependence.

example of one mode obtained by such a simulation is given in Fig. 8.5 **a**. Here and for the following simulations, we once again use standard values of Py, see page 24. The excitation frequency $f = 8\,GHz$ is chosen as in the experiment. The cell size in x-direction is 5 nm and in z-direction 60 nm, corresponding to the thickness of the film. A number of $N = 10000$ cells is used corresponding to a stripe width $L_w = 50\,\mu m$. It is noteworthy, that the magnetization is not fully pinned at the interface, thus resembling the experimental observations.

Together with the implicit harmonic y-dependence, an interference pattern similar as in the experiments — without damping — can be constructed, as shown in Fig. 8.5 **b**. The angle of incidence can be deduced from k_x and k_y, where the former is obtained by fitting the standing wave in the middle of the stripe. In the present situation, it roughly amounts to 60° as indicated by the antenna drawn on top.

A verification of the model is done by means of the full film dispersion relation Eq. (2.38). Here, we employ periodic boundary conditions and compare H obtained from the analytical dispersion relation with H obtained as eigenvalue for the corresponding (fitted) wave vector component k_x. Only few of the eigenvalue-eigenvector pairs are useful, as there is a lower bound of k_x limited by the stripe width w. An upper bound is given by the dispersion relation: with increasing wave vector, H decreases, until there is no field to fulfill the LLG. Next, it is verified that the edges do not influence the modal profiles in the middle significantly by comparing the eigenvalues H of these simulations to the PBC simulations. All three methods agree very well as depicted in Fig. 8.6. A comparison between PBC and analytical values yields an idea of the accuracy of this method, which is in the range of 10^{-5}, roughly corresponding to the error which is introduced when **n** is computed and consequently translates to the error of the eigenvalues and modal profiles. To make sure that the plane wave model is applicable in the middle, modes with mode

Figure 8.6: Comparison between simulations with different boundary conditions (stripe and PBC) and the analytical dispersion Eq. (2.38). For the simulations, k_x is obtained by fitting the standing waves in the middle of the stripe with a sine function. k_y is implicitly fixed to 1 μm^{-1}.
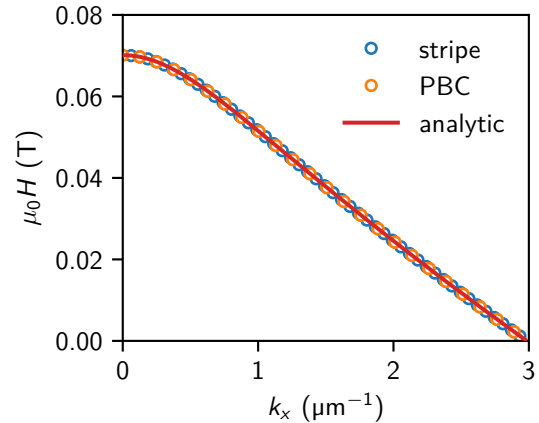
number $n < 10$ are disregarded in the following discussion.

By default, exchange is taken into account, but it hardly influences the wave profiles or eigenvalues H in the wave vector regime of interest. Nevertheless, it is favorable to calculate profiles with exchange, since it adds numerical stability by suppressing high spatial frequencies in the simulation.

The numerical model allows to take a closer look at the dynamic modes near the edge, in order to investigate the physical origins of the shift. Figure 8.7 shows the dynamic in-plane component m_x near the (right) edge of the simulation. As stated, in the bulk the wave follows a harmonic x-dependence with a defined $\mathbf{k}$-vector. Crests (troughs) of the wave correspond to the dynamic magnetization pointing to the right (left) at this snapshot in time. Dynamic magnetic volume charges $\sigma = -\nabla\mathbf{m}$ are present and govern the propagation by creating dynamic dipolar fields. The charges at the edge, which are drawn as red "$-$"-symbols, are not sufficiently compensated for as they are missing their respective counterparts. As a result, a deviation from the plane wave is observed. We interpret this modal profile as a superposition of a harmonic wave and an evanescent wave. The harmonic part can be fitted far away from the edge (red line). By subtracting this fit from the numerical data, the residual reveals the evanescent part (orange line) in the enlarged image. This mode arises to compensate for the missing dynamic charges and as a result of the charge avoidance at the interface to the non-magnetic capping material.

Finally, we evaluate the phase shift exactly as in the experiment, by fitting a 2D plane wave on the simulation grid. This is done for various values of k_x and k_y, where the values in between are interpolated linearly. Figure 8.8 **a** summarizes these numerical results. In general, the shift is closer to π for larger values of k_y. Following the argument in Ref. [91], essentially the dynamic charges along y start to get dense and compensate each other, rendering the evanescent wave unnecessary. The four solid lines correspond to the four angles that we are investigating experimentally in the following section. The dashed lines correspond to constant wave vector magnitude, shown in **b**. They allow to make predictions for beams by means of the stationary phase method. The dependence of Φ on k_y is immediately obvious. With Eq. (8.1), the small negative slope results in a small
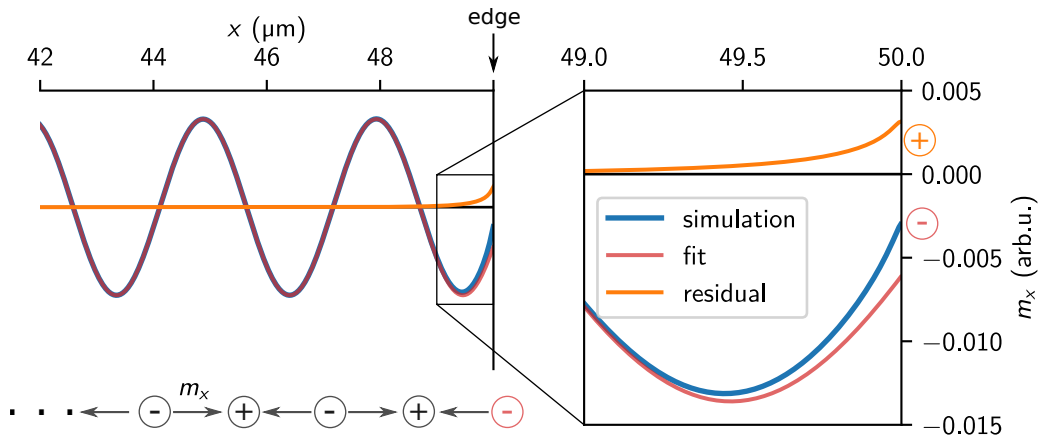
Figure 8.7: Dynamic in-plane magnetization for $k_y = 1\,\mu m^{-1}$ near the right edge of the stripe. The vector **m** points to the left (right) as indicated by the arrows below; in between, positive (negative) dynamic magnetic charges occur. The inset magnifies the region close to the edge. A plane wave is fitted far away from the edge and is shown in red. By comparing to the simulation, an evanescent wave, shown in orange, is revealed. It accounts for the uncompensated dynamic charges at the edge (red "−").
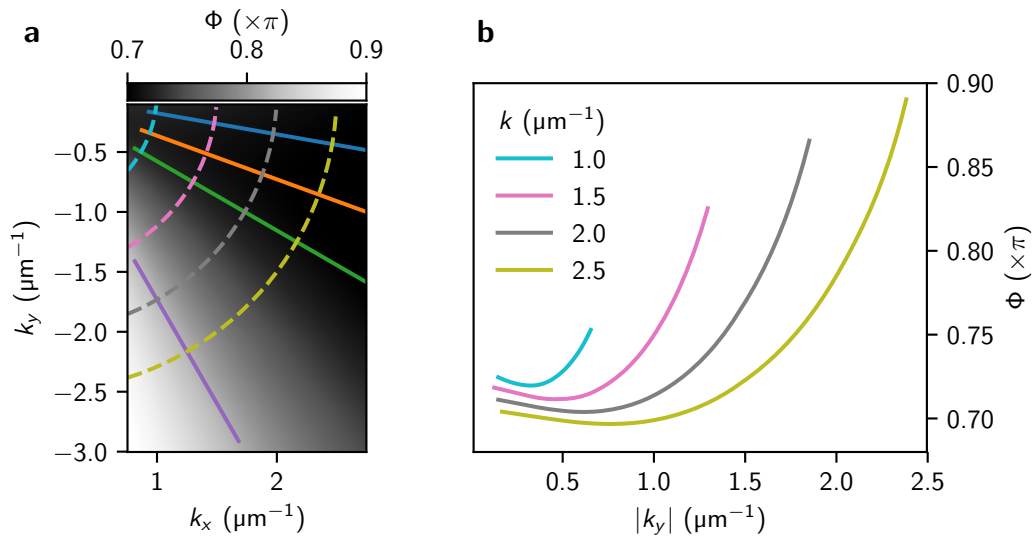
Figure 8.8: Summary of the numerical results. **a** shows the phase shift Φ as a map of wave vector components k_x and k_y. Blue, orange, green, and violet lines correspond to constant angles $\varphi = 10°$, $20°$, $30°$, and $60°$. Teal, pink, gray, and yellow lines represent a constant wave vector magnitude k. Their line cuts are shown versus k_y in **b**.
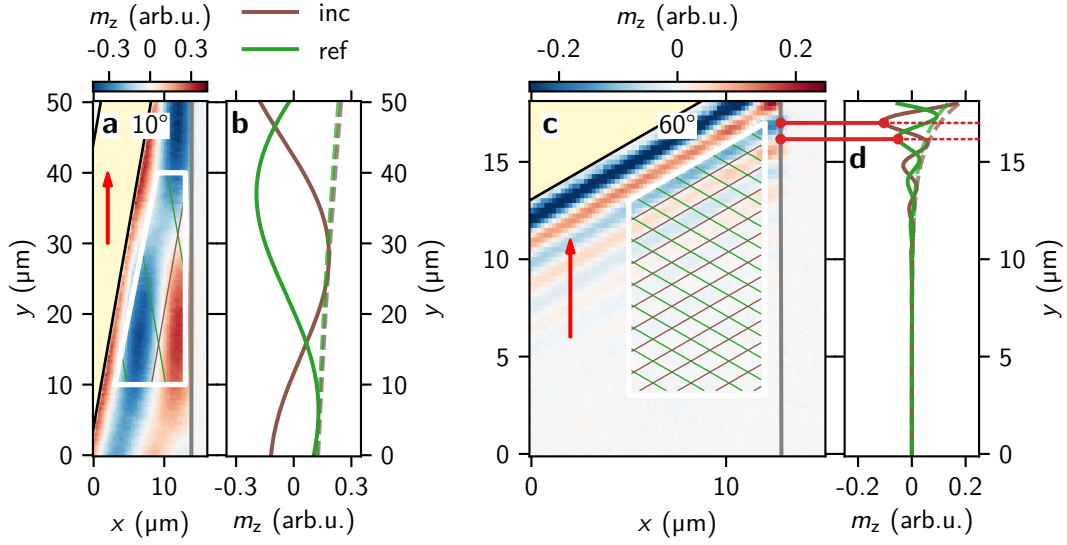
Figure 8.9: a and **c**: Typical experimental data, recorded at $\mu_0 H = 52.5\,\mathrm{mT}$ on samples with incident angle of 10° and 60°, respectively. **b** and **d**: Evaluations of the respective fits along the interface. The color code and structure of this figure is the same as in Fig. 8.3. Images on the 60° sample have a three times larger lock-in integration time to increase the signal-to-noise ratio.

positive shift in y-direction for negative k_y of the order of some tens of nanometers. For larger $|k_y|$, i.e. larger incident angles, the shift is in negative y-direction and of the order of a hundred nanometer. Hence, the observed phase shift would indeed result in a true lateral shift of spin wave beams, which depends on and can be tuned with the wave vector.

8.4 Angular Dependence of Reflection

As already shown in the previous chapters, the use of different incident angles allows to probe reflection effects for a range of wave vector components. Additionally, it allows independent measurements that confirm a dependence of the phase shift on the wave vector and not on the external field. The corresponding experimental data for $\varphi = 10°$ and $\varphi = 60°$ are shown in Fig. 8.9 **a** and **c**, respectively. Again, **b** and **d** show the evaluation of the fit along the interface. In passing, we observe that the amplitudes of incident and reflected waves do not differ significantly for $\varphi = 10°$. For larger incident angles (see also Fig. 8.3 **a**) the difference increases substantially. This behavior was already numerically discussed in Sec. 4.1.

Figure 8.10 **a** summarizes the results on Φ obtained on the four samples and with different fields plotted versus the component along the interface. In **b**, the region for $0 < k_y < 1\,\mu\mathrm{m}^{-1}$ is magnified in order to better visualize the dependence for smaller angles. The lines are the numerically obtained shifts from Sec. 8.3. Within the error, they agree well with the experiment. Note, that the error bars include an uncertainty connected to the position of the edge. For instance, a shift of the edge position of about 90 nm — far below the optical resolution of the microscope — would be enough to sufficiently account
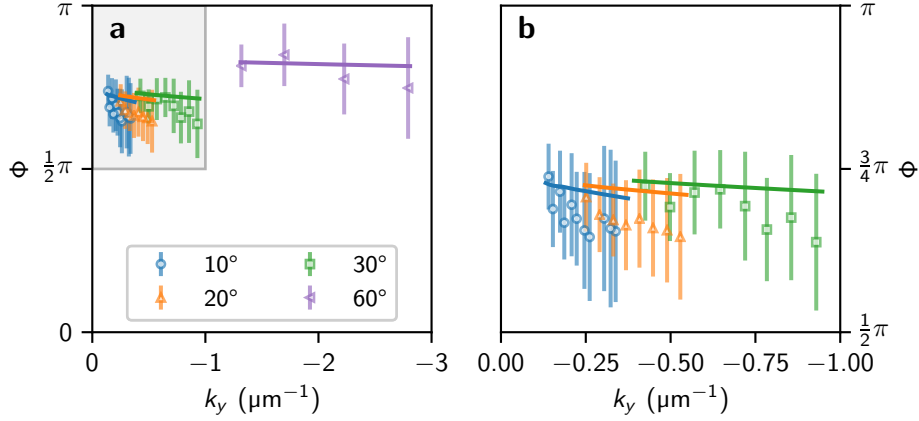
Figure 8.10: Summary of the results on the phase shift for all samples and fields. Every point corresponds to an image similar to the ones in Fig. 8.9. The external field is along $+y$. The solid lines are the numerical calculations presented in Fig. 8.8 with the same color code. **b** magnifies the gray rectangle in **a**.

for the systematic error of the $\varphi = 20°$ sample. For this reason, we can also exclude a dominant contribution of other pinning mechanisms like surface anisotropies. Besides, the latter should not contribute significantly, since the exchange energy is negligible compared to the dipolar energy in our wave vector regime. We therefore conclude that dipolar interactions cause the GH-like phase shift that we observe in our experiments.

At the end of this chapter, we want to shortly comment on the possibility of a phase shift for refracted waves motivated by Ref. [139], where a shift of a refracted spin wave beam is found at the interface between two ferromagnets. The experimental results presented in Chapter 7 have therefore been reevaluated. Within the error, we could not detect a phase shift between incoming and transmitted wave for any thickness ratio or angle of incidence.

In conclusion, we have studied the field and angular dependence of the reflection process of a plane wave at an edge of a Py film. We observe a phase shift between the waves, which exhibits a non-trivial dependence on the wave vector component along the interface. A numerical model reveals an evanescent wave, which arises due to dynamic magnetic charge avoidance at the Py edge. It also allows us to predict a GH shift for spin wave beams in this geometry. This shift might either be in negative or positive direction, depending on the angle of incidence and the wave vector. With the experiments presented here, we add a representative of GH-like shifts to the ones previously predicted for spin waves [140, 32, 33, 34, 139, 35] and provide a universal route to discover similar effects with the help of plane waves.

9 Summary

In this thesis, wave effects associated with the refraction and reflection of plane, dipolar spin waves are investigated. All measurements are conducted with time-resolved scanning Kerr microscopy. This magneto-optical technique allows for imaging of phase-resolved magnetization dynamics in real space, thereby providing a direct access to wave characteristics: By fitting their interference pattern, wave vector, phase, and attenuation length can be quantified.

The anisotropic dispersion relation in the dipolar regime depends on the thickness of a ferromagnetic film. Therefore, a thickness step acts as a boundary between two media of different indices of refraction. In two related experiments, the refraction and reflection of spin waves at the interface between a thick $Ni_{80}Fe_{20}$ (Py) film and a thin Py film are investigated. In addition, the reflection of spin waves from an edge of a Py film is studied. In all experiments, spin waves are excited by means of a coplanar wave guide in a 60 nm Py film. Their dispersion is tuned by direction and magnitude of the external field.

The first experiment emphasizes the angular dependence of refraction. We are able to analytically state and experimentally confirm Snell's law for spin waves. In contrast to optics, the index of refraction considerably depends on the angle of propagation of the incident wave. As a result, with larger incident angles, a non-linear increase in wave vector magnitude and a decrease of the angle of refraction with respect to the interface normal is observed. As a side effect, spin wave bending, i.e. non-constant wave fronts near the interface, is investigated. The refraction process is efficient, since the amplitude of spin waves after the step is about 1.6 times larger than in the thick film.

In a second series of experiments, this is further explored by studying different thicknesses of the thin film. The large transmission coefficient does not persist for lower thicknesses and decreases linearly to about 0.6 for a film thickness of 10 nm. Still, these steps are attractive as wave vector converters, since the ratio of wavelengths of refracted and incident wave follows the ratio of film thicknesses and can therefore be easily tuned.

In a third experiment, we focus on spin wave reflection at the edge of a Py film. In particular, we find a phase shift between incoming and reflected plane waves, which shows a non-trivial dependence on the wave vector component along the interface. A numerical model, based on the dynamic matrix approach, reveals that dipolar interactions are responsible for this phase shift and also cause an evanescent magnetization wave inside the Py film. With the help of the stationary phase method, the model further allows us to predict a Goos-Hänchen shift for spin wave beams. This shift can be up to about 100 nm large and might be either negative or positive, depending on the incident angle of the spin wave beam.

All three experiments provide valuable insight into the refraction and reflection of spin waves. Especially the study of refraction is interesting in the context of magnonics, where concepts to efficiently reduce wavelengths and steer spin waves are actively searched for. Besides these technological aspects, Snell's law and the Goos-Hänchen shift are fundamental wave effects which appear in various contexts throughout physics.

Appendix

A Discretization of Boundary Conditions

We closely follow the steps in Ref. [103] to obtain discretized boundary conditions like the ones in Sec. 3.2. The following procedure is formulated for the bottom boundary but an analogous one can be used for the top boundary. We denote the cells at the bottom with indices 1, 2, 3 and respective magnetization components $m^{(1)}$, $m^{(2)}$, and $m^{(3)}$. At the interface between cell 1 and 2, we introduce an index 1.5 and at the real boundary — half a cellsize to the bottom of cell 1 — we equip the position with index b. There, the boundary conditions, Eq. (3.4) are effective.

As a first step, an expression for one magnetization component at position 1.5 is found by tayloring the expression of the magnetization in cell 2 at position $-0.5d_w$:

$$m^{(1.5)} = m^{(2)} + \frac{m^{(3)} - m^{(1)}}{2d_w}\left(-\frac{d_w}{2}\right) + \frac{1}{2}\frac{m^{(3)} + m^{(1)} - 2m^{(2)}}{d_w^2}\left(-\frac{d_w}{2}\right)^2. \tag{A.1}$$

Second, an expression for $\frac{\partial m^{(b)}}{\partial w}$ is derived by tayloring the derivative in cell 1 at position $-0.5d_w$:

$$\frac{\partial m^{(b)}}{\partial w} = \frac{m^{(1.5)} - m^{(b)}}{d_w} + 4\frac{m^{(b)} + m^{(1.5)} - 2m^{(1)}}{d_w^2}\left(-\frac{d_w}{2}\right).$$

Both expressions are then put into the real boundary conditions, e.g.

$$\frac{\partial m_x^{(b)}}{\partial w} - dm_x^{(b)} = 0$$

for the component m_x with $d = d_{\text{pin}}^{(0)}\sin^2(\theta)$, and solved for $m^{(b)}$. For the second dynamic component m_z, the procedure can be applied accordingly. Then,

$$m^{(b)} = \frac{29m^1 - 6m^2 + m^3}{8d_w d + 24} \tag{A.2}$$

and finally an expression for the second derivative, which appears in the expression of the exchange operator in cell 1, can be found to

$$\frac{\partial^2 m^{(1)}}{\partial w^2} = 4\frac{m^{(b)} + m^{(1.5)} - 2m^{(1)}}{d_w^2} .$$

The identities Eqs. (A.1) and (A.2) can be plugged in the latter equality, which yields Eq. (3.6), where the boundary conditions are correctly absorbed in the exchange operator. The result depends only on $m^{(1)}$, $m^{(2)}$, and $m^{(3)}$ and can therefore be directly utilized in the matrix $\mathbf{D}$.

B Implementation of the Dynamic Matrix Method

In this chapter, some sample codes are given to build the dynamic matrix $\mathbf{D}$ and solve it for its eigenvalues as described in Secs. 3.2. The necessary packages in python can be loaded via

```python
1  import numpy as np
2  import scipy.optimize
```

B.1 Full Film

In the case of a full film, first the equilibrium position and internal field, i.e. H and θ have to be found for a given H_{ext} and θ_H. For this reason, a function `equ()` can be defined that is numerically solved for the latter via `fsolve()`:

```python
1  def equ(p,Hext,thetaH,Ms):
2      H,theta = p
3      e1 = Hext*np.cos(theta-thetaH)-Ms*np.sin(theta)**2-H
4      e2 = Hext*np.sin(theta-thetaH) + Ms * np.sin(theta)*np.cos(theta)
5      return e1,e2
6
7  H,theta = optimize.fsolve(equ,[1,0],args=(He,thetaH,Ms))
```

The contributions to $\mathbf{D}$ are separated into `D_demag`, `D_zeeman` and `D_exc` (shown in Listings B.1 – B.3, respectively) according to their interaction. First, these $2N \times 2N$ arrays are initialized and afterwards filled via for-loops.

Listing B.1: Calculation of the demag interaction. `R` and a `RT` correspond to the rotational matrix and its transposed defined in Eq. (2.22), respectively. `G_self` and `G_mut` are defined as the negative of the demag tensors in Eqs. (3.1) and (2.35). `dw` is the cell thickness and `wm` is defined as $\mu_0\gamma M_S$.

```python
1  D_demag = np.zeros([2*N,2*N],dtype = complex)
2
3  for i in range(N):
4      for j in range(N):
5          if i-j == 0: # self-demagnetizing
6              nvv_self = 1-(1-np.exp(-abs(k)*dw))/abs(k)/dw
7
8              G_self = np.array([[0,0,0],[0,nvv_self,0],[0,0,1-nvv_self]])
9              Gxyz_self = np.dot(np.dot(R,G_self),RT)
10             Gxx = Gxyz_self[0,0]
11             Gxz = Gxyz_self[0,2]
12             Gzx = Gxyz_self[2,0]
13             Gzz = Gxyz_self[2,2]
```

```
14
15                    D_demag[2*i,2*j] = -Gzx #contributes to hz # sign change bc h=\
                          -G*m
16                    D_demag[2*i+1,2*j] = Gxx #contributes to hx
17                    D_demag[2*i,2*j+1] = -Gzz #contributes to hz
18                    D_demag[2*i+1,2*j+1] = Gxz #contributes to hx
19
20              else:
21                    nvv_mut = 2*np.sinh(k*dw/2)**2/abs(k)/dw*np.exp(-abs(k*(i-j)*\
                          dw))
22                    G_mut = np.array([[0,0,0],[0,nvv_mut,-1j*np.sign(i-j)*np.sign(\
                          k)*nvv_mut],[0,-1j*np.sign(i-j)*np.sign(k)*nvv_mut,-\
                          nvv_mut]])
23                    Gxyz_mut = np.dot(np.dot(R,G_mut),RT)
24                    Gxx = Gxyz_mut[0,0]
25                    Gxz = Gxyz_mut[0,2]
26                    Gzx = Gxyz_mut[2,0]
27                    Gzz = Gxyz_mut[2,2]
28                    D_demag[2*i,2*j] = -Gzx #contributes to hz
29                    D_demag[2*i+1,2*j] = Gxx #contributes to hx
30                    D_demag[2*i,2*j+1] = -Gzz #contributes to hz
31                    D_demag[2*i+1,2*j+1] = Gxz #contributes to hx
32
33  D_demag *= wm
```

Listing B.2: Calculation of the Zeeman interaction. wh is defined as $\mu_0\gamma H$.

```
1  D_zeeman = np.zeros([2*N,2*N])
2
3  for i in range(N):
4      j = i                              #zeeman acts locally
5      D_zeeman[2*i,2*j+1] = -wh
6      D_zeeman[2*i+1,2*j] = wh
```

Listing B.3: Calculation of the exchange interaction with different pinning paramters at top (dtop) and bottom (dbot). The exchange boundary conditions are discretized according to Chapter A. lex is the exchange length defined in Eq. (2.6).

```
1  D_exc = np.zeros([2*N,2*N],dtype = complex)
2
3  dx_top = dtop * np.sin(theta)**2
4  dx_bot = dbot * np.sin(theta)**2
5
6  dz_top = dtop * np.cos(2*theta)
7  dz_bot = dbot * np.cos(2*theta)
8
9  for i in range(N):                     #exchange fields:
10     j = i
11
12     if i==0:                           #bot boundary
13         D_exc[2*i,2*j+1] += 1/(2*(dz_bot*dw - 3))*(-13*dz_bot*dw+10) #hz
14         D_exc[2*i+1,2*j] -=  1/(2*(dx_bot*dw + 3))*(-13*dx_bot*dw-10) #hx
15
16         D_exc[2*i,2*(j+1)+1] += 1/(2*(dz_bot*dw - 3))*(6*dz_bot*dw-12)
```

```
17            D_exc[2*i+1,2*(j+1)] -= 1/(2*(dx_bot*dw + 3))*(6*dx_bot *dw+12)
18
19            D_exc[2*i,2*(j+2)+1] += 1/(2*(dz_bot*dw - 3))*(-dz_bot*dw+2)
20            D_exc[2*i+1,2*(j+2)] -= 1/(2*(dx_bot*dw + 3))*(-dx_bot *dw-2)
21
22      else:                                    #top boundary
23          if i==N-1:
24              D_exc[2*i,2*j+1] += 1/(2*(dz_top*dw - 3))*(-13*dz_top*dw+10) #\
                    hz
25              D_exc[2*i+1,2*j] -=  1/(2*(dx_top*dw + 3))*(-13*dx_top*dw-10) \
                    #hx
26
27              D_exc[2*i,2*(j-1)+1] += 1/(2*(dz_top*dw - 3))*(6*dz_top*dw-12)
28              D_exc[2*i+1,2*(j-1)] -= 1/(2*(dx_top*dw + 3))*(6*dx_top*dw+12)
29
30              D_exc[2*i,2*(j-2)+1] += 1/(2*(dz_top*dw - 3))*(-dz_top*dw+2)
31              D_exc[2*i+1,2*(j-2)] -= 1/(2*(dx_top*dw + 3))*(-dx_top*dw-2)
32
33          else:                                #in the middle
34              D_exc[2*i,2*j+1] += -2 #hz
35              D_exc[2*i+1,2*j] -= -2 #hx
36              D_exc[2*i,2*(j+1)+1] += 1
37              D_exc[2*i+1,2*(j+1)] -= 1
38              D_exc[2*i,2*(j-1)+1] += 1
39              D_exc[2*i+1,2*(j-1)] -= 1
40
41      D_exc[2*i,2*j+1] += -k**2*dw**2 #hz dw gets canceled below
42      D_exc[2*i+1,2*j] += k**2*dw**2 #hx
43
44 D_exc = lex**2/dw**2*wm * D_exc
```

Finally, the contributions are added up and the matrix is numerically solved via the `linalg.eig()` method to receive eigenvalues `w` and eigenvectors `v`:

```
1 D = 1j*(D_zeeman+D_demag+D_exc)
2 w, v = np.linalg.eig(D)
```

Due to the structure of D, the dynamic component $m_{x,0}$ can be recovered as `v[::2]` (every second entry) and $m_{z,0}$ as `v[1::2]` (every second entry starting from the second) for a particular ω (`w`).

B.2 Stripe

The structure of $\mathbf{D}$ in a stripe is similar to the one for the full film. They differ mainly in the arrangement of different field contributions, such that the previous section can be used as a basic recipe. Since dynamic demagnetizing factors n_{xx} and n_{zz} cannot be calculated analytically anymore, they are numerically integrated. As detailed in [91], self interaction and interactions with neighboring cells might exhibit (integrable) singularities and therefore a Monte Carlo method, i.e. the vegas algorithm provided through the vegas python package [105], yields good results. The integration converged with an acceptable error in the range of 10^{-6} for 10 iterations of the algorithm, each sampling the integrand

10^7 times. For demagnetizing interactions further than one cell apart, the faster method `nquad()` provided by the `scipy.integrate` module was used.
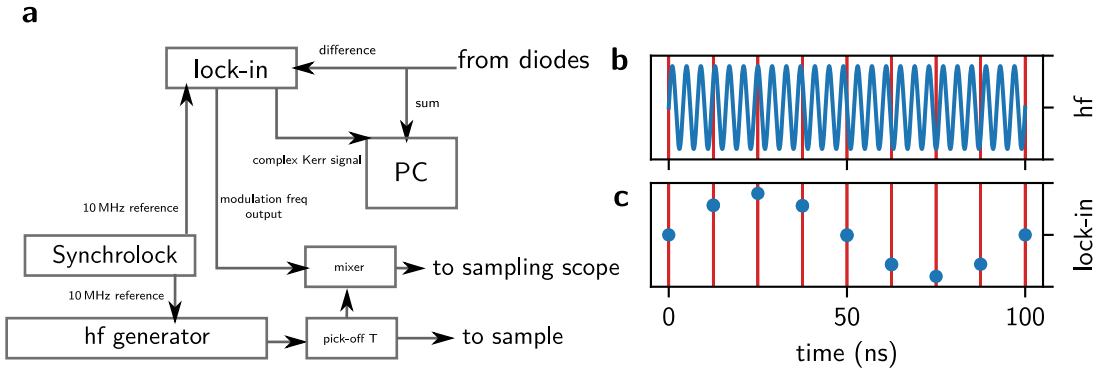
C Undersampling

When a time harmonic signal with frequency f gets sampled at a constant frequency $f_{\mathrm{rep}} < f$, there appear aliases at lower frequencies. Especially, when $f = \nu f_{\mathrm{rep}} + f_{\mathrm{mod}}$ with an integer ν, there will be aliases at integer multiples of f_{mod}.

In particular, a precessing magnetization at frequency $f \neq \nu f_{\mathrm{rep}}$, which is detected by laser pulses with a repetition rate $f_{\mathrm{rep}} = 80\,\mathrm{MHz}$ will cause an alias at $f_{\mathrm{mod}} < 80\,\mathrm{MHz}$. This alias enables a reconstruction of the signal. A lock-in amplifier can be used to lock to f_{mod} and determine its phase and amplitude, which essentially allow for a detection of phase and amplitude of the precessing magnetization as θ and R channel of the lock-in without a need of a phase shifter or active modulation as in setup described in Sec. 3.3. In addition, it permits almost arbitrary frequency steps as opposed to the limitation $f = \nu f_{\mathrm{rep}}$. In Ref. [109], this technique was dubbed *super Nyquist sampling*.

The components necessary are depicted in Fig. C.1 **a**. The time-domain representation of the sampling is depicted in **b**: A signal (in blue) is sampled with a repetition rate of 80 MHz (red vertical lines). As a result, an alias at much lower frequency will be recognized by the detector and fed to the lock-in. Since the sampling scope cannot be utilized for phase stabilization as described in Sec. 3.3, f is mixed with f_{mod} to get a signal that is a multiple of f_{rep} and whose phase can be displayed by the oscilloscope. If this phase drifts in time, it can be added to the phase θ determined by the lock-in.

Figure C.1: Undersampling technique. **a** shows the components necessary. **b** and **c** show the signal expected at the sample and the sampled signal, respectively. The time scale is chosen such that one period of the harmonic alias with frequency f_{mod} is visible in **c**. The lock-in needs to lock to this frequency to retain the signal. See Figs. 3.9 and 3.10 for comparison to the techniques used for the experiments in this thesis.

Unfortunately, the phase stabilization was not stable enough to considerably extend the measurement time beyond 1 minute. This corresponds to the time where the output of the hf generator can be considered phase-stable with respect to the reference of the synchrolock (i.e. the laser pulses). This is probably due to the mixing of the output of the lock-in with the high frequency signal, which might not be phase conserving. Of course, this only applies to the correct determination of θ — the R channel should be unaffected by the phase. This would prevent a detection of spin waves, but is certainly a possibility for local ferromagnetic resonance measurements, where usually only the resonance position and not its phase is important.

Lock-in and photodiodes need to have a bandwidth of preferably $0.5f_{\mathrm{rep}}$. This guarantees access to the whole frequency spectrum f, since there is always an alias in the frequency interval $-0.5f_{\mathrm{rep}} < 0.5f_{\mathrm{rep}}$. The respective components were integrated into the current setup. To make the undersampling technique competitive for longer measurements, the hf generator, laser pulses, and the lock-in need to have a constant phase relation. In the author's opinion, the missing piece to solve this problem is a hf generator with a stable phase relation with respect to its reference input, such that an active phase stabilization is superfluous. First measurements showed that such a setup would provide a considerable boost in signal-to-noise ratio and therefore decreased measurement times. Additionally, in contrast to standard TRMOKE experiments, it allows to measure with very high frequency resolution. In situations where the experiment demands a fixed external field, e.g. at skyrmion resonances, this may be in particular useful.

Bibliography

[1] A. V. Chumak, V. I. Vasyuchka, A. A. Serga, and B. Hillebrands, "Magnon spin-tronics," Nat. Phys. **11**, 453 (2015).

[2] H. Yu, O. d Allivy Kelly, V. Cros, R. Bernard, P. Bortolotti, A. Anane, F. Brandl, F. Heimbach, and D. Grundler, "Approaching soft x-ray wavelengths in nanomagnet-based microwave technology," Nat. Commun. **7**, 11255 (2016).

[3] T. Kampfrath, A. Sell, G. Klatt, A. Pashkin, S. Mährlein, T. Dekorsy, M. Wolf, M. Fiebig, A. Leitenstorfer, and R. Huber, "Coherent terahertz control of antifer-romagnetic spin waves," Nat. Photonics **5**, 31 (2010).

[4] A. V. Chumak, A. A. Serga, and B. Hillebrands, "Magnon transistor for all-magnon data processing," Nat. Commun. **5**, 4700 (2014).

[5] S. Neusser and D. Grundler, "Magnonics: Spin waves on the nanoscale," Adv. Mater. **21**, 2927 (2009).

[6] V. V. Kruglyak, S. O. Demokritov, and D. Grundler, "Magnonics," J. Phys. D: Appl. Phys. **43**, 264001 (2010).

[7] B. Lenk, H. Ulrichs, F. Garbs, and M. Münzenberg, "The building blocks of magnon-ics," Phys. Rep. **507**, 107 (2011).

[8] S. A. Nikitov, D. V. Kalyabin, I. V. Lisenkov, A. Slavin, Y. N. Barabanenkov, S. A. Osokin, A. V. Sadovnikov, E. N. Beginin, M. A. Morozova, Y. A. Filimonov, Y. V. Khivintsev, S. L. Vysotsky, V. K. Sakharov, and E. S. Pavlov, "Magnonics: a new research area in spintronics and spin wave electronics," Phys. Usp. **58**, 1002 (2015).

[9] M. Krawczyk and D. Grundler, "Review and prospects of magnonic crystals and devices with reprogrammable band structure," J. Phys.: Condens. Matter **26**, 123202 (2014).

[10] S. O. Demokritov, V. E. Demidov, O. Dzyapko, G. A. Melkov, A. A. Serga, B. Hille-brands, and A. N. Slavin, "Bose-Einstein condensation of quasi-equilibrium magnons at room temperature under pumping," Nature **443**, 430 (2006).

[11] S. O. Demokritov, A. A. Serga, A. André, V. E. Demidov, M. P. Kostylev, B. Hille-brands, and A. N. Slavin, "Tunneling of dipolar spin waves through a region of inhomogeneous magnetic field," Phys. Rev. Lett. **93**, 047201 (2004).

[12] F. Ma, Y. Zhou, H. B. Braun, and W. S. Lew, "Skyrmion-based dynamic magnonic crystal," Nano Lett. **15**, 4029 (2015).

[13] M. Weiler, A. Aqeel, M. Mostovoy, A. Leonov, S. Geprägs, R. Gross, H. Huebl, T. T. M. Palstra, and S. T. B. Goennenwein, "Helimagnon resonances in an intrinsic chiral magnonic crystal," Phys. Rev. Lett. **119**, 237204 (2017).

[14] D. R. Birt, B. O'Gorman, M. Tsoi, X. Li, V. E. Demidov, and S. O. Demokritov, "Diffraction of spin waves from a submicrometer-size defect in a microwaveguide," Appl. Phys. Lett. **95**, 122510 (2009).

[15] S. Mansfeld, J. Topp, K. Martens, J. N. Toedt, W. Hansen, D. Heitmann, and S. Mendach, "Spin wave diffraction and perfect imaging of a grating," Phys. Rev. Lett. **108**, 047204 (2012).

[16] K. Perzlmaier, G. Woltersdorf, and C. H. Back, "Observation of the propagation and interference of spin waves in ferromagnetic thin films," Phys. Rev. B **77**, 054425 (2008).

[17] M. Bauer, C. Mathieu, S. O. Demokritov, B. Hillebrands, P. A. Kolodin, S. Sure, H. Dötsch, V. Grimalsky, Y. Rapoport, and A. N. Slavin, "Direct observation of two-dimensional self-focusing of spin waves in magnetic films," Phys. Rev. B **56**, R8483 (1997).

[18] J.-V. Kim, R. L. Stamps, and R. E. Camley, "Spin wave power flow and caustics in ultrathin ferromagnets with the Dzyaloshinskii-Moriya interaction," Phys. Rev. Lett. **117**, 197204 (2016).

[19] V. Vlaminck and M. Bailleul, "Current-induced spin-wave Doppler shift," Science **322**, 410 (2008).

[20] J.-Y. Chauleau, H. G. Bauer, H. S. Körner, J. Stigloher, M. Härtinger, G. Woltersdorf, and C. H. Back, "Self-consistent determination of the key spin-transfer torque parameters from spin-wave Doppler experiments," Phys. Rev. B **89**, 020403 (2014).

[21] B. A. Kalinikos and A. N. Slavin, "Theory of dipole-exchange spin wave spectrum for ferromagnetic films with mixed exchange boundary conditions," J. Phys. C: Sol. St. Phys. **19**, 7013 (1986).

[22] L. Berger, "Emission of spin waves by a magnetic multilayer traversed by a current," Phys. Rev. B **54**, 9353 (1996).

[23] J. Stigloher, M. Decker, H. S. Körner, K. Tanabe, T. Moriyama, T. Taniguchi, H. Hata, M. Madami, G. Gubbiotti, K. Kobayashi, T. Ono, and C. H. Back, "Snell's law for spin waves," Phys. Rev. Lett. **117**, 037204 (2016).

[24] J. Stigloher, T. Taniguchi, M. Madami, M. Decker, H. S. Körner, T. Moriyama, G. Gubbiotti, T. Ono, and C. H. Back, "Spin-wave wavelength down-conversion at thickness steps," Appl. Phys Express **11**, 053002 (2018).

[25] V. E. Demidov, M. P. Kostylev, K. Rott, J. Münchenberger, G. Reiss, and S. O. Demokritov, "Excitation of short-wavelength spin waves in magnonic waveguides," Appl. Phys. Lett. **99** (2011).

[26] H. Yu, G. Duerr, R. Huber, M. Bahr, T. Schwarze, F. Brandl, and D. Grundler, "Omnidirectional spin-wave nanograting coupler," Nat. Commun. **4**, 2702 (2013).

[27] K. Vogt, F. Fradin, J. Pearson, T. Sebastian, S. Bader, B. Hillebrands, A. Hoffmann, and H. Schultheiss, "Realization of a spin-wave multiplexer," Nat. Commun. **5**, 3727 (2014).

[28] A. Haldar, D. Kumar, and A. O. Adeyeye, "A reconfigurable waveguide for energy-efficient transmission and local manipulation of information in a nanomagnetic device," Nat. Nano , 332 (2016).

[29] K. Wagner, A. Kákay, K. Schultheiss, A. Henschke, T. Sebastian, and H. Schultheiss, "Magnetic domain walls as reconfigurable spin-wave nanochannels," Nat. Nano , 339 (2016).

[30] K. Artmann, "Berechnung der Seitenversetzung des totalreflektierten Strahles," Ann. Phys. **437**, 87 (1948).

[31] F. Goos and H. Hänchen, "Ein neuer und fundamentaler Versuch zur Totalreflexion," Ann. Phys. **436**, 333 (1947).

[32] Y. S. Dadoenkova, N. N. Dadoenkova, I. L. Lyubchanskii, M. L. Sokolovskyy, J. W. Klos, J. Romero-Vivas, and M. Krawczyk, "Huge Goos-Hänchen effect for spin waves: A promising tool for study magnetic properties at interfaces," Appl. Phys. Lett. **101**, 042404 (2012).

[33] P. Gruszecki, J. Romero-Vivas, Y. S. Dadoenkova, N. N. Dadoenkova, I. L. Lyubchanskii, and M. Krawczyk, "Goos-Hänchen effect and bending of spin wave beams in thin magnetic films," Appl. Phys. Lett. **105**, 242406 (2014).

[34] P. Gruszecki, Y. S. Dadoenkova, N. N. Dadoenkova, I. L. Lyubchanskii, J. Romero-Vivas, K. Y. Guslienko, and M. Krawczyk, "Influence of magnetic surface anisotropy on spin wave reflection from the edge of ferromagnetic film," Phys. Rev. B **92**, 054427 (2015).

[35] A. Okamoto and S. Murakami, "Berry curvature for magnons in ferromagnetic films with dipole-exchange interactions," Phys. Rev. B **96**, 174437 (2017).

[36] J. Stigloher, T. Taniguchi, H. S. Körner, M. Decker, T. Moriyama, T. Ono, and C. H. Back, "Observation of a Goos-Hänchen-like phase shift for magnetostatic spin waves," Phys. Rev. Lett. **121**, 137201 (2018).

[37] J. H. E. Griffiths, "Anomalous high-frequency resistance of ferromagnetic metals," Nature **158**, 670 (1946).

[38] C. Kittel, "On the theory of ferromagnetic resonance absorption," Phys. Rev. **73**, 155 (1948).

[39] F. Bloch, "Zur Theorie des Ferromagnetismus," Zeitschrift für Physik **61**, 206 (1930).

[40] T. Holstein and H. Primakoff, "Field dependence of the intrinsic domain magnetization of a ferromagnet," Phys. Rev. **58**, 1098 (1940).

[41] L. D. Landau and E. Lifshitz, "On the theory of the dispersion of magnetic permeability in ferromagnetic bodies," Phys. Z. Sowjetunion **8**, 101 (1935).

[42] W. Brown, *Magnetostatic principles in ferromagnetism*, Selected topics in solid state physics (North-Holland Publishing Company, 1962).

[43] L. R. Walker, "Magnetostatic modes in ferromagnetic resonance," Phys. Rev. **105**, 390 (1957).

[44] J. R. Eshbach and R. W. Damon, "Surface magnetostatic modes and surface spin waves," Phys. Rev. **118**, 1208 (1960).

[45] R. Damon and J. Eshbach, "Magnetostatic modes of a ferromagnet slab," J. Phys. Chem. Solids **19**, 308 (1961).

[46] G. Rado and J. Weertman, "Spin-wave resonance in a ferromagnetic metal," J. Phys. Chem. Solids **11**, 315 (1959).

[47] R. F. Soohoo, "General exchange boundary condition and surface anisotropy energy of a ferromagnet," Phys. Rev. **131**, 594 (1963).

[48] O. G. Vendik, B. A. Kalinikos, and D. N. Chartorizhskii, "Instability of spin-waves in thin ferromagnetic films," Sov. Phys. Solid State **16**, 1785 (1975).

[49] O. G. Vendik, B. A. Kalinikos, and D. N. Chartorizhskii, "Instability of spin-waves in tangentially magnetized ferromagnetic films," Sov. Phys. Solid State **19**, 222 (1977).

[50] B. A. Kalinikos, M. P. Kostylev, N. V. Kozhus, and A. N. Slavin, "The dipole-exchange spin wave spectrum for anisotropic ferromagnetic films with mixed exchange boundary conditions," J. Phys.: Condens. Matter **2**, 9861 (1990).

[51] K. Y. Guslienko and A. N. Slavin, "Magnetostatic Green's functions for the description of spin waves in finite rectangular magnetic dots and stripes," J. Magn. Magn. Mater. **323**, 2418 (2011).

[52] M. R. Freeman and W. K. Hiebert, "Stroboscopic microscopy of magnetic dynamics," in *Spin Dynamics in Confined Magnetic Structures I*, edited by B. Hillebrands and K. Ounadjela (Springer Berlin Heidelberg, Berlin, Heidelberg, 2002) pp. 93–126.

[53] A. A. Serga, T. Schneider, B. Hillebrands, S. O. Demokritov, and M. P. Kostylev, "Phase-sensitive Brillouin light scattering spectroscopy from spin-wave packets," Appl. Phys. Lett. **89**, 063506 (2006).

[54] M. Madami, G. Gubbiotti, S. Tacchi, and G. Carlotti, "Application of microfocused Brillouin light scattering to the study of spin waves in low-dimensional magnetic systems," Sol. State Phys. **63**, 79 (2012).

[55] M. Bailleul, D. Olligs, and C. Fermon, "Propagating spin wave spectroscopy in a permalloy film: A quantitative analysis," Appl. Phys. Lett. **83**, 972 (2003).

[56] A. Gurevich and G. Melkov, *Magnetization oscillations and waves* (Taylor & Francis, 1996).

[57] B. Hillebrands and K. Ounadjela, eds., *Spin dynamics in confined magnetic structures I* (Springer-Verlag Berlin Heidelberg New York, 2002).

[58] G. Bertotti, I. D. Mayergoyz, and C. Serpico, "Chapter 2 - basic equations for magnetization dynamics," in *Nonlinear Magnetization Dynamics in Nanosystems*, Elsevier Series in Electromagnetism, edited by G. Bertotti, I. D. Mayergoyz, and C. Serpico (Elsevier, Oxford, 2009) pp. 21 – 34.

[59] J. D. Jackson, *Classical electrodynamics*, 3rd ed. (Wiley, New York, NY, 1999).

[60] A. J. Newell, W. Williams, and D. J. Dunlop, "A generalization of the demagnetizing tensor for nonuniform magnetization," J. Geophys. Res. Solid Earth **98**, 9551 (1993).

[61] J. A. Osborn, "Demagnetizing factors of the general ellipsoid," Phys. Rev. **67**, 351 (1945).

[62] E. Schlömann, "A sum rule concerning the inhomogeneous demagnetizing field in nonellipsoidal samples," J. Appl. Phys. **33**, 2825 (1962).

[63] R. I. Joseph and E. Schlömann, "Demagnetizing field in nonellipsoidal bodies," J. Appl. Phys. **36**, 1579 (1965).

[64] A. Aharoni, "Demagnetizing factors for rectangular ferromagnetic prisms," J. Appl. Phys. **83**, 3432 (1998).

[65] J. M. Coey, *Magnetism and magnetic materials* (Cambridge University Press, 2009).

[66] K. J. Harte, "Theory of magnetization ripple in ferromagnetic films," J. Appl. Phys. **39**, 1503 (1968).

[67] P. Kaboš and V. Stalmačov, *Magnetostatic waves and their application* (Chapman & Hall, 1994).

[68] E. H. Lock, "The properties of isofrequency dependences and the laws of geometrical optics," Phys.-Usp. **51**, 375 (2008).

[69] C. S. Davies, A. Francis, A. V. Sadovnikov, S. V. Chertopalov, M. T. Bryan, S. V. Grishin, D. A. Allwood, Y. P. Sharaevskii, S. A. Nikitov, and V. V. Kruglyak, "Towards graded-index magnonics: Steering spin waves in magnonic networks," Phys. Rev. B **92**, 020408 (2015).

[70] V. E. Demidov, S. Urazhdin, and S. O. Demokritov, "Direct observation and mapping of spin waves emitted by spin-torque nano-oscillators," Nat. Mat. **9**, 984 (2010).

[71] S. M. Mohseni, S. R. Sani, J. Persson, T. N. A. Nguyen, S. Chung, Y. Pogoryelov, P. K. Muduli, E. Iacocca, A. Eklund, R. K. Dumas, S. Bonetti, A. Deac, M. A. Hoefer, and J. Åkerman, "Spin torque–generated magnetic droplet solitons," Science **339**, 1295 (2013).

[72] S. Urazhdin, V. E. Demidov, H. Ulrichs, T. Kendziorczyk, T. Kuhn, J. Leuthold, G. Wilde, and S. O. Demokritov, "Nanomagnonic devices based on the spin-transfer torque," Nat. Nanotechnol. **9**, 509 (2014).

[73] M. Voto, L. Lopez-Diaz, and E. Martinez, "Pinned domain wall oscillator as a tuneable direct current spin wave emitter," Sci. Rep. **7**, 13559 (2017).

[74] S. Wintz, V. Tiberkevich, M. Weigand, J. Raabe, J. Lindner, A. Erbe, A. Slavin, and J. Fassbender, "Magnetic vortex cores as tunable spin-wave emitters," Nat. Nano **11**, 948 (2016).

[75] M. van Kampen, C. Jozsa, J. T. Kohlhepp, P. LeClair, L. Lagae, W. J. M. de Jonge, and B. Koopmans, "All-optical probe of coherent spin waves," Phys. Rev. Lett. **88**, 227201 (2002).

[76] Y. Hashimoto, S. Daimon, R. Iguchi, Y. Oikawa, K. Shen, K. Sato, D. Bossini, Y. Tabuchi, T. Satoh, B. Hillebrands, G. E. W. Bauer, T. H. Johansen, A. Kirilyuk, T. Rasing, and E. Saitoh, "All-optical observation and reconstruction of spin wave dispersion," Nat. Commun. **8**, 15859 (2017).

[77] M. Obstbaum, *Inverse spin Hall effect in metallic heterostructures*, Ph.D. thesis, Universität Regensburg (2016).

[78] H. S. Körner, J. Stigloher, H. G. Bauer, H. Hata, T. Taniguchi, T. Moriyama, T. Ono, and C. H. Back, "Interfacial Dzyaloshinskii-Moriya interaction studied by time-resolved scanning Kerr microscopy," Phys. Rev. B **92**, 220413 (2015).

[79] T. Schneider, A. A. Serga, T. Neumann, B. Hillebrands, and M. P. Kostylev, "Phase reciprocity of spin-wave excitation by a microstrip antenna," Phys. Rev. B **77**, 214411 (2008).

[80] H. G. Bauer, J.-Y. Chauleau, G. Woltersdorf, and C. H. Back, "Coupling of spinwave modes in wire structures," Appl. Phys. Lett. **104**, 102404 (2014).

[81] T. Brächer, M. Fabre, T. Meyer, T. Fischer, S. Auffret, O. Boulle, U. Ebels, P. Pirro, and G. Gaudin, "Detection of short-waved spin waves in individual microscopic spin-wave waveguides using the inverse spin hall effect," Nano Lett. **17**, 7234 (2017).

[82] H. Bauer, *Linear and nonlinear magnetization dynamics in thin ferromagnetic films and nanostructures*, Ph.D. thesis, Universität Regensburg (2015).

[83] A. K. Ganguly and D. C. Webb, "Microstrip excitation of magnetostatic surface waves: Theory and experiment," IEEE Trans. Microwave Theory Tech. **23**, 998 (1975).

[84] E. Schlömann, "Generation of spin waves in nonuniform magnetic fields. I. conversion of electromagnetic power into spin-wave power and vice versa," J. Appl. Phys. **35**, 159 (1964).

[85] F. B. Mushenok, R. Dost, C. S. Davies, D. A. Allwood, B. J. Inkson, G. Hrkac, and V. V. Kruglyak, "Broadband conversion of microwaves into propagating spin waves in patterned magnetic structures," Appl. Phys. Lett. **111**, 042404 (2017).

[86] G. Csaba, Ádám Papp, and W. Porod, "Perspectives of using spin waves for computing and signal processing," Phys. Lett. A **381**, 1471 (2017).

[87] A. Papp, W. Porod, A. I. Csurgay, and G. Csaba, "Nanoscale spectrum analyzer based on spin-wave interference," Sci. Rep. **7**, 9245 (2017).

[88] M. Donahue and D. Porter, "Oommf user's guide, version 1.0," Interagency Report NISTIR 6376, National Institute of Standards and Technology, Gaithersburg, MD (1999).

[89] T. Fischbacher, M. Franchin, G. Bordignon, and H. Fangohr, "A systematic approach to multiphysics extensions of finite-element-based micromagnetic simulations: Nmag," IEEE Trans. Magn. **43**, 2896 (2007).

[90] A. Vansteenkiste, J. Leliaert, M. Dvornik, M. Helsen, F. Garcia-Sanchez, and B. Van Waeyenberge, "The design and verification of mumax3," AIP Adv. **4**, 107133 (2014).

[91] Y. Henry, O. Gladii, and M. Bailleul, "Propagating spin-wave normal modes: A dynamic matrix approach using plane-wave demagnetizating tensors," ArXiv e-prints (2016), 1611.06153 .

[92] M. Grimsditch, L. Giovannini, F. Montoncello, F. Nizzoli, G. K. Leaf, and H. G. Kaper, "Magnetic normal modes in ferromagnetic nanoparticles: A dynamical matrix approach," Phys. Rev. B **70**, 054409 (2004).

[93] F. Montoncello, L. Giovannini, F. Nizzoli, P. Vavassori, M. Grimsditch, T. Ono, G. Gubbiotti, S. Tacchi, and G. Carlotti, "Soft spin waves and magnetization reversal in elliptical permalloy nanodots: Experiments and dynamical matrix results," Phys. Rev. B **76**, 024426 (2007).

[94] W. H. Press, S. A. Teukolsky, W. T. Vetterling, and B. P. Flannery, *Numerical recipes 3rd edition: the art of scientific computing*, 3rd ed. (Cambridge University Press, 2007).

[95] W. Sun, K. Liu, and C. A. Balanis, "Analysis of singly and doubly periodic absorbers by frequency-domain finite-difference method," IEEE Transactions on Antennas and Propagation **44**, 798 (1996).

[96] M. G. Cottam, *Linear and nonlinear spin waves in magnetic films and superlattices* (World Scientific, 1994).

[97] M. Kostylev, "Non-reciprocity of dipole-exchange spin waves in thin ferromagnetic films," J. Appl. Phys. **113**, 053907 (2013).

[98] M. Haidar, M. Bailleul, M. Kostylev, and Y. Lao, "Nonreciprocal Oersted field contribution to the current-induced frequency shift of magnetostatic surface waves," Phys. Rev. B **89**, 094426 (2014).

[99] O. Gladii, *Spin wave propagation and its modification by an electrical current in Py/Al2O3, Py/Pt and Fe/MgO films*, Ph.D. thesis, Université de Strasbourg (2016).

[100] M. Donahue and D. Porter, "Exchange energy formulations for 3d micromagnetics," Physica B **343**, 177 (2004).

[101] K. Y. Guslienko, S. O. Demokritov, B. Hillebrands, and A. N. Slavin, "Effective dipolar boundary conditions for dynamic magnetization in thin magnetic stripes," Phys. Rev. B **66**, 132402 (2002).

[102] K. Y. Guslienko and A. N. Slavin, "Boundary conditions for magnetization in magnetic nanoelements," Phys. Rev. B **72**, 014463 (2005).

[103] M. Kostylev, "Strong asymmetry of microwave absorption by bilayer conducting ferromagnetic films in the microstrip-line based broadband ferromagnetic resonance," J. Appl. Phys. **106**, 043903 (2009).

[104] G. P. Lepage, "A new algorithm for adaptive multidimensional integration," J. Comput. Phys. **27**, 192 (1978).

[105] G. P. Lepage, "vegas: Adaptive multidimensional Monte Carlo integration," (2013–), https://github.com/gplepage/vegas; accessed October 8, 2018.

[106] J. P. Park, P. Eames, D. M. Engebretson, J. Berezovsky, and P. A. Crowell, "Spatially resolved dynamics of localized spin-wave modes in ferromagnetic wires," Phys. Rev. Lett. **89**, 277201 (2002).

[107] Z. Liu, F. Giesen, X. Zhu, R. D. Sydora, and M. R. Freeman, "Spin wave dynamics and the determination of intrinsic damping in locally excited permalloy thin films," Phys. Rev. Lett. **98**, 087201 (2007).

[108] G. Woltersdorf, J. Stigloher, H. S. Körner, F. Hoffmann, M. Kiessling, V. Novak, J.-Y. Chauleau, and C. H. Back, "Spatial constraints on the source of uniaxial anisotropy in (Ga,Mn)As films," J. Phys. D: Appl. Phys. **47**, 195001 (2014).

[109] R. Dreyer, N. Liebing, E. R. J. Edwards, and G. Woltersdorf, "Local spin-wave dispersion and damping in thin yttrium-iron-garnet films," ArXiv e-prints (2018), 1803.04943 .

[110] F. Hoffmann, *Magnetic anisotropies of (Ga,Mn)As films and nanostructures*, Ph.D. thesis, Universität Regensburg (2010).

[111] M. Decker, *Spin Hall Induced Spin transfer Torque*, Master's thesis, Universität Regensburg (2012).

[112] M. M. Decker, *Spin Current Induced Control of Magnetization Dynamics*, Ph.D. thesis, Universität Regensburg (2018).

[113] H. S. Körner, *Time-Resolved Kerr Microscopy of Spin Waves Propagating in Magnetic Nanostructures*, Ph.D. thesis, Universität Regensburg (2018).

[114] S. Bader, "SMOKE," J. Magn. Magn. Mater. **100**, 440 (1991).

[115] S. Blundell, *Magnetism in condensed matter* (Oxford University Press, 2001).

[116] V. E. Demidov, S. O. Demokritov, D. Birt, B. O'Gorman, M. Tsoi, and X. Li, "Radiation of spin waves from the open end of a microscopic magnetic-film waveguide," Phys. Rev. B **80**, 014429 (2009).

[117] T. Schneider, A. A. Serga, A. V. Chumak, C. W. Sandweg, S. Trudel, S. Wolff, M. P. Kostylev, V. S. Tiberkevich, A. N. Slavin, and B. Hillebrands, "Nondiffractive subwavelength wave beams in a medium with externally controlled anisotropy," Phys. Rev. Lett. **104**, 197203 (2010).

[118] H. S. Körner, J. Stigloher, and C. H. Back, "Excitation and tailoring of diffractive spin-wave beams in NiFe using nonuniform microwave antennas," Phys. Rev. B **96**, 100401 (2017).

[119] R. Gieniusz, H. Ulrichs, V. D. Bessonov, U. Guzowska, A. I. Stognii, and A. Maziewski, "Single antidot as a passive way to create caustic spin-wave beams in yttrium iron garnet films," Appl. Phys. Lett. **102**, 102409 (2013).

[120] F. Goedsche, "Reflection and refraction of spin waves," Phys. stat. sol. (b) **39**, K29 (1970).

[121] Y. I. Gorobets and S. A. Reshetnyak, "Reflection and refraction of spin waves in uniaxial magnets in the geometrical-optics approximation," Tech. Phys. **43**, 188 (1998).

[122] S.-K. Kim, S. Choi, K.-S. Lee, D.-S. Han, D.-E. Jung, and Y.-S. Choi, "Negative refraction of dipole-exchange spin waves through a magnetic twin interface in restricted geometry," Appl. Phys. Lett. **92**, 212501 (2008).

[123] D.-E. Jeong, D.-S. Han, and S.-K. Kim, "Refractive index and snell's law for dipole-exchange spin waves in restricted geometry," Spin **01**, 27 (2011).

[124] R. Gieniusz, V. D. Bessonov, U. Guzowska, A. I. Stognii, and A. Maziewski, "An antidot array as an edge for total non-reflection of spin waves in yttrium iron garnet films," Appl. Phys. Lett. **104**, 082412 (2014).

[125] A. Vashkovskii, A. Stal'makhov, and D. Shakhnazaryan, "Formation, reflection, and refraction of magnetostatic wave beams," Sov. Phys. J. **31**, 908 (1988).

[126] A. V. Vashkovskii and E. H. Lokk, "Negative refractive index for a surface magnetostatic wave propagating through the boundary between a ferrite and ferrite-insulator-metal media," Phys. Usp. **47**, 601 (2004).

[127] K. Tanabe, R. Matsumoto, J.-I. Ohe, S. Murakami, T. Moriyama, D. Chiba, K. Kobayashi, and T. Ono, "Real-time observation of snells law for spin waves in thin ferromagnetic films," Appl. Phys. Exp. **7**, 053001 (2014).

[128] J.-N. Toedt, S. Mansfeld, D. Mellem, W. Hansen, D. Heitmann, and S. Mendach, "Interface modes at step edges of media with anisotropic dispersion," Phys. Rev. B **93**, 184416 (2016).

[129] H. Hata, T. Moriyama, K. Tanabe, K. Kobayashi, R. Matsumoto, S. Murakami, J.-I. Ohe, D. Chiba, and T. Ono, "Micromagnetic simulation of spin wave propagation in a ferromagnetic film with different thicknesses," J. Magn. Soc. of Japan **39**, 151 (2015).

[130] J.-N. Toedt, M. Mundkowski, D. Heitmann, S. Mendach, and W. Hansen, "Design and construction of a spin-wave lens," Sci. Rep. **6**, 33169 (2016).

[131] S. van der Walt, J. L. Schönberger, J. Nunez-Iglesias, F. Boulogne, J. D. Warner, N. Yager, E. Gouillart, T. Yu, and the scikit-image contributors, "scikit-image: image processing in Python," PeerJ **2**, e453 (2014).

[132] E. Jones, T. Oliphant, P. Peterson, *et al.*, "SciPy: Open source scientific tools for Python," (2001–), http://www.scipy.org; accessed October 8, 2018.

[133] M. Madami, S. Bonetti, G. Consolo, S. Tacchi, G. Carlotti, G. Gubbiotti, F. Mancoff, M. Yar, and J. Akerman, "Direct observation of a propagating spin wave induced by spin-transfer torque," Nat. Nano. **6**, 635 (2011).

[134] B. Van de Wiele, S. J. Hämäläinen, P. Balaz, F. Montoncello, and S. van Dijken, "Tunable short-wavelength spin wave excitation from pinned magnetic domain walls," Sci. Rep. **6**, 21330 (2016).

[135] K. K. Tikuisis, L. Beran, P. Cejpek, K. Uhlirová, J. Hamrle, M. Vanatka, M. Urbánek, and M. Veis, "Optical and magneto-optical properties of permalloy thin films in 0.7–6.4eV photon energy range," Materials & Design **114**, 31 (2017).

[136] K. Y. Bliokh and A. Aiello, "Goos–hänchen and Imbert-Fedorov beam shifts: An overview," J. Opt. **15**, 014001 (2013).

[137] W. Yu, J. Lan, R. Wu, and J. Xiao, "Magnetic Snell's law and spin-wave fiber with Dzyaloshinskii-Moriya interaction," Phys. Rev. B **94**, 140410 (2016).

[138] P. Gruszecki, M. Kasprzak, A. E. Serebryannikov, M. Krawczyk, and W. Smigaj, "Microwave excitation of spin wave beams in thin ferromagnetic films," Sci. Rep. **6**, 22367 (2016).

[139] P. Gruszecki, M. Mailyan, O. Gorobets, and M. Krawczyk, "Goos-Hänchen shift of a spin-wave beam transmitted through anisotropic interface between two ferromagnets," Phys. Rev. B **95**, 014421 (2017).

[140] K. Yasumoto and Y. Oishi, "A new evaluation of the Goos-Hänchen shift and associated time delay," J. Appl. Phys. **54**, 2170 (1983).

[141] R. Matsumoto and S. Murakami, "Theoretical prediction of a rotating magnon wave packet in ferromagnets," Phys. Rev. Lett. **106**, 197202 (2011).

[142] R. Matsumoto and S. Murakami, "Rotational motion of magnons and the thermal hall effect," Phys. Rev. B **84**, 184406 (2011).

[143] R. Matsumoto, R. Shindou, and S. Murakami, "Thermal Hall effect of magnons in magnets with dipolar interaction," Phys. Rev. B **89**, 054420 (2014).

[144] C. Bayer, S. O. Demokritov, B. Hillebrands, and A. N. Slavin, "Spin-wave wells with multiple states created in small magnetic elements," Appl. Phys. Lett. **82**, 607 (2003).

[145] U.-H. Hansen, M. Gatzen, V. E. Demidov, and S. O. Demokritov, "Resonant tunneling of spin-wave packets via quantized states in potential wells," Phys. Rev. Lett. **99**, 127204 (2007).

List of Publications

- J. Stigloher, M. Decker, H. S. Körner, K. Tanabe, T. Moriyama, T. Taniguchi, H. Hata, M. Madami, G. Gubbiotti, K. Kobayashi, T. Ono, and C. H. Back, "Snell's law for spin waves," Phys. Rev. Lett. 117, 037204 (2016).

- J. Stigloher, T. Taniguchi, M. Madami, M. Decker, H. S. Körner, T. Moriyama, G. Gubbiotti, T. Ono, and C. H. Back, "Spin-wave wavelength down-conversion at thickness steps," Appl. Phys Express 11, 053002 (2018).

- J. Stigloher, T. Taniguchi, H. S. Körner, M. Decker, T. Moriyama, T. Ono, and C. H. Back, "Observation of a Goos-Hänchen-like phase shift for magnetostatic spin waves," Phys. Rev. Lett. 121, 137201 (2018).

- H. S. Körner, J. Stigloher, H. G. Bauer, H. Hata, T. Taniguchi, T. Moriyama, T. Ono, and C. H. Back, "Interfacial Dzyaloshinskii-Moriya interaction studied by time-resolved scanning Kerr microscopy," Phys. Rev. B 92, 220413 (2015).

- H. S. Körner, J. Stigloher, and C. H. Back, "Excitation and tailoring of diffractive spin-wave beams in NiFe using nonuniform microwave antennas," Phys. Rev. B 96, 100401 (2017).

- A. Talalaevskij, M. Decker, J. Stigloher, A. Mitra, H. S. Körner, O. Cespedes, C. H. Back, and B. J. Hickey, "Magnetic properties of spin waves in thin yttrium iron garnet films," Phys. Rev. B 95, 064409 (2017).

- H. S. Körner, M. A. W. Schön, T. Mayer, M. M. Decker, J. Stigloher, T. Weindler, T. N. G. Meier, M. Kronseder, and C. H. Back, "Magnetic damping in polycrystalline Co25Fe75: Ferromagnetic resonance vs. spin wave propagation experiments," Appl. Phys. Lett. 111, 132406 (2017).

Acknowledgment

I want to say a big "Thank you!" to the following persons:

First and foremost Prof. Dr. Christian Back for the opportunity to do my PhD in his group. I had the freedom to pursue own ideas while he was there to give valuable scientific guidance whenever needed. I also thank him for the chance to present our work on many international conferences, even at the beginning of this thesis. He understands to create a pleasant working environment, not only by keeping an eye on the coffee-quality and providing us with Steckerlfisch and Kickertisch.

Prof. Dr. Teruo Ono and his group at Kyoto University for the sample preparation, the idea to use thickness steps for refraction, as well as the support during the write-up of publications. Especially, I want to thank Dr. Takahiro Moriyama and Dr. Takuya Taniguchi.

Prof. Dr. Gianluca Gubbiotti and Dr. Marco Madami for their contributions to two publications. In particular, they conducted BLS experiments and were involved in the writing process of both publications on refraction experiments. I greatly appreciate their encouragement throughout this collaboration.

Helmut Körner for his assistance in my first years, for countless discussions, and our symbiotic work-flow in many experiments. Consequently, he is part of all my publications and additionally helped me with many tasks like sample preparation, proof-reading, and calculations of spin wave dispersions.

Martin Decker for being a great lab-mate, for his interest in my work, and for providing a sofa in his office in times of need.

Jean-Yves Chauleau for introducing me to spin waves and the TRMOKE setup.

Hans Bauer for laying the basis of the dynamic matrix method and in general all kinds of assistance at theoretical and numerical problems.

Magdalena Pfleger, Sylvia Hrdina, Claudia Zange, and Doris Meier for their assistance on administrative issues.

Markus Hollnberger for his help with all technical problems.

All members of the chair, for creating such a great working atmosphere, in particular my office mates Martin Buchner, Martin Schön, and especially Robert Islinger.

Martin Decker, Helmut Körner, and Johannes Ziegler for proof-reading different parts of this thesis.

Sebastian Schöttl and Maria Stigloher for linguistic proof-reading.

Julia Butz for proof-reading and her constant support throughout the whole course of this thesis.